



**HAL**  
open science

# Effects of solid-solid boundary anisotropy on directional solidification microstructures

Supriyo Ghosh

► **To cite this version:**

Supriyo Ghosh. Effects of solid-solid boundary anisotropy on directional solidification microstructures. Engineering Sciences [physics]. Ecole Polytechnique, 2015. English. NNT : . tel-01204752

**HAL Id: tel-01204752**

**<https://pastel.hal.science/tel-01204752>**

Submitted on 24 Sep 2015

**HAL** is a multi-disciplinary open access archive for the deposit and dissemination of scientific research documents, whether they are published or not. The documents may come from teaching and research institutions in France or abroad, or from public or private research centers.

L'archive ouverte pluridisciplinaire **HAL**, est destinée au dépôt et à la diffusion de documents scientifiques de niveau recherche, publiés ou non, émanant des établissements d'enseignement et de recherche français ou étrangers, des laboratoires publics ou privés.



# Effects of solid-solid boundary anisotropy on directional solidification microstructures

A Thesis

submitted for the degree of

*Doctor of Philosophy*

in the *Department of Physics*

*(Speciality: Materials Science)*

by

**Supriyo Ghosh**

Committee in charge:

Prof. Jean-Marc Debierre	Université d'Aix-Marseille	Reviewer
Dr. Tamás Pusztai	WRCP, Budapest	Reviewer
Dr. Ulrike Hecht	ACCESS, Aachen	Examiner
Dr. Yann Le Bouar	LEM, CNRS/ONERA	Examiner
Dr. Silvère Akamatsu	INSP, UPMC	Examiner
Dr. Mathis Plapp	PMC, École Polytechnique	Supervisor

Laboratoire de Physique de la Matière Condensée (LPMC)

École Polytechnique

Palaiseau – 91128 (FRANCE)

SEPTEMBER 2015

*To my beloved parents*

# Acknowledgements

Looking down the memory lane, when I was three years younger, I took the most difficult decision of my life till date. I had decided to do a PhD! Even though there were ups and downs in this journey, numerous people made this journey joyful and successful.

At first, I express my deepest gratitude to my PhD supervisor Dr. Mathis Plapp for his consistent guidance and motivation through these years. I have learnt a lot from you Mathis. A big thank you. I also thank Prof. Alain Karma for supervising me during my three months stay at Northeastern University, Boston. I acknowledge our experimental collaborators - Dr. Silvère Akamatsu, Dr. Gabriel Faivre and Dr. Sabine Bottin-Rousseau - for providing us the exciting experimental evidences which motivated the thesis. I am grateful to Dr. Abhik Choudhury who helped me in writing the code during my first year of PhD. Thank you Abhik for keeping in touch with us beyond this period. Thanks to Julien Monguillon for helping me run simulations in the clusters. I convey my gratitude to Prof. Jean-Marc Debierre and Dr. Tamás Putzai for carefully reading my thesis. I also thank Yann Le Bouar and Ulrike Hecht for being the examiners in my thesis defence.

Thank you to Lucio Martinelli and Khalid Lahlil, who share the same office with me. I am lucky to have them as roommates because most of the time they are away of the office to do experiments and I have the room for myself! I would like to thank all my friends in the PMC lab – Tapajyoti, Maria, Marine, Tim, Manon, Lili, Petr, Nan, Marco, Hongye, Surya and many others. You guys have been a great support to me. Thank you to the lab members in Northeastern University - Antoine, Matteo, Collin and others. You made my life at the work and at the Boston very much engaged. I also thank to my India house friends – Siddarth, Gourav, Ashwath, Ghayaz, Ayan, Satish, Shalini, Ranajoy, Bitan,

Koushik, Alok and many others – for not letting me skip any meals, without even cooking!  
I had so much of fun with you guys!

# Abstract

Solidification microstructures have been the subject of intense theoretical and experimental research because of the fundamental importance of these structures in the properties of materials and because these structures represent an excellent example of pattern formation in nature. Moreover, these structures are significantly influenced by the structure and the properties of the interfaces in it. In a broader sense, the present thesis examines the effects of these interfaces on solidification microstructures.

The microstructures arising from the solidification processing possess various types of boundaries: solid-liquid interfaces, grain boundaries (GB), interphase boundaries (IB). Whereas solid(S)-liquid(L) interfaces have been investigated extensively, relatively little attention has been paid to the solid(S)-solid(S) boundaries (GB and IB). Recently, it has been found that S-S boundary anisotropy can also have a significant influence, particularly on the overall orientation selection of the growing patterns. More specifically, the present thesis investigates the effects of GB and IB anisotropy through simulations of solidification morphologies.

Recently, an efficient quantitative phase-field model has been developed to study the solidification dynamics in multicomponent, multiphase alloys. This model differs from other contemporary models in the sense that, chemical potential has replaced the composition variable to describe the mass conservation equation in the system. This is motivated by the fact that, at equilibrium, the chemical potential is constant through the interfaces, while concentration exhibits a jump. This allows us to exploit larger interface thicknesses in the simulations of microstructures without affecting the quality of the results. For the present purpose, we have implemented this model, and applied this code to study three problems

stemming from the directional solidification of lamellar eutectics and polycrystals, with a particular focus on the effects of the S-S boundary anisotropy.

During thin-film directional solidification experiments on lamellar eutectics in  $\text{CBr}_4\text{-C}_2\text{Cl}_6$ , it has been observed that in the absence of interfacial anisotropy, the solid phases grow straight next to each other, the IBs are aligned with the growth direction, and Young's law is satisfied at the trijunction points. Whereas, in non-faceted substances, the S-L surface free energy is only weakly anisotropic, the anisotropy of S-S IB can be strong. This anisotropy depends on the relative orientation of the two solids with respect to each other. The anisotropy function thus is not an intrinsic property of the material, but differs between different *eutectic grains* – that is, portions of the solid in which the orientations of the two phases remain homogeneous. One may distinguish *floating grains* with low anisotropy from *locked grains* with high anisotropy. In the latter, the IB may remain “locked” onto a direction of low energy, irrespective of the orientation of the grain with respect to the temperature gradient. A recent theory uses the anisotropic Young-Herring condition at the trijunction, to predict the orientations a eutectic grain can possess in a microstructure. This is the prediction against which we compare our numerical results.

Recent experiments on bulk lamellar eutectics suggest that the (disordered) labyrinthine eutectic structures, which result from the direction solidification of Al - Cu alloys, never become ordered in experimentally accessible time scales. These bulk structures contain multiple eutectic grains and interphases leading to multiple orientations. We attempt to simulate these microstructures including the influence of the anisotropy along the IBs. IB-anisotropy tends to align the IBs with the directions of minimal energy. Lamellae oriented in these directions grow at the expense of the other lamellae, until they eventually totally outgrow them. In this way, an ordered lamellar structure with a preferred direction is formed.

Finally, we examine the effect of GB anisotropy on solidification morphologies. This is motivated by an experimental study on the directional solidification of grain-boundaries in  $\text{CBr}_4\text{-C}_2\text{Cl}_6$  illustrating that a low-angle GB grows at a fixed angle with respect to the growth axis. This is true, as long the melt/solid front remains planar or nearly planar. The

moment that these interfaces break into cellular structures at a certain critical solidification rate, the angle between the GB and the growth axis starts to decrease until the GB follows the direction of the temperature gradient. We simulate the growth of bicrystals for various solidification velocities using a suitable anisotropy function and find that the mobility of the GB plays an important role in the selection of the growth angle.



# Contents

<b>Acknowledgements</b>	<b>i</b>
<b>Abstract</b>	<b>iii</b>
<b>1 Introduction</b>	<b>1</b>
1.1 Directional solidification . . . . .	2
1.2 Solidification of single phase alloys . . . . .	3
1.2.1 Morphological instability . . . . .	6
1.2.2 Constitutional supercooling (CS) . . . . .	6
1.2.3 Mullins-Sekerka instability . . . . .	8
1.3 Solidification of multiphase alloys: Eutectic solidification . . . . .	11
1.4 Surface tension anisotropy: Origin and Effects . . . . .	15
1.5 Rotating directional solidification (RDS) . . . . .	22
1.6 Numerical methods . . . . .	23
1.7 Thesis Outline and motivation . . . . .	25
<b>2 Simulation Methods</b>	<b>28</b>
2.1 Sharp-interface problem . . . . .	29
2.2 Basics of Phase Field Method . . . . .	31
2.3 Grand-canonical Multi-phase-field Model . . . . .	32
2.4 Thermodynamic description of the free energy . . . . .	36
2.5 Incorporation of Anisotropy . . . . .	37
2.6 Regularized Phase-field model . . . . .	41
2.6.1 Willmore Regularization . . . . .	42
2.6.2 Linear Regularization . . . . .	43
2.7 Relation to sharp interface theory . . . . .	44
<b>3 Interphase Anisotropy Effects on Lamellar Eutectics</b>	<b>46</b>
3.1 Introduction . . . . .	46
3.2 Background . . . . .	50
3.2.1 Anisotropic inter-phase boundaries . . . . .	50
3.2.2 Theoretical predictions for the tilt angle . . . . .	52
3.3 Boundary-integral method . . . . .	54
3.3.1 Parameters . . . . .	54

3.4	Results . . . . .	55
3.4.1	General remarks . . . . .	55
3.4.2	Anisotropy functions without missing orientations . . . . .	59
3.4.3	Anisotropy with missing orientations . . . . .	62
3.5	Discussion . . . . .	65
3.5.1	Reconstructing the anisotropy function . . . . .	65
3.5.2	Bistability in the numerical simulations . . . . .	65
3.6	Conclusions and perspectives . . . . .	68
<b>4</b>	<b>Interphase Anisotropy Effects on Bulk Lamellar Eutectics</b>	<b>70</b>
4.1	Introduction . . . . .	70
4.2	Simulation Details . . . . .	71
4.2.1	Parameters . . . . .	71
4.2.2	Procedures . . . . .	72
4.3	Results . . . . .	73
4.3.1	Lamellar tilt . . . . .	73
4.3.2	Structural selection in single eutectic grain . . . . .	75
4.3.3	Multiple eutectic grains . . . . .	80
4.4	Conclusions and Outlook . . . . .	84
<b>5</b>	<b>Influence of grain boundary anisotropy during directional solidification</b>	<b>86</b>
5.1	Introduction . . . . .	86
5.2	Background . . . . .	88
5.2.1	Morphological instability . . . . .	88
5.2.2	Grain Boundary (GB) and Sub-Boundary (SB) . . . . .	88
5.2.3	Anisotropic interphase boundaries . . . . .	89
5.2.4	Theoretical prediction of the tilt angle . . . . .	90
5.3	Method . . . . .	92
5.3.1	Parameters . . . . .	92
5.4	Results . . . . .	93
5.4.1	Behaviour of SB below CS . . . . .	93
5.4.2	Above MS . . . . .	94
5.4.3	Above CS, Below MS . . . . .	97
5.4.4	Interaction between SBs . . . . .	98
5.5	Conclusions and Outlook . . . . .	101
<b>6</b>	<b>Overall summary, Conclusions and Outlook</b>	<b>103</b>
	<b>Appendix A Anisotropy Implementation Techniques</b>	<b>107</b>
	<b>Appendix B Rotation Matrices in 2-D and 3-D</b>	<b>110</b>
B.1	2-D . . . . .	110
B.2	3-D . . . . .	110

---

<b>Appendix C Choice of Anisotropy <math>\gamma</math> Functions</b>	<b>113</b>
C.1 4-fold . . . . .	113
C.2 2-fold . . . . .	114
C.3 In presence of a cusp . . . . .	115
C.4 Composite Anisotropy Function . . . . .	116
<b>Bibliography</b>	<b>118</b>

# List of Figures

1.1	Experimental directional solidification set up [6]; all details are explained in the text . . . . .	3
1.2	Schematic Phase diagram of a dilute binary alloy . . . . .	4
1.3	Steady state concentration profile of the solute pile-up ahead of the solidification front; At temperature $T_2$ , $c_s = c_0$ and $c_l = c_0/k$ . . . . .	5
1.4	The change of the morphology with increasing velocity for a directionally solidified transparent organic alloy (pivalic acid-0.076% ethanol) with a temperature gradient of 2.98 K/mm (adapted from [2]); (a) planar S-L interface, (b)unstable interface leading to shallow cells (c) cells (d) dendrites	7
1.5	Diffusion profile ahead of the interace and the corresponding equilibrium liquidus temperature profile. (a)No constitutional undercooling (c) critical constitutional undercooling limit (b) constitutional supercooling zone. (adapted from [8]) . . . . .	8
1.6	The effect of $G/V$ on the solidification microstructures; $c_0$ is the alloy composition (adapted from [2]) . . . . .	9
1.7	Plot of $w_q$ given by Eq. (1.13) for different wavenumbers $q$ (schematic) . .	10
1.8	Experimental observation of the growth of a planar S-L interface into cells. The experiment is performed for a sample of 0.25% poly(ethylene oxide) in succinonitrile with a pulling speed $V = 1.34\mu m/s$ (adapted from [7]) . . . .	11
1.9	A schematic eutectic phase diagram. $C_E$ and $T_E$ are the eutectic composition and temperature, respectively . . . . .	12
1.10	Regular and irregular eutectic morphologies (adapted from D. M. Stefanescu [2]) . . . . .	13
1.11	Solute diffusion paths leading to the lamellar sequence of $\alpha$ and $\beta$ phases (adapted from D. M. Stefanescu [2])) . . . . .	14
1.12	Front undercooling vs. lamellar spacing for a eutectic front: Jackson-Hunt(JH) minimum undercooling criteria . . . . .	14
1.13	Variation of surface energy as a function of $\theta$ around a facet . . . . .	15
1.14	Surface tension ( $\gamma$ ) profile of an isolated solid, and the equilibrium crystal shape (adapted from [28]) . . . . .	16
1.15	. . . . .	17
1.16	Cubic anisotropy with a four-fold symmetry: $\gamma = \bar{\gamma}[1 + 0.06 \cos(4\theta)]$ . . . . .	18
1.17	Parametric Plots: Red: $\gamma$ plot; Green: $1/\gamma$ plot; Blue: $\vec{\xi}$ plot . . . . .	20

1.18	A rotating directional solidification run: (a) seed crystal and grain selection (b)directional solidification (c) start of RDS run (d) after long run. Empty rectangles are the hot and cold blocks and X is the center of rotation (Adapted from Akamatsu et. al[41]) . . . . .	23
1.19	Representational rotating coordinate frame . . . . .	24
1.20	CBr <sub>4</sub> -C <sub>2</sub> Cl <sub>6</sub> lamellar eutectic formation in the (a) absence of anisotropy (b) presence of anisotropy (adapted from Akamatsu et al. [41]). The two micrographs are taken from two different eutectic grains. Bar: 20 $\mu$ m. . . . .	26
1.21	Transformation of an disordered lamellar arrays or labyrinths towards a regular lamellar arrays with a preferred orientation in the bulk eutectic sample (adapted from Hecht et al. [68]) . . . . .	27
1.22	Orientation of a low-angle GB (a) below CS velocity (b) above MS velocity. Note that, in figure (b) the bottom part of the GB has been solidified above MS velocity; then a downward velocity jump in the experiment makes the GB to orient at an angle in the low velocity regime (adapted from Bottin et al. [69]) . . . . .	27
2.1	(left) A sharp interface and (right) a diffuse interface (adapted from Sin et al. [47]) . . . . .	29
2.2	Two angles $\varphi$ and $\theta$ represent a spherical coordinate system. $xy$ is the azimuthal plane. Axis $z$ is the direction of G as well as the growth direction which renders the azimuthal plane as a transverse plane of the simulation box. . . . .	40
3.1	Lamellar eutectic patterns observed in situ during thin-sample directional solidification ( $V = 0.5\mu ms^{-1}$ ) of a eutectic transparent (CBr <sub>4</sub> -C <sub>2</sub> Cl <sub>6</sub> ) model alloy. a) Symmetric steady-state in a “floating” eutectic grain. b) Tilted lamellae in a “locked” eutectic grain. The growth direction is vertical (liquid on top). Bar: 20 $\mu$ m. . . . .	47
3.2	Schematic repeat units of lamellar eutectic patterns. a) Isotropic system. b) System with an interfacial anisotropy of the interphase boundary in the symmetric-pattern (SP) approximation. $\alpha, \beta$ : solid phases. $L$ : liquid. $z$ : growth direction parallel to the thermal gradient. $x$ : direction of the isotherms. $\theta_{sp}$ : SP-approximation lamellar tilt angle. The lateral drift velocity is given by $\tan \theta_{sp} = V_d/V$ , with $V$ the pulling velocity. Other symbols: see text. . . . .	48
3.3	a) Illustration of the Young-Herring equilibrium condition at the trijunction. $\vec{n}$ and $\vec{t}$ : normal and tangent unit vectors of the interphase boundary. b) Definition of the tilt angle $\theta_t$ and the angle $\delta$ between $\vec{\sigma}$ and $z$ . . . . .	53
3.4	Steady-state lamellar patterns (BI simulations). a) Symmetric pattern without anisotropy. b) Tilted pattern with anisotropic interphase boundaries (anisotropy function given by Eq. (3.4); $\epsilon_g = 0.2$ ; $w_g = 0.1$ ; $\theta_R = 3\pi/48 \approx 11.25^\circ$ ; $Pe = 0.024$ ; $\theta_t = 11.0^\circ$ ). c) Spatio-temporal diagram showing the steady-state dynamics corresponding to a) and b), successively, and the brief transient after the anisotropy was turned on. . . . .	56

3.5	Drifting lamellar patterns in the PF model; the anisotropy function is given by Eq. (3.5) with $\epsilon_g = 0.2$ , $w_g = 0.1$ , $\epsilon_2 = 0.0854$ , and $\epsilon_4 = 0.0221$ (the same function as in Fig. 3.10 below): (a) “locked” tilted state ( $\theta_t = 29^\circ, \theta_R = 30^\circ$ ), (b) transition from a locked to an unlocked tilted state upon change of $\theta_R$ from $35^\circ$ to $40^\circ$ , (c) unlocked tilted state ( $\theta_t = 10.8^\circ, \theta_R = 50^\circ$ ). Other parameters: $d_0/l_D = 7.9 \times 10^{-3}$ , $l_T/l_D = 3.167$ . . . . .	57
3.6	Steady-state tilt angle $\theta_t$ obtained from BI simulations as a function of the reduced lamellar spacing $\lambda/\lambda_{JH}$ , at constant $G$ and $V$ ( $d_0/l_D = 1.9531 \times 10^{-5}$ , $l_T/l_D = 4$ ). The angle $-\delta$ is also plotted ( $\delta$ is the angle between $\vec{\sigma}$ and $z$ ). Anisotropy function $a_c(\theta) = 1 - 0.05 \cos[2(\theta - \theta_R)]$ ; $\theta_R = \pi/3$ ( $\theta_{sp} = 5.3^\circ$ ). . . . .	58
3.7	Lamellar tilt angle vs Péclet number at constant $\lambda/d_0 = 20.25$ , $d_0/l_T = 2.496 \times 10^{-3}$ ; $a_c = 1 + 0.04 \cos[4(\theta - \theta_R)]$ , $\theta_R = 15^\circ$ ( $\theta_{sp} = 9.07^\circ$ ). . . . .	59
3.8	Lamellar tilt angle as a function of the rotation angle $\theta_R$ . Weak, two-fold symmetry anisotropy of the interphase boundary ( $a_c = 1 - 0.05 \cos[2(\theta - \theta_R)]$ ). The SP-approximation angle $\theta_{sp}$ , and the steady-state angle $\theta_t$ obtained with the BI and PF simulations are both shown. In this graph, as well as in the following, the represented $\theta_R$ range is limited to $[0, \pi/2]$ for obvious symmetry reasons. . . . .	60
3.9	a) Lamellar tilt angle as a function of the rotation angle $\theta_R$ . Mild lamellar locking effect caused by a shallow, smooth local minimum in the Wulff plot of the interphase boundary (see text). Same symbols as in Fig. 3.8. Dashed line: slope 1. b) Wulff shape ( $\theta_R = 0$ ). c) Partial view of the Wulff shape (dash-dotted line) and the shape reconstructed from the $\theta_t$ data of Fig. 3.9 under the SP approximation (thin line). . . . .	61
3.10	a) Lamellar tilt angle as a function of the rotation angle $\theta_R$ . Strong lamellar locking effect with a sharp local minimum in the Wulff plot (see text). Same symbols as in Fig. 3.8. Inset: Wulff plot (thin line) and Wulff shape (thick line). Dashed lines: unstable branches. b) Angle $\delta$ of $\vec{\sigma}$ with $z$ as a function of $\theta_R$ (BI simulations). c) Shape of the lamellar pattern with the largest $\theta_t$ value ( $\approx 48^\circ$ ) simulated with the BI code. . . . .	63
3.11	Experimental observation of a coexistence of eutectic-growth domains with two different tilt angles in a single eutectic grain. Rotating directional solidification of a thin ( $10\text{-}\mu\text{m}$ thick) sample of a eutectic $\text{CBr}_4\text{-C}_2\text{Cl}_6$ alloy. Horizontal dimension: $450\ \mu\text{m}$ . . . . .	66
4.1	A period of lamellae: (a) untilted and (b) tilted state. Colors of $\alpha$ and $\beta$ are red and green, respectively. . . . .	74
4.2	Simulated $\theta_t$ excellently follows the theoretically predicted value for an anisotropy function $a_c = 1 + 0.04 \cos[4(\theta - \theta_R)]$ . . . . .	74
4.3	$\alpha\beta$ interfaces in the transverse plane ( $xy$ ) of the solid which is growing in the $z$ direction. The interfaces are contoured at $\phi_\alpha = \phi_\beta = 0.5$ . . . . .	75
4.4	A random pattern isotropically evolves to a random lamellar pattern; colors of $\alpha_1$ and $\beta_1$ are red and green, respectively. Fig. 4.4c confirms the random spread in interface orientation angles in a labyrinth. . . . .	76

4.5	4-fold phase evolution for $a_c = 1 + \epsilon_4 \cos[4(\varphi - \varphi_R)]$ : $\epsilon_4 = 6\%$ in Fig. 4.5a and $0.5\%$ in Fig. 4.5b; $\varphi_R = 40^\circ$ . Colors of $\alpha$ and $\beta$ are red and green, respectively. . . . .	77
4.6	An initial random configuration of Fig. 4.4a with Neumann boundary condition along one of the directions in the azimuthal plane results into ideal lamellar arrays with a preferred direction at $\tilde{t}=36$ . The anisotropy function being used: $a_c = 1 + 0.3 \cos[2(\varphi - \varphi_R)]$ . Colors of $\alpha$ and $\beta$ are red and green, respectively. . . . .	78
4.7	Temporal variation of spread in orientation for various strengths of 2-fold anisotropy . . . . .	79
4.8	(a)Formation of a defect in lamellar solidification (b) Spread in orientation with time . . . . .	80
4.9	An initial random configuration of Fig. 4.4a with isolate boundary condition along one of the directions: (a) an ideal lamellar arrays with a preferred direction, (b) arrays are arranged at a zero angle with $y$ axis, (c) histogram of interface orientation angles, scanned from a plane of Img. 4.9b. Colors of $\alpha$ and $\beta$ are red and green, respectively. . . . .	81
4.10	Temporal evolution of two eutectic grains according to Eq. (4.4); colors of $\alpha_1$ , $\beta_1$ , $\alpha_2$ and $\beta_2$ are red, green, blue and magenta, respectively. Note, interfaces between $\alpha_1$ and $\beta_1$ are anisotropic. . . . .	83
4.11	Histogram plot of volume fraction distribution with time for Fig. 4.11; colors of $\alpha_1$ , $\beta_1$ , $\alpha_2$ and $\beta_2$ are red, green, blue and magenta, respectively. . . . .	84
4.12	$\alpha_1\beta_1$ anisotropic grain possess higher interfacial energies compared to $\alpha_2\beta_2$ isotropic grain; $\tilde{t} = 56$ , colors of $\alpha_1$ , $\beta_1$ , $\alpha_2$ and $\beta_2$ are red, green, blue and magenta, respectively. . . . .	85
5.1	Formation of a GB groove by balancing the surface and GB tensions at the intersection of a GB with a free surface . . . . .	89
5.2	Anisotropic force balance at a SB trijunction in unidirectional solidification . . . . .	90
5.3	Schematic representation of the tilt angles ( $\theta_t$ ) in three different velocity (V) regimes during directional solidification . . . . .	91
5.4	Below CS: (a) SB tilts at a finite angle with a planar solid-melt interface (b) numerically obtained SB tilt angles are imposed on the analytical solution of Eq. (3.7) . . . . .	94
5.5	Superimposed snapshot pictures of the interfaces above MS suggests a Herring instability along the S-S boundary. Note that units of lengths are in grid spacing. . . . .	95
5.6	Superimposed snapshot pictures of the interfaces above MS: effects of finite mobility on the orientation selection of SB. Note that units of lengths are in grid spacing. . . . .	96
5.7	(a)Superimposed snapshot pictures of the interfaces above MS: Effects of zero mobility on the SB (b) Asymmetry of the GB groove profile . . . . .	97
5.8	Superimposed snapshot pictures of the interfaces in between the CS and MS critical velocity limits . . . . .	98

---

5.9	Superimposed snapshot pictures of the interfaces below CS: interaction between isotropic and anisotropic SBs . . . . .	99
5.10	Superimposed snapshot pictures of the interfaces below CS: interaction between anisotropic SBs . . . . .	100
5.11	Superimposed snapshot pictures of the interfaces above MS: interaction between isotropic and anisotropic SBs . . . . .	100
5.12	Superimposed snapshot pictures of the interfaces above MS: interaction between anisotropic SBs . . . . .	101
C.3	(a) $\gamma - \theta$ plot of function C.8 (b) parametric plot of $\gamma$ (red) and the equilibrium shape (green) for the parameters listed above . . . . .	116
C.4	(a) $\gamma - \theta$ plot of function C.10 (b) parametric plot of $\gamma$ (red) and the equilibrium shape (green) for the parameters listed above . . . . .	117



# Chapter 1

## Introduction

Solidification is a crystallization process through which a liquid phase transforms into solid. The use of this process dates back to the historic times when the human civilization understood the importance of it to cast hunting weapons from a liquid metal mould. Interestingly, the modern world still uses this process to make these old-purposed weapons; however, there are so many other uses of it that human civilization cannot live without it.

The importance of solidification is manifold [1, 2, 3]. Engineers use it as a method to cast objects ranging from a simple pin to a complicated aeroplane engine; these materials are engineered through casting solidification, and the engineers work on the technical aspects of the structure-property-processing relationships of the cast objects. Moreover, solidification is an excellent example for a spontaneous pattern forming process in nature [4, 5]. This intrigues the scientists to study the theoretical aspects of it. Thus, solidification possesses great theoretical and technological importance.

In general, there are two basic techniques of solidification processing depending on the parameters controlling the process [1, 2, 3]. In isothermal solidification of pure materials, the solidification bath is kept at a constant temperature below the melting point, and the solid grows freely from this undercooled melt. In directional solidification, a sample is pulled with fixed velocity through a fixed temperature gradient from a hot to a cold zone. The microstructures formed in this process are very uniform, which helps us to perform the parametric study of these microstructures under well-controlled conditions.

In what follows, we first describe the principles of directional solidification and the morphologies that arise during this process. Then, we talk about the surface tension anisotropy and its effects on the directional solidification microstructures. This is followed by a brief review of the numerical methods through which one can simulate these microstructures. Finally, an outline of the thesis is given in section 1.7.

## 1.1 Directional solidification

In experiment, directional solidification is performed in a set-up shown in Fig. 1.1. This is sometimes referred to as the Bridgman method. In the solidification table, one end is fixed to a hot zone and the other end to a cold zone, which are kept at fixed temperatures using a thermostat, above and below the melting point, respectively. This establishes a fixed temperature gradient ( $G$ ) in the system. The liquid metal is then placed in between these zones. As the solidification progresses, solid phases grow towards the hot zone at a particular growth velocity ( $V$ ) set by a motor that pulls the sample towards the cold zone. These two parameters,  $G$  and  $V$ , are the major controlling parameters of directional solidification experiments. Since the solute diffusivity of solids is generally far smaller than the one of liquids, in common practice the diffusion in the solid is ignored. Moreover, we are interested in studying the structure of solids near to the S-L interface. Thus, if we pull the already-formed solid, which is sufficiently away from the interface, backwards at a constant velocity  $V$ , we retain the necessary information around the S-L interface. Moreover, this keeps the interfaces stationary in the laboratory frame. This is termed steady-state directional solidification [6, 7].

It is useful to mention that typically the solidification samples are prepared as a thin-film, i.e. the sample is confined between glass plates spaced typically by  $10\mu\text{m}$ . These samples are generally an organic material, which solidify at about room temperature. Even though most organic substances have faceted S-L interfaces, however, for the specific material considered here, the interfaces are rough so that these interfaces solidify like metals. In addition, these materials are transparent and, therefore, the solidification process can be recorded using an optical microscope, as shown in Fig. 1.1. Examples of

such materials include Succinonitrile (SCN),  $\text{CBr}_4\text{-C}_2\text{Cl}_6$ , Pivalic acid (PVA) and a few others.

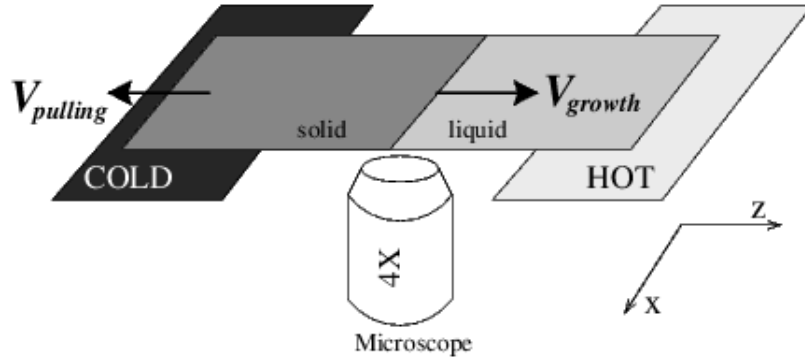


Figure 1.1: Experimental directional solidification set up [6]; all details are explained in the text

## 1.2 Solidification of single phase alloys

Consider a binary alloy consisting of a solvent and a solute. For low solute concentration, the phase diagram looks like Fig. 1.2. For simplicity, consider that the Solidus and Liquidus lines are straight with a Liquidus slope of  $m < 0$ .  $k$  is the equilibrium partition coefficient of the alloy and can be defined at any temperature in Fig. 1.2 as:

$$k = \frac{\text{composition of the solute in the solid}}{\text{composition of the solute in the liquid}} = \frac{c_s}{c_l} \quad (1.1)$$

Under the above conditions, an alloy of liquid composition  $c_0$  initially solidifies into a solid of composition  $c_0k$  (at temperature  $T_1$ ). For the phase diagram shown in Fig. 1.2,  $k < 1$  and, hence,  $c_0k < c_0$ . This excess solute will be rejected from the solid and piles up locally at the S-L interface. In steady-state conditions, the concentration of the solute at the interface is  $c_0/k > c_0$ . The solute concentration ahead of the solid decays exponentially with the distance from the interface and sufficiently far away from the interface, the composition of the liquid equals the nominal composition of the alloy, i.e.  $c_0$ . The profile of such a solute pile-up is shown in Fig. 1.3.

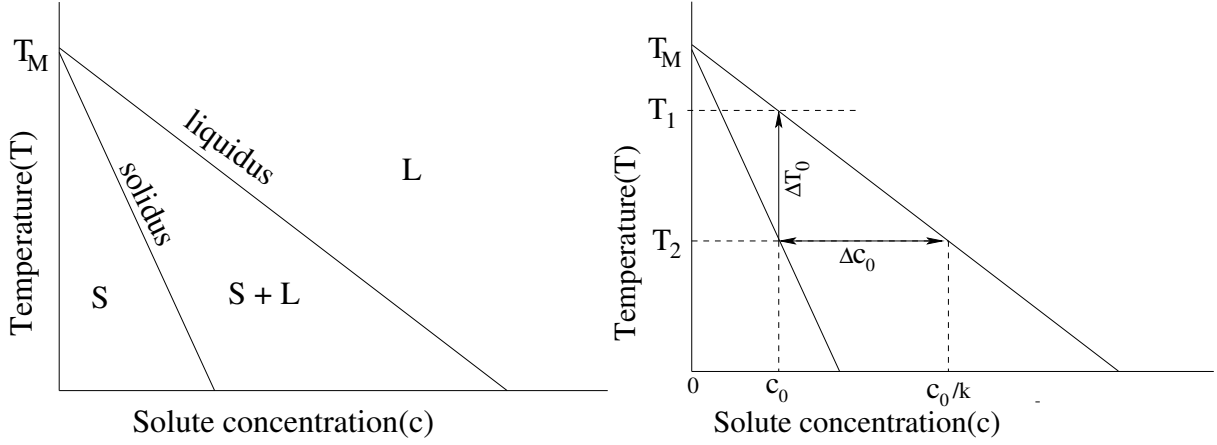


Figure 1.2: Schematic Phase diagram of a dilute binary alloy

So, the concentration jump at the interface due to the pile up of the excess solute, at temperature  $T_2$ , can be written as:

$$\Delta c_0 = \frac{c_0}{k} - c_0 = c_0 \left( \frac{1-k}{k} \right). \quad (1.2)$$

If  $T_M$  is the melting temperature and  $T_2$  is the interface temperature, then the undercooling of a flat interface can be expressed as:

$$\Delta T_0 = T_1 - T_2 = -m \Delta c_0; \text{ (for } m < 0 \text{)} \quad (1.3)$$

For a curved interface, the interface temperature  $T_2$  can be written as,

$$T_2 = T_M + m c_l - \frac{\gamma T_M}{L} \kappa - \frac{V_n}{\mu_k}. \quad (1.4)$$

The first correction in Eq. (1.4) comes from the phase diagram in Fig. 1.2. The second correction is due to the Gibbs-Thomson condition for a interface of curvature  $\kappa$ .  $\gamma_{SL}$  is the interface free energy per unit surface area, and  $L$  is the latent heat of fusion. The final correction is due to the departure of the interface from the local thermodynamic equilibrium condition;  $\mu_k$  is the interface mobility and  $V_n$  is the growth speed normal to the interface.

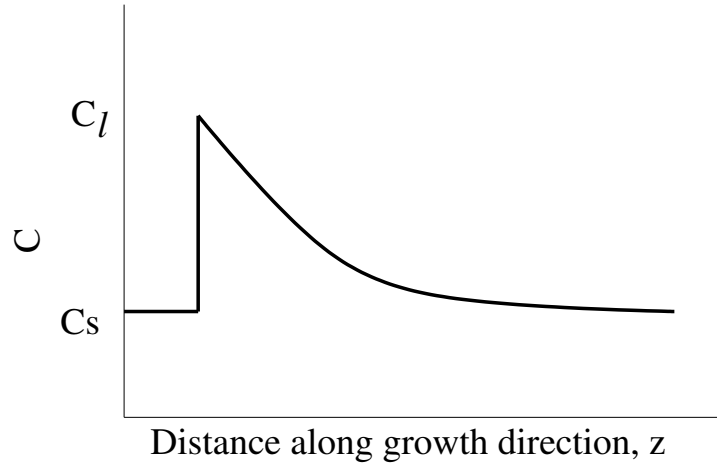


Figure 1.3: Steady state concentration profile of the solute pile-up ahead of the solidification front; At temperature  $T_2$ ,  $c_s = c_0$  and  $c_l = c_0/k$

As we are considering directional solidification with a constant temperature gradient  $G$ , a linear variation is superimposed on the liquid temperature profile, from which a solid is growing in the  $z$  direction,

$$T(z) = T_2 + Gz. \quad (1.5)$$

At the interface, i.e. at  $z = 0$ , the temperature is given by  $T = T_2$ . Under the above conditions, the steady state diffusion equation describing the system in the laboratory frame is given by:

$$\frac{\partial c}{\partial t} = D\nabla^2 c + V \frac{\partial c}{\partial z} = 0. \quad (1.6)$$

$D$  is the diffusivity of the solute in the liquid. Applying boundary conditions from the Fig. 1.3 renders: ( $z = 0, c = c_0/k$  and  $z = \infty, c = c_0$ )

$$c = c_0 \left( 1 + \frac{1-k}{k} \exp\left(-\frac{Vz}{D}\right) \right). \quad (1.7)$$

Note that, this equation describes the exponential solute profile in the solid front in Fig. 1.3. Moreover, there is solute mass conservation at the interface, because the solute rejected at the interface is balanced by the diffusion of the solute in the liquid only

(one-sided diffusion problem). The corresponding mathematical expression is:

$$(c_l - c_s)V_n = -D \left( \frac{\partial c}{\partial n} \right)_{z=0}, \quad (1.8)$$

$\vec{n}$  is a unit vector normal to the interface and pointing into the liquid.

## 1.2.1 Morphological instability

### Directionally solidified morphologies

A brief summary of the essential morphologies formed during the directional solidification is given here. In the limit of low growth velocities, the solute built up ahead of the interface has sufficient time to diffuse away from the interface and, thus, a planar interface forms in between the solid and liquid which grows into the liquid with the imposed velocity  $V$ . When the sample is pulled through the temperature gradient ( $G$ ) with a higher velocity, in essence, the solute does not have enough time to diffuse away from the interface, and, thus, the planar interface will not be able to continue growing at the imposed velocity. Thus, an instability is set up in the system and a cellular structure results. With further increase of  $V$ , a tree-like dendritic morphology prevails with or without side-branches. The effects of the increasing velocity on the solidification microstructures are shown in Fig. 1.4.

## 1.2.2 Constitutional supercooling (CS)

Recall from the previous section,

$$T(z) = T_2 + Gz, \quad (1.9)$$

$T_2$  is the interface temperature and  $G$  is the thermal gradient in the liquid. The phase diagram in Fig. 1.2 describes how the increase in solute content in the liquid decreases the freezing temperature of the solid. Depending on the thermal gradient in the liquid, there may exist a thin layer of liquid ahead of the interface, where the temperature is below the equilibrium liquidus temperature  $T_2$ . This condition is illustrated in Fig. 1.5 (see line b).

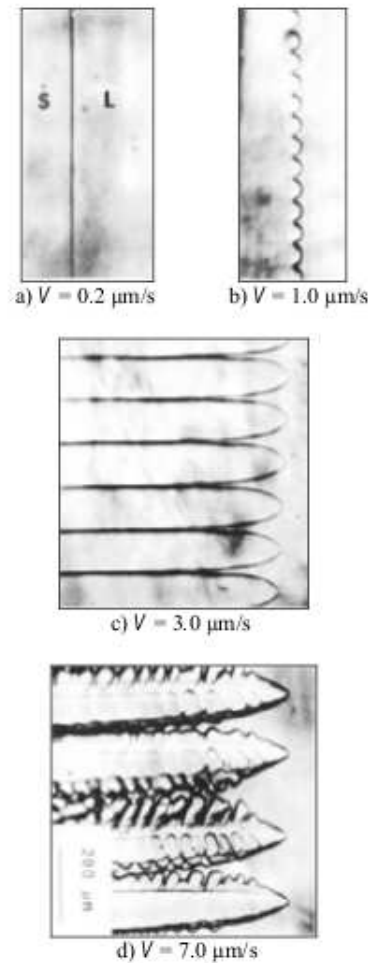


Figure 1.4: The change of the morphology with increasing velocity for a directionally solidified transparent organic alloy (pivalic acid-0.076% ethanol) with a temperature gradient of 2.98 K/mm (adapted from [2]); (a) planar S-L interface, (b) unstable interface leading to shallow cells (c) cells (d) dendrites

Referring to Fig. 1.5, if the applied thermal gradient ( $G$ ) is reduced below the Liquidus gradient  $G_L$  (line b), there is a layer of liquid around the solid which have lower temperature than the solid. This is the essence of constitutional supercooling which is given by the critical  $G_L$  which equals to the  $G$  (line c in Fig. 1.5). Therefore, the critical  $G$  to avoid constitutional undercooling is:  $G \geq \left(\frac{dT}{dz}\right)_c$ . This is the classical macroscopic criterion of CS, introduced by Tiller et al.[9]. In this (experimental) criterion, the presence of an

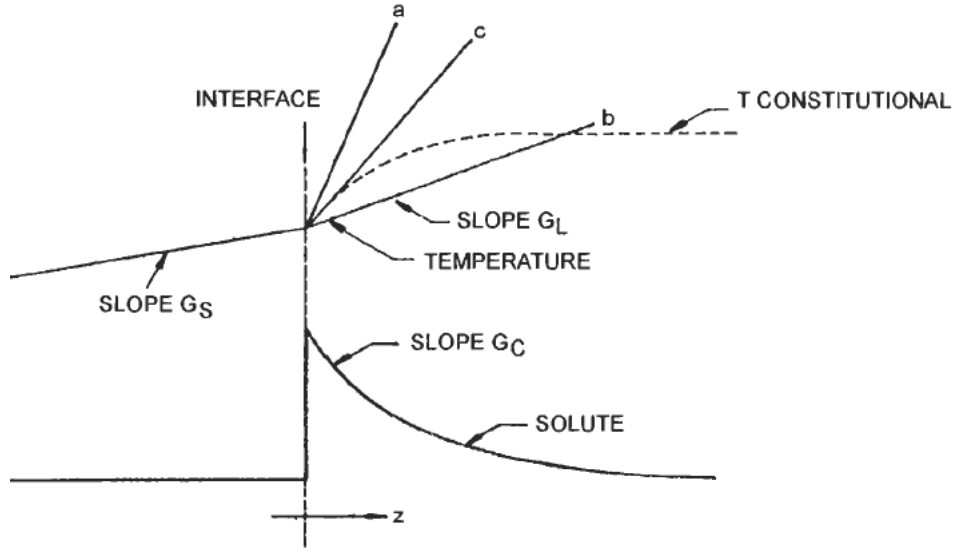


Figure 1.5: Diffusion profile ahead of the interface and the corresponding equilibrium liquidus temperature profile. (a) No constitutional undercooling (c) critical constitutional undercooling limit (b) constitutional supercooling zone. (adapted from [8])

undercooled region is determined by the  $G/V$  ratio, according to the following expression:

$$\frac{G}{V} \leq \frac{m\Delta c_0}{D}. \quad (1.10)$$

Note that, the left hand side involves the process parameters while on the right side elements are the materials parameters. There are two ways how one can cross the constitutional supercooling limit, either by decreasing the thermal gradient  $G$  or by increasing the velocity  $V$ . Thus, the  $G/V$  ratio determines the equilibrium microstructures of a solidification system, as shown in Fig. 1.6. The corresponding expression for  $V_{CS}$  is given by:

$$V_{CS} = \frac{DG}{m\Delta c_0}. \quad (1.11)$$

### 1.2.3 Mullins-Sekerka instability

As discussed earlier, for low velocity, the solid grows with a planar interface. To develop a non-planar interface from a planar interface, some perturbations must be locally present to trigger the growth of an instability. Consider that, a infinitesimal sinusoidal perturbation



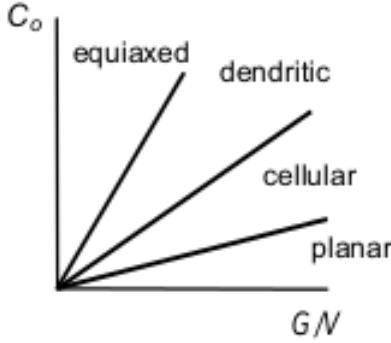


Figure 1.6: The effect of  $G/V$  on the solidification microstructures;  $c_0$  is the alloy composition (adapted from [2])

of certain amplitude is introduced to a steady state planar S-L interface profile in the following way:

$$c(x, z, t) = c(z, t) + A \sin(qx) \exp(\omega_q t) \quad (1.12)$$

$z$  is the direction of growth of the solid,  $x$  is the direction parallel to the interface,  $A$  is the amplitude of the sinusoidal perturbation, and  $\omega_q$  is the growth rate related to the applied wave-number  $q$ , which further relates to the wavelength by  $q = 2\pi/\lambda$ . Mullins and Sekerka in their seminal work [10] used a linear stability analysis, which determines whether a wave of particular wave number will grow or decay. The wavelengths which will grow can be determined from all the positive  $\omega_q$  in Fig. 1.7. For zero diffusivity in the solid and for a phase diagram with parallel Solidus and Liquidus lines ( $k = 1$ ), the expression takes the following form [11]:

$$\begin{aligned} \frac{\omega_q l_D^2}{D} &= gl_D \left( 1 - \frac{l_D}{l_T} - d_0 l_D q^2 - \frac{1}{gl_D} \right) \\ gl_D &= 1 + \sqrt{1 + (ql_D)^2} \end{aligned} \quad (1.13)$$

This analysis depends on three length scales. The definition of these length scales, namely, diffusion ( $l_D$ ), thermal ( $l_T$ ) and capillary ( $d_0$ ) are given below:

$$l_D = \frac{D}{V}, \quad (1.14)$$

$$l_T = \frac{(-m)\Delta c_0}{G}, \quad (1.15)$$

$$d_0 = \frac{\gamma_{SL}T_M}{L(-m)\Delta c_0}. \quad (1.16)$$

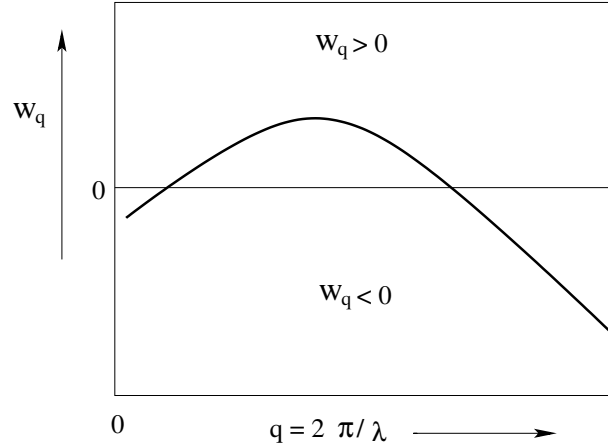


Figure 1.7: Plot of  $w_q$  given by Eq. (1.13) for different wavenumbers  $q$  (schematic)

This formula describes the basic mechanism of diffusion controlled pattern formation in crystal growth. In essence, this consists of a destabilizing part, the diffusion length  $l_D$ , leading to positive  $\omega_q$  and a stabilizing part controlled by the capillary length  $d_0$ . The marginally stable mode is marked by the combinations of  $d_0 l_D$ , which are most conveniently expressed as for a limit of  $q l_D \gg 1$  and  $l_T \gg l_D$ :

$$\lambda_{MS} = 2\pi\sqrt{l_D d_0}. \quad (1.17)$$

This is sometimes referred as the “stability length” for diffusion generated ripples on the S-L interfaces [5]. Note that, the fastest growing wavelength from the Eq. (1.13) can be determined as:  $\lambda_f \approx \sqrt{3}\lambda_{MS}$ , which is a useful measure of the typical lengths that arise during diffusional pattern formation [5, 4] (see Fig. 1.8).

Strictly speaking, among all the parameters related to the morphological instability,  $G$  and  $\gamma_{SL}$  are the stabilizing components and  $V$  is the destabilizing component to the S-L

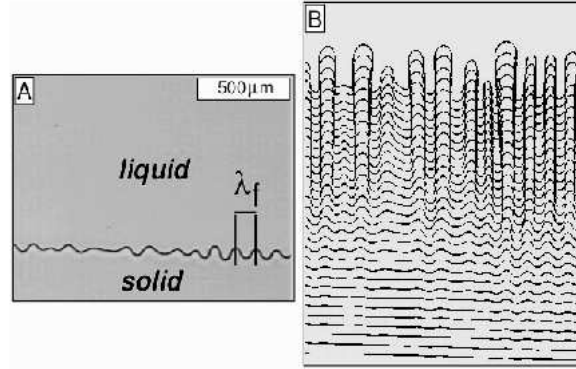


Figure 1.8: Experimental observation of the growth of a planar S-L interface into cells. The experiment is performed for a sample of 0.25% poly(ethylene oxide) in succinonitrile with a pulling speed  $V = 1.34 \mu\text{m}/\text{s}$  (adapted from [7])

planar shape. As we increase  $V$ , at a critical  $V$ , namely CS velocity  $V_{CS}$ , stabilizing effects of  $G$  are overcome. This gives the classical macroscopic criteria of CS (Eq. (1.10)). The Mullins and Sekerka (MS) critical velocity  $V_{MS}$  signifies the onset when the stabilizing effect of the  $\gamma_{SL}$  is also overwhelmed. The exact form of Mullins-Sekerka threshold can be expressed as:

$$V_{MS} = \frac{D}{l_T} \left( 1 + 3 \left( \frac{K}{2} \right)^{2/3} \left( \frac{d_0}{l_T} \right)^{1/3} \right) \quad (1.18)$$

### 1.3 Solidification of multiphase alloys: Eutectic solidification

The phase diagram in Fig. 1.9 represents a eutectic phase diagram of a two-component (A and B) liquid: an alloy of eutectic composition  $C_E$  solidifies below the eutectic temperature  $T_E$  into two chemically distinct solids – one is enriched with A atoms ( $\alpha$ -phase) while the other is with B atoms ( $\beta$ -phase) [12, 13]. In most metallic eutectic systems, the S-L interfaces of these phases are non-faceted in nature and they appear rough at the atomic scale. In a eutectic microstructure, these phases appear as lamella-like or rod-like depending on the volume fraction of the constituting phases [14, 1]. If the volume fraction of the minor phase is  $< 0.3$ , rod-like morphologies appear with the minor phase dispersed

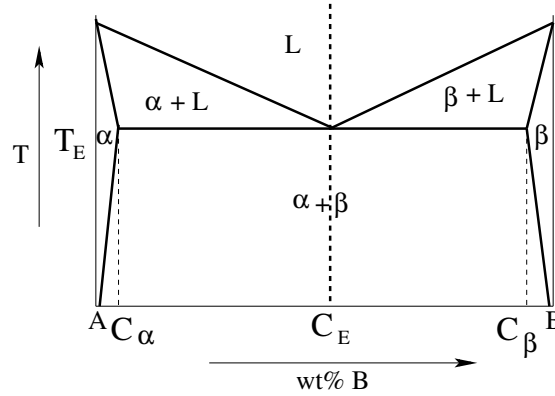


Figure 1.9: A schematic eutectic phase diagram.  $C_E$  and  $T_E$  are the eutectic composition and temperature, respectively

in the continuous matrix of the major phase, while the minor phase with a volume fraction of more than 0.3 results in lamellar morphologies (refer to Fig. 1.10). In the present work, we focus on the lamellar eutectic structures only.

In lamellar solidification, alternate plates of  $\alpha$  and  $\beta$  phases appear in the microstructures and, then, they grow next to each other by the mutual solute diffusion in between the liquid regions in front of each phase; this is called the co-operative growth or coupled growth [15]. Note that such growth behaviour exists for rod eutectics also. When both eutectic components are faceted, the growth conditions are no longer coupled and the resulting structure is a random mixture of the two phases yielding an irregular eutectic microstructure, as in Fig. 1.10. Moreover, in the presence of ternary impurities, cellular eutectic growth occurs and eutectic colonies result [16]. For a three-component ternary eutectic system, the morphologies which appear can be very complex [17, 18]. Excellent reviews of eutectic solidification can be found in [1, 2, 3, 19].

A sketch of the mutual solute diffusion paths are shown in Fig. 1.11a. Three phases –  $\alpha$ ,  $\beta$  and  $L$  – are bounded by two S-L interfaces,  $\alpha L$  and  $\beta L$ , and one S-S interface,  $\alpha\beta$ , which are shown in Fig. 1.11b. In addition to these, there is a unique singular point in the microstructure where all the interfaces meet – a trijunction point. At this point, the surface tension vectors of the respective interfaces balance to zero resulting into a mechanical equilibrium:

$$\gamma_{\alpha L}\hat{t}_{\alpha L} + \gamma_{\beta L}\hat{t}_{\beta L} + \gamma_{\alpha\beta}\hat{t}_{\alpha\beta} = 0, \quad (1.19)$$

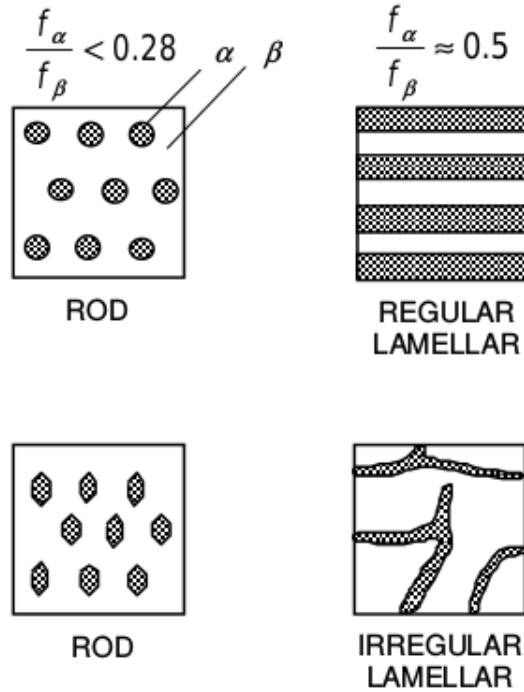


Figure 1.10: Regular and irregular eutectic morphologies (adapted from D. M. Stefanescu [2])

where  $\hat{t}_{ij}$  are the unit vectors tangent to the  $i - j$  interfaces at the triple-point, and pointing away from the triple-point. This is sometimes referred to as Young's law. This law sets the shapes as well as the contact angles of the S-L interfaces relative to a flat interface [2] (refer to Fig. 1.11b).

Every eutectic microstructure is defined by a set of length scales. Total undercooling of the S-L interfaces can be approximately written as [5]:

$$\Delta T = T_E \left\{ a_I \frac{\lambda}{l_D} + a_K \frac{d_0}{\lambda} \right\}, \quad (1.20)$$

where  $a_I$  and  $a_K$  are dimensionless constants that depend only on material parameters. Analogous to Eq. (1.4), the first term in Eq. (1.20) is due to the diffusion and the second term is due to the S-L interfacial curvature correction (Gibbs-Thomson effect). Plotting this function with respect to  $\lambda$ , we find a  $\lambda$  corresponding to the minimum undercooling of the system for which  $\frac{\partial \Delta T}{\partial \lambda} = 0$  (refer to Fig. 1.12).

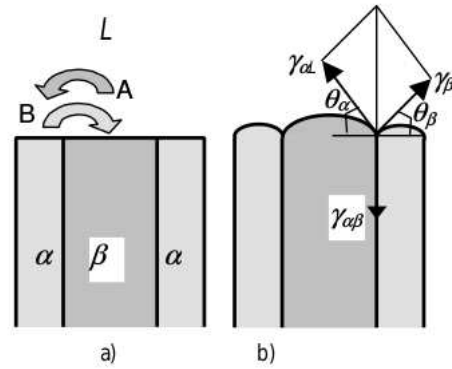


Figure 1.11: Solute diffusion paths leading to the lamellar sequence of  $\alpha$  and  $\beta$  phases (adapted from D. M. Stefanescu [2])

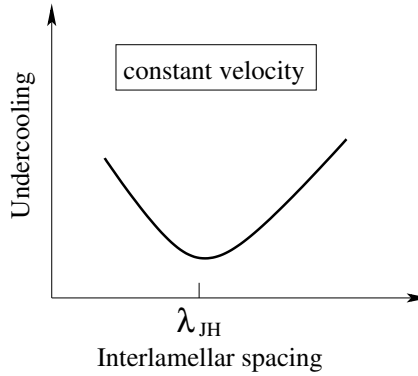


Figure 1.12: Front undercooling vs. lamellar spacing for a eutectic front: Jackson-Hunt(JH) minimum undercooling criteria

$$\lambda_{JH} \sim \sqrt{l_D d_0} \quad (1.21)$$

This has been verified by the experiments [14] as well as by the theories [20, 21]. This leads to the famous relationship between inter-lamellar spacing and the growth rate  $V$  for a regular eutectic [14]:

$$\lambda^2 V = \text{constant}. \quad (1.22)$$

For Eutectic microstructures, this characteristic inter-lamellar spacing is defined as  $\lambda_{JH}$  (JH stands for Jackson-Hunt). If the processing conditions of eutectic reaction are such that the length scales of the resulting microstructures are other than  $\lambda_{JH}$ , then, they are characterized using a function of reduced lamellar spacing  $\Lambda = \lambda/\lambda_{JH}$ .

These micro-structures have been well-identified by (quasi-2D) thin-sample directional solidification experiments [22, 23], and also by numerical simulations [21]. If there are interactions between multiple lamellae in the system, spacing adjustment processes like lamella elimination or lamella nucleation are activated in the system until a steady state is achieved. As we depart further from  $\lambda_{JH}$ , a tilt instability is seen with an asymmetry between phases, inducing a lateral drift of the lamellae [24]. Moreover, in the order of  $\Lambda \approx 2$ , oscillatory instabilities appear in the microstructures with a periodicity of  $1 - \lambda$  or  $2 - \lambda$  [22]. In bulk samples, a zigzag instability is seen at  $\Lambda \geq 1.2$ , and a wavy lamellae state results [25]. It is useful to mention here that these stability limits depend on the composition of the solidifying alloy.

## 1.4 Surface tension anisotropy: Origin and Effects

A brief account on the microscopic origin of the surface tension for faceted interfaces is given here. In the context of solidification, ordered solid phases emerge from the disordered liquid, and, thereafter, grow as stepped atomic layers where each layer is a minimum energy closed-packed plane [13, 26]. During this process, if a crystal plane forms at an angle  $\theta$  to this closed packed plane, it will contain broken bonds in excess of the closed packed plane due to the atoms at the steps. This is the essence of excess surface free energy or interfacial energy ( $\gamma$ ). In this way,  $\gamma$  can vary across the whole surface of the crystal depending on the local orientation of a particular atomic plane (Fig. 1.13).

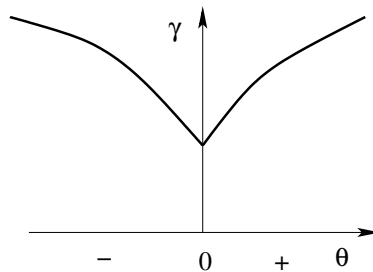


Figure 1.13: Variation of surface energy as a function of  $\theta$  around a facet

Note that, the closed packed orientation ( $\theta = 0$ ) lies at the cusped minimum in the

$\gamma - \theta$  plot. The classic method for plotting such variation of  $\gamma$  with respect to the interface orientation ( $\theta$ ) is known as Wulff's method [27]: constructing a surface about an origin such that the free energy of each plane is equal to the distance between the surface and the origin when measured along the normal to the plane. This type of polar representation of  $\gamma$  is known as  $\gamma$ -plot and has the useful property of being able to predict the equilibrium shape of a isolated single crystal.

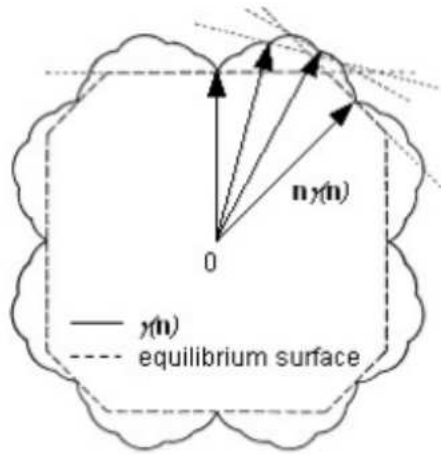
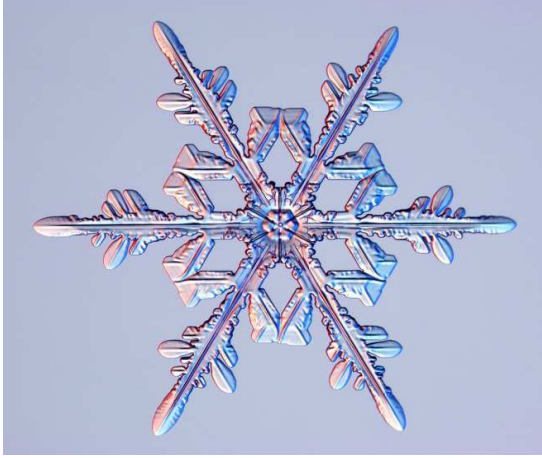


Figure 1.14: Surface tension ( $\gamma$ ) profile of an isolated solid, and the equilibrium crystal shape (adapted from [28])

A minimal representation of the Wulff's construction is depicted in Fig. 1.14. Here, the outer envelope describes the (polar) surface tension profile of an isolated solid in which  $\gamma$  is the measure of the distance between the surface and the center of the crystal  $O$ . If this solid is bounded by several planes of areas  $A_1, A_2, A_3$ , etc., with energies  $\gamma_1, \gamma_2, \gamma_3$ , etc., then, the equilibrium crystal shape or the energy minimising shape of this solid is obtained by minimising  $\sum A_i \gamma_i$  under the constraint of constant volume of the crystal. Note that, a large set of planes can be drawn perpendicular to the  $\hat{n} \gamma(\hat{n})$  passing through the  $\gamma$  surface. The equilibrium shape is simply the inner envelope of all these planes, the dotted polyhedron in Fig. 1.14. In addition, the solid  $\gamma(\hat{n})$  profile in Fig. 1.14 have cusps, which, in equilibrium, become flat facets of the polyhedron at a distance minimum to the centre of the crystal. This represents a minimum energy orientation or favourable



orientation in the resultant microstructure. However, such Wulff shape only relates the  $\gamma$ -plot to the equilibrium crystal shape, and, hence, does not include the kinetics of the process.



(a) A snowflake



(b) A dendrite

Figure 1.15

Because of their aesthetics, snowflakes have attracted human curiosity for ages. This is a naturally abundant crystal, which forms due to a complex interaction between crystallization and anisotropy (refer to Fig. 1.15(a)). In the context of directional solidification of single-phase alloys, dendrites are another classic example. To obtain a strong crystallographic morphology like in Fig. 1.15(b), the simplest cubic anisotropic form must include a four-fold symmetry, in the surface free energy of the underlying (cubic) structure of the growing solid, which takes the following shape in polar and Cartesian coordinate systems, respectively,

$$\gamma(\theta) = \bar{\gamma}(1 + \epsilon_4 \cos(4\theta)) \quad (1.23)$$

$$\gamma(\hat{n}) = \bar{\gamma}(1 + \epsilon_4(\hat{n}_x^4 + \hat{n}_y^4)) \quad (1.24)$$

$\hat{n}_x$  and  $\hat{n}_y$  are the Cartesian components of a unit vector normal to the interface.  $\gamma$  is the anisotropic surface tension and  $\bar{\gamma}$  is a constant.  $\epsilon_4$  is the anisotropy parameter which gives the strength of the surface tension variations and induces the minimum and maximum

energy directions in the system. Note that, analytical comparison between the equilibrium shapes and the calculated Wulff shapes can lead to an useful measure of  $\epsilon_4$ . The polar form of such  $\gamma$  function is plotted in Fig. 1.16. It is worthwhile to mention here that to simulate a snowflake, we need a six-fold symmetry in the anisotropic surface tension as follows:

$$\gamma(\theta) = \bar{\gamma}(1 + \epsilon_6 \cos(6\theta)) \quad (1.25)$$

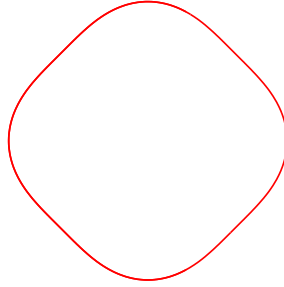


Figure 1.16: Cubic anisotropy with a four-fold symmetry:  $\gamma = \bar{\gamma}[1 + 0.06 \cos(4\theta)]$ .

Note that, in the previous case, the equilibrium shape is contained well within the surface tension envelope in Fig. 1.14. This signifies that, all the orientations represented by the equilibrium shape are energetically stable. Mathematically, this is described by the positive surface stiffness parameter,  $\gamma + \frac{d^2\gamma}{d\theta^2}$  (or,  $\gamma + \gamma''$ ),  $\theta$  is the local interface orientation angle. However, if the magnitude of the anisotropy becomes so large that the energy of some orientations ( $\theta$ ) becomes very high, these directions are not present in equilibrium microstructures. They are called missing orientations, which are described by a negative surface stiffness and can be calculated analytically using the Cahn-Hoffman surface tension vector ( $\vec{\xi}$ ) construction [29]. This is equivalent to the Wulff-construction in order to determine the equilibrium shape of a crystal of surface energy  $\gamma$  [29]. A set of  $\vec{\xi}$  vectors define the equilibrium shape of a crystal in an elegant way. The  $\vec{\xi}$ -vector is defined as the gradient of the scalar field  $r$  because it applies normal to the  $\gamma$  surface. In polar coordinate system, unit normal vectors are given by their components  $\cos\theta$  and  $\sin\theta$  for (Cartesian)  $x$ - and  $y$ - directions respectively. This leads to the following useful definitions

in two dimensions:

$$\vec{\xi} = \vec{\nabla}(\hat{n}\gamma) \quad (1.26)$$

$$\vec{\xi} = \gamma\hat{n} + \gamma'\hat{t} \quad (1.27)$$

$$\hat{t} = \frac{\partial\hat{n}}{\partial\theta} \quad (1.28)$$

$$\begin{pmatrix} \xi_x \\ \xi_y \end{pmatrix} = \begin{pmatrix} \gamma(\theta)\cos\theta - \gamma'(\theta)\sin\theta \\ \gamma(\theta)\sin\theta + \gamma'(\theta)\cos\theta \end{pmatrix} \quad (1.29)$$

Consider an isolated particle embedded in a matrix is growing under the influence of an cubic anisotropy function with a four-fold symmetry. If the strength of the anisotropy is such that  $\gamma + \gamma''$  remains positive, the corresponding  $\gamma$  function (red) and the equilibrium shape (blue) is shown using a  $\vec{\xi}$ -vector plot in Fig. 1.17; these curves are smooth and continuous in space. However, if the anisotropy strength becomes so high that  $\gamma + \gamma''$  is no longer positive, there exists a range of high energy orientations, missing from the equilibrium shape of the crystal: they appear as “ears” in the  $\vec{\xi}$ -vector plot [30] (Fig. 1.17). Note that, the equilibrium shape or the Wulff shape, in the  $\vec{\xi}$ -vector representation, is given by the blue dotted curve without the “ears”. In such situations, the equilibrium shape becomes convex signifying the onset of sharp corners and edges in the equilibrium microstructures.

In the present thesis, we describe the surface tension of the system using a  $\vec{\sigma}$ -vector notation rather than a  $\vec{\xi}$  vector.  $\vec{\sigma}$  vector lies in the plane with a line of unit vector (say)  $\vec{l}$ .  $\vec{l}$  applies along the triple line (normal to the page in 2D) and related to the  $\vec{\xi}$  vector in the following way [31],

$$\vec{\sigma} = \vec{\xi} \times \vec{l}. \quad (1.30)$$

So, the  $\vec{\sigma}$  (normal to  $\vec{\xi}$ ) can be written in two dimensions as:

$$\vec{\sigma} = \gamma\hat{t} - \gamma'\hat{n} \quad (1.31)$$

$$\begin{pmatrix} \sigma_x \\ \sigma_y \end{pmatrix} = \begin{pmatrix} \gamma(\theta)\sin\theta - \gamma'(\theta)\cos\theta \\ \gamma(\theta)\cos\theta + \gamma'(\theta)\sin\theta \end{pmatrix} \quad (1.32)$$

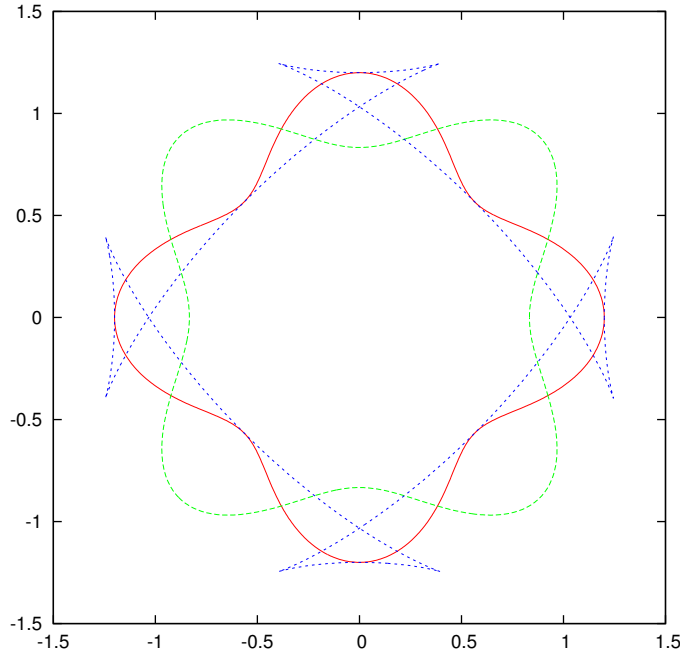


Figure 1.17: Parametric Plots: Red:  $\gamma$  plot; Green:  $1/\gamma$  plot; Blue:  $\vec{\xi}$  plot

In essence, the anisotropy function representation in terms of  $\vec{\xi}$ -vector or  $\vec{\sigma}$ -vector are equivalent.

Since anisotropy comes into play in the balance of capillary forces at the interface, in directional solidification, in addition to the pulling speed and the thermal gradient, crystalline anisotropy is also an important parameter to determine the steady state microstructures. In addition to this, changing the angle ( $\theta_R$ ) between the crystalline axis and the pulling direction modifies the anisotropy  $\gamma(\theta)$  functions operating in the growth plane [22]. This fact can easily be exploited using a relatively recent experimental technique known as rotating directional solidification, which is elaborated in Sec. 1.5.

Moreover, atomistics of the emerging interfaces can also influence the evolution of the solidification microstructures, particularly on the orientation development of the steady state structures [32]. In other words, the effects of anisotropy in the S-L interfaces may not bear the same role for S-S interfaces. During dendritic solidification, the crystal seed grows into the liquid, and the growth direction of it is selected by the anisotropy in the S-L interface. Such orientation selection during dendritic solidification is illustrated in experiments as well as in numerical simulations to describe the transition from a

dendrite to seaweed and fractal-like structure [33, 34, 35, 36, 37, 38]. In addition to these, competition between different orientations has also been studied to shed some light on the development of a preferred crystallographic direction during dendritic solidification [39, 40]. However, little is known about the orientation development in lamellar eutectic growth patterns. A recent experiment by Akamatsu et al. [41] suggests that the orientation of a growing lamella is influenced by the S-S boundary anisotropy. Motivated by this work, in the present thesis, we aim to explore the effects of S-S boundary anisotropy on the directional solidification microstructures. Furthermore, while the measurement of anisotropic  $\gamma$  functions (Eq. (1.23)) of the S-L interfaces has gained significant attention in the experiments as well as in the numerical calculations [42, 43, 44], little is known about these functions for S-S interfaces [45].

S-S boundary surface tension anisotropy plays an important role in eutectic solidification. First of all, in reality, all eutectic microstructure possess some degrees of anisotropy depending on the symmetry of the underlying crystal structure of the material. Second, in anisotropic regime the lamellar growth no longer relies on the simple isotropic energy considerations or the Young's law. Hence, the stability of the steady state patterns, which arise during the eutectic solidification with isotropic energies, as well as the laws of spacing-selection need to be revisited. Finally, one can obtain plenty of novel morphologies, in addition to the "normal" lamellar and rod-like morphologies, with a revised dependency on the phase fractions of the containing phases. In metallic alloys, although the most important form of the anisotropy is a (cubic) four-fold one, experimental measurements reveal that there can also be a significant contribution from non-fourfold anisotropies, particularly, two-fold [46, 6]; this has been investigated in more detail in the present thesis.

It is useful to mention here that, in the presence of S-S boundary anisotropy, surface tension balance at the triple point does not obey the isotropic Young-condition (Eq. (1.19)) anymore and, instead, follows the anisotropic Young-Herring equation [45]. This combines the anisotropic  $\vec{\sigma}$ -vector (Eq. (1.31)) along the S-S boundaries with the isotropic surface tensions (Eq. (1.19)) along S-L boundaries resulting into following expression:

$$\gamma_{\alpha L} \hat{t}_{\alpha L} + \gamma_{\beta L} \hat{t}_{\beta L} + \vec{\sigma} = 0 \quad (1.33)$$

This is further detailed in Chapter 3.

## 1.5 Rotating directional solidification (RDS)

Horizontal directional solidification using the Bridgman method as described in Sec. 1.2.1 can be performed with yet another degree of freedom, i.e., rotating the solidification set-up placed in a unidirectional thermal gradient while solidification is in progress. A rotating coordinate frame is attached to the solidification table and the sample is rotated at an angle of  $\theta_R$  with respect to the thermal gradient  $G$ .

The details of this experimental method can be found in [41]. We only detail the essence of this method in Fig. 1.18. A sample is placed in the center of the rotating solidification table, which is rotated by a motor at a constant angular velocity  $\omega = \frac{d\theta_R}{dt}$ , or until a certain orientation  $\theta_R$  is reached. A hot block of temperature above the melting point and a cold block below the melting temperature are placed across the table to generate a fixed temperature gradient similar to the linear directional solidification. To initiate growth, the sample is completely melted first and, then, quenched to generate a number of grains. Once a grain of particular orientation is selected, the growth of it is followed in the rotating frame with a rotation angle of (say)  $\theta_R$ . Note that, after each half rotation cycle, the sample melts and, hence, a number of runs are needed to obtain a micrograph like Fig. 1.18d, which contains the solidification history. The essence of this rotation is schematically shown in Fig. 1.19.

This exciting, relatively recent, technique has many unique advantages over horizontal directional solidification. The 2-D micrographs obtained in this method are “mathematically” proved to be analogous to the equilibrium interface shapes or Wulff shapes of the solid-solid boundaries [45]. In addition, we can follow the change in morphology of the solidifying grain, as well as the tilt angle of the interfaces with a change in the sample orientation introduced by a rotation of  $\theta_R$ . Note, this method covers all the orientations

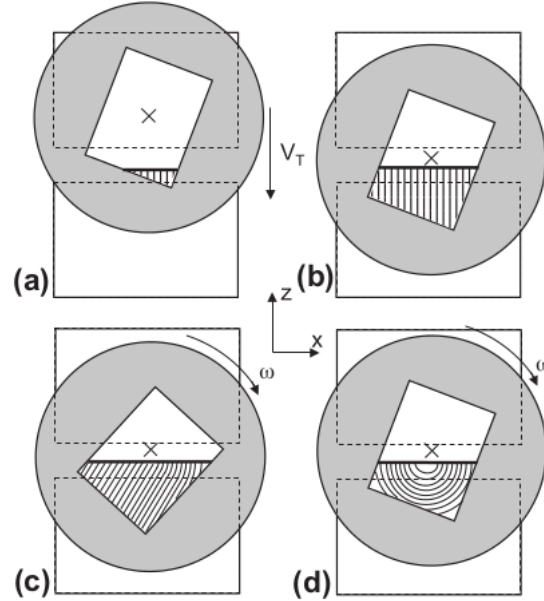


Figure 1.18: A rotating directional solidification run: (a) seed crystal and grain selection (b) directional solidification (c) start of RDS run (d) after long run. Empty rectangles are the hot and cold blocks and X is the center of rotation (Adapted from Akamatsu et. al[41])

between 0 to  $2\pi$  in the sample plane. Moreover, changing the angle ( $\theta_R$ ) between the crystalline axis and the pulling direction induces an effective anisotropy in the growth plane [22]. Therefore, this method is well suited to examine the S-S boundary anisotropy driven pattern formation systems, such as lamellar eutectics. This will be illustrated in chapter 3.

## 1.6 Numerical methods

There are two basic methods to study solidification microstructures — sharp-interface and diffuse-interface approaches. In the sharp-interface approach, one needs to implement the equations described in Sec. 1.2.1 using sharp-interface methods, such as boundary-integral [4, 21]. This solves for a mathematically sharp interface in between the solid and liquid using complex boundary conditions at the interface. So, one needs to find the interface positions explicitly using this approach. The problems of front tracking do not arise in case of diffuse-interface approaches.

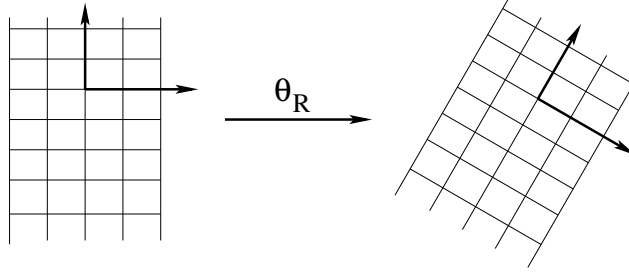


Figure 1.19: Representational rotating coordinate frame

In diffuse interface models, an order parameter  $\phi$  is introduced to distinguish between liquid ( $\phi = 0$ ) and solid ( $\phi = 1$ ).  $\phi$  is a continuous function in space with a relatively smooth region where  $0 < \phi < 1$  in between the bulk phases describing the interfaces. We need a free energy description of the system, and minimising this free energy with respect to the conserved ( $c$ ) and non-conserved ( $\phi$ ) quantities of the system, we obtain the equations of motion concerning the microstructure evolution [47, 48, 49, 50].

However, the solidification morphologies obtained using these evolution equations do not provide a quantitative comparison with a real alloy system. The reason is that the characteristic natural thicknesses of diffuse S-L interfaces are much smaller than the solidification patterns. Hence, in order to resolve both scales at the same time, the thickness of the interfaces has to be enlarged numerically [51]. This may lead to certain non-physical behaviours in the systems, like solute-trapping. Therefore, in order to use this model, in a sense of comparison with the experimental results in a quantitative spirit, one has to relate these model equations to the sharp-interface equations using a proper asymptotic analysis [52]. The details of these diffuse interface models can be found in recent reviews [50],[53],[54].

Initially, thermodynamically-consistent “simple” phase-field models with single phase-field variable were developed to describe the phase transitions in a binary system [55, 56, 57, 58, 59]. In recent times, they have been extended to accommodate arbitrary number of phases in a multi-component setting, utilizing a vector field description of the order parameter. These multiphase, multicomponent models have been introduced and



developed by Steinbach and co-workers [60, 61, 53], Nestler and co-workers [62, 63, 64], Wheeler [65], Kim et al. [66], Plapp [51], Cogswell and Carter [67] etc. We will adopt here a quantitative model in the line of Choudhury and Nestler, which uses the chemical potential instead of the composition to describe the conserved field of the system. The details of this model are given in chapter 2.

## 1.7 Thesis Outline and motivation

The goal of this thesis is to study the influence of S-S interface anisotropy on solidification patterns, with the help of phase-field simulations. Our results will be systematically compared to experiments.

In chapter 2, at first, the sharp-interface equations are described. Next, we provide an introduction to the phase-field modeling technique and, then, detail the phase-field model used in the present work. This is followed by a brief review of the methods used to relate the phase-field equations to the sharp-interface equations.

Chapter 3 is devoted to the simulations of thin lamellar eutectics. In directional solidification of binary eutectics, it is often observed that two-phase lamellar growth patterns grow tilted with respect to the direction  $z$  of the imposed temperature gradient (Fig. 1.20). This crystallographic effect depends on the orientation of the two crystal phases  $\alpha$  and  $\beta$  with respect to  $z$ . Recently, an approximate theory was formulated that predicts the lamellar tilt angle as a function of the anisotropy of the free energy of the solid( $\alpha$ )-solid( $\beta$ ) interphase boundary. We use two different numerical methods – phase-field (PF) and dynamic boundary-integral (BI) – to simulate the growth of steady periodic patterns in two dimensions as a function of the angle  $\theta_R$  between  $z$  and a reference crystallographic axis for a fixed relative orientation of  $\alpha$  and  $\beta$  crystals, that is, for a given anisotropy function (Wulff plot) of the interphase boundary. For Wulff plots without unstable interphase-boundary orientations, the two simulation methods are in excellent agreement with each other, and confirm the general validity of the previously proposed theory. When unstable orientations are present in the Wulff plot, it is expected that two distinct values of the tilt angle can appear for the same crystal orientation over a finite  $\theta_R$ .

range. This bistable behaviour, which has been observed experimentally, is well reproduced by BI simulations, but not by the PF model. Possible reasons for this discrepancy are discussed.

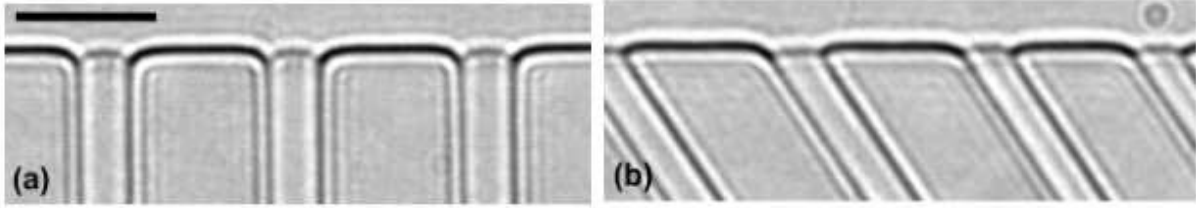


Figure 1.20:  $\text{CBr}_4\text{-C}_2\text{Cl}_6$  lamellar eutectic formation in the (a) absence of anisotropy (b) presence of anisotropy (adapted from Akamatsu et al. [41]). The two micrographs are taken from two different eutectic grains. Bar:  $20\ \mu\text{m}$ .

Chapter 4 deals with bulk lamellar eutectics. We use a phase-field model to simulate the eutectic microstructures of a generic binary alloy in three dimensions for different anisotropy functions. Solid-solid interphase anisotropy was found to be sufficient to describe the dynamics of lamellar eutectic growth in this regime. In the absence of anisotropy, a labyrinth of lamellae forms. While a four-fold anisotropy produces a wealth of complex microstructures, two-fold anisotropy produces a regular lamellar array; a possible mechanism for the development of preferred orientations has been discussed (see Fig. 1.21). Moreover, we perform simulations with competing eutectic grains in which steady state morphologies are found to be consistent with the interphase energy considerations. Finally, a possible mechanism has been proposed in regard to the transformation of labyrinths into regular arrays.

In Chapter 5, we study the orientation development of an anisotropic GB during unidirectional solidification of a dilute binary alloy. In particular, we increase the solidification rate  $V$  from 0 to cellular-instability threshold, and follow the response of the GB towards its orientation selection. Below the constitutional supercooling limit, the GB grows at a finite angle, and then, it follows a gradual or sharp transition towards the growth axis depending on the intensity of the morphological instability. In this regime, the GB profile is found to be greatly influenced by the GB mobility. Finally, we shed some light on

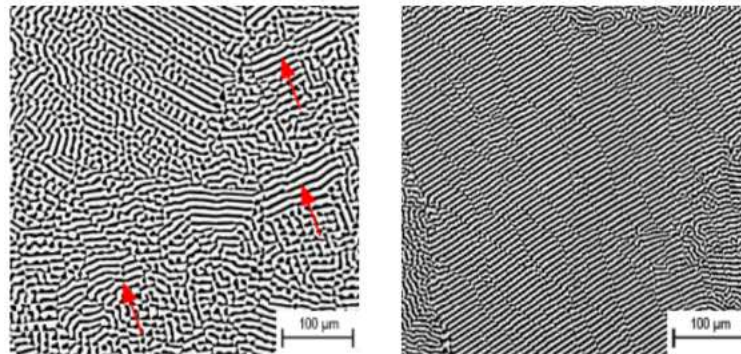


Figure 1.21: Transformation of an disordered lamellar arrays or labyrinths towards a regular lamellar arrays with a preferred orientation in the bulk eutectic sample (adapted from Hecht et al. [68])

orientation selection in the presence of multiple GBs with different energy minima.

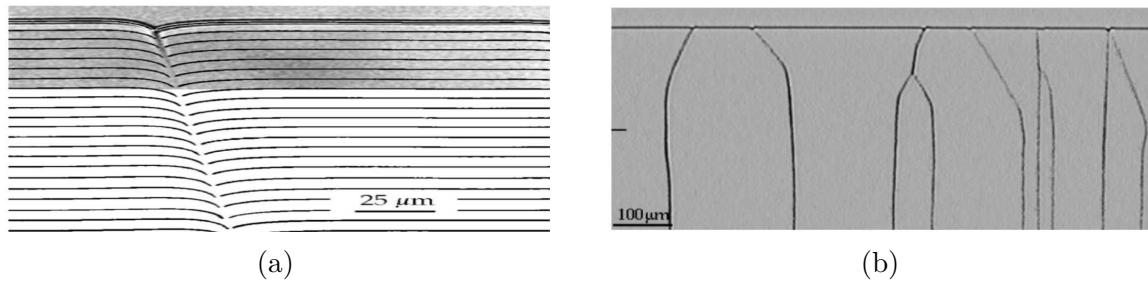


Figure 1.22: Orientation of a low-angle GB (a) below CS velocity (b) above MS velocity. Note that, in figure (b) the bottom part of the GB has been solidified above MS velocity; then a downward velocity jump in the experiment makes the GB to orient at an angle in the low velocity regime (adapted from Bottin et al. [69])

Finally, in Chapter 6, an overall conclusion is drawn from the results of the previous chapters, and a perspective is given for the future work.

# Chapter 2

## Simulation Methods

In this chapter, we first describe the differences between a sharp-interface and a diffuse-interface approach in materials modeling techniques. Next, we briefly outline the sharp-interface method equations. Finally, we describe the basic phase-field method equations before elaborating on the details of the model used in our present study.

Consider the problem of solidification where a liquid is solidifying into one or several solids. In this process, one bulk phase (liquid) transforms into other bulk phases (solid) leaving an intermediate region in between them, which is termed an interface. In sharp interface approaches, such interfaces are described mathematically as of zero width, and one needs to solve complex boundary conditions to track this interface. However, the experimental electron microscopy images or the atomistic simulations using molecular dynamics methods confirm that the interfacial region is several atomic layers thick. This means that the interfaces that form in real materials between two bulk phases are smooth and continuous. This concept has been assimilated in the phase-field modeling techniques, where interfaces have been given a finite thickness. Hence, the phase-field modeling suits better for the understanding of microstructure evolution of solids. In this technique, the whole microstructure is described using a scalar field value  $\phi$ , which is called the order parameter. In the context of solidification, the order parameter  $\phi$  is 0 in the liquid and 1 in the solid and, thus, the region in between is defined by  $0 < \phi < 1$ . This range defines an interface in the microstructure, and the region over which it changes is called the width of

the interface. A schematic representation of a sharp-interface and a diffuse-interface is presented in Fig. 2.1. A comparison between the sharp interface and the diffuse interface model equations can be found in [58].

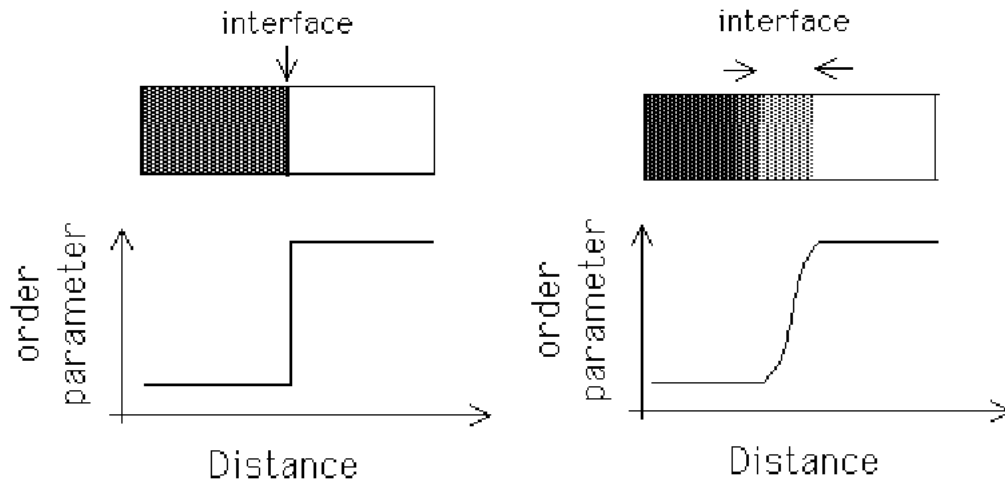


Figure 2.1: (left) A sharp interface and (right) a diffuse interface (adapted from Sin et al. [47])

## 2.1 Sharp-interface problem

The sharp interface equations are already described in chapter 1. In the present section, we explain how these equations are rendered dimensionless and utilized to study a eutectic solidification problem referring to the phase diagram in Fig. 1.9.

Consider the directional solidification of a binary eutectic alloy in an externally imposed temperature gradient  $G$  along the  $z$  axis with a fixed pulling velocity  $V$ . We make the approximation that the temperature field is independent of the S-L front shape (frozen-temperature approximation), which is a good approximation for thin-sample solidification in which heat conduction takes mainly place in the sample walls. In a two-dimensional system (an appropriate model for thin-sample directional solidification) in which the

temperature gradient is directed along the  $z$  axis, the temperature field is hence given by

$$T(\vec{x}, t) = T_E + G(z - Vt), \quad (2.1)$$

where we have chosen the origin of the  $z$  axis at the eutectic temperature  $T_E$  at time  $t = 0$ , and  $\vec{x}$  is a position vector in the  $(x, z)$  plane.

A dimensionless concentration field  $u$  is introduced,

$$u(\vec{x}, t) = \frac{c(\vec{x}, t) - c_E}{c_\beta - c_\alpha}, \quad (2.2)$$

where  $c(\vec{x}, t)$  is the space- and time-dependent composition of the alloy, and  $c_E$ ,  $c_\alpha$ , and  $c_\beta$  are the equilibrium compositions of the three phases (liquid, solid  $\alpha$  and solid  $\beta$ ) that are in coexistence at  $T = T_E$ . In the one-sided model of solidification, this field obeys the diffusion equation in the liquid with the diffusivity  $D$ ,

$$\partial_t u = D \vec{\nabla}^2 u, \quad (2.3)$$

whereas no diffusion takes place in the solid. At the S-L interfaces, the conservation of solute implies

$$V_n u_i = -D \hat{n} \cdot \vec{\nabla} u, \quad (2.4)$$

where  $V_n$  is the normal growth velocity of the interface,  $u_i = (c_i - c_E)/(c_\beta - c_\alpha)$  for  $i = \alpha, \beta$ , and  $\hat{n}$  is the unit normal vector to the interface pointing into the liquid. In writing down this expression, we have made the simplifying assumption that the concentration differences between the phases do not depend on temperature (parallel Liquidus and Solidus lines).

For isotropic interfaces, the classic problem of eutectic growth is completed by the local equilibrium condition,

$$u_{\text{int}} = \begin{cases} -(\zeta(x) - Vt)/l_T^\alpha - d_0^\alpha \kappa, & \alpha\text{-L interface} \\ (\zeta(x) - Vt)/l_T^\beta + d_0^\beta \kappa, & \beta\text{-L interface} \end{cases} \quad (2.5)$$

Here,  $\zeta(x)$  indicates the position of the S-L interface in the  $z$  direction,

$$l_T^i = \frac{|m_i|(c_\beta - c_\alpha)}{G} \quad (2.6)$$

is the thermal length of phase  $i$ , with  $m_i$  being the liquidus slope at the eutectic point,

$$d_0^i = \frac{\gamma_{iL} T_E}{L_i |m_i| (c_\beta - c_\alpha)} \quad (2.7)$$

is the capillary length of phase  $i$ , with  $L_i$  the latent heat of melting per unit volume and  $\gamma_{iL}$  the surface free energy, and  $\kappa$  is the interface curvature, counted positive for a convex solid.

Moreover, at the trijunction point, local equilibrium implies the balance of surface tensions following the Young's law for isotropic interfaces (Eq. (1.19)). These equations are exploited in a boundary integral method, described in Chapter 3.

## 2.2 Basics of Phase Field Method

The evolution of a microstructure from a mother phase to a daughter phase is described by a free energy functional which combines the free energies of the bulk phases and the interfaces in between [70]. If the system is defined using an order parameter  $\phi$ , the minimal form of the functional becomes [54],

$$\mathcal{F} = \int_V [f(\phi, c) + \kappa_\phi (\nabla \phi)^2] dV \quad (2.8)$$

Here,  $f$  is the free energy density of the bulk phases and the second term in the functional is the gradient energy contribution from the interfaces because only at the interface the gradient of  $\phi$  is non-zero.  $\kappa_\phi$  is the gradient energy coefficient, a parameter related to the interface thickness. See Appendix A for an explanation of this coefficient.

The standard procedure is to minimise this free energy functional with respect to the field variables. There are two basic types of field variables: conserved and non-conserved. During solidification and other diffusional phase transformations, the overall composition

of the system remains constant — this is a conserved variable. Whereas, during the process of grain growth, the order parameter  $\phi$  representing the grains no longer remains constant as with time one grain overgrows the other. In this case  $\phi$  is a non-conserved variable.

For conserved type of phase field modeling, the evolution of the field variables with time is calculated from the continuity equation of local mass conservation calculating the divergence of the solute flux  $\vec{J}$  in the system. This uses a variational derivative of the functional in Eq. (2.10).

$$\frac{\partial c}{\partial t} = -\nabla \cdot \vec{J} \quad (2.9)$$

$$\frac{\partial c}{\partial t} = \nabla \cdot \left( M \nabla \frac{\delta \mathcal{F}}{\delta c} \right) \quad (2.10)$$

$M$  is a mobility parameter. On the other hand, evolution equations for non-conserved field variables such as order parameter  $\phi$  are determined from an Allen-Cahn type of equation:

$$\frac{\partial \phi}{\partial t} = -M(\phi) \frac{\delta \mathcal{F}}{\delta \phi} \quad (2.11)$$

Depending on the physics of the system, these two equations are used to determine the equilibrium microstructure of an alloy undergoing phase transformations.

## 2.3 Grand-canonical Multi-phase-field Model

For the present purpose, we have used a recent multi-phase, multi-component, grand-canonical, phase-field formulation that has been elaborated in [51, 71, 64, 72]. In essence, we start with a grand-potential functional rather than a free energy functional combining the interfacial and bulk parts of the free energy of the system and then we minimise this functional with respect to the field variables to obtain the evolution equations for the phase fields and the composition fields.

Let us consider a binary alloy that solidifies into  $\alpha$  and  $\beta$  solids. The following formulation considers:

- No solute convection in the liquid ( $l$ )



- Solute is transported in the liquid by diffusion only
- Diffusion in the solids is ignored (one-sided model)
- Diffusion of solute in the liquid is described by the chemical potential field  $\mu$ , conjugate to the composition variable  $c$

$N = 3$  phase fields, namely,  $\phi_\alpha$ ,  $\phi_\beta$  and  $\phi_l$ , equivalent to the local volume fractions, describe the system and obey the constraint:

$$\sum_{i=1}^N \phi_i = 1. \quad (2.12)$$

The grand potential functional combines the interface and bulk free energies and takes the following form:

$$\Omega = \int \left[ \epsilon a(\phi, \nabla \phi) + \frac{1}{\epsilon} w(\phi) + \omega(T, \mu, \phi) \right] dV, \quad (2.13)$$

where  $\epsilon$  is a length scale parameter related to numerical interface thickness.  $a(\phi, \nabla \phi)$  is the gradient energy density which reads as:

$$a(\phi, \nabla \phi) = \sum_{i < j}^N \bar{\gamma}_{ij} [a_c]^2 |q_{ij}|^2. \quad (2.14)$$

$q_{ij}$  is a vector normal to the  $ij$  interface and expressed as:

$$q_{ij} = \phi_i \nabla \phi_j - \phi_j \nabla \phi_i. \quad (2.15)$$

In Eq. (2.14),  $\bar{\gamma}_{ij}$  is a constant and  $a_c$  is the anisotropy function. Isotropic interfaces are described by  $a_c = 1$ . For anisotropic interfaces,  $a_c$  is a function of local orientation angle  $\theta$ , as explained in Chapter 1. Incorporation of anisotropy via  $a_c$  is detailed in Sec. 2.5.

$w(\phi)$  in Eq. (2.13) imparts multi-obstacle potential in the system and is expressed as:

$$w(\phi) = \begin{cases} \frac{16}{\pi^2} \sum_{i,j=1}^N \bar{\gamma}_{ij} \phi_i \phi_j + \sum_{i,j,k=1}^N \gamma_{ijk} \phi_i \phi_j \phi_k & \text{if } \phi \in \Sigma \\ \infty & \text{elsewhere,} \end{cases} \quad (2.16)$$

$\Sigma$  is bounded by  $\phi_i \geq 0$  and  $\sum_i^N \phi_i = 1$ .  $\gamma_{ijk}$  is a third order potential term which avoids appearance of any unwanted “foreign” phases in the binary interfaces.

The function  $\omega$  in Eq. (2.13) is the grand canonical potential which is obtained using the Legendre transformations of the concentration-dependent Helmholtz free energy density,  $f_i$ , of each phase,

$$\omega(\mu, T, \phi) = \sum_{i=1}^N \omega_i(\mu, T) h_i(\phi). \quad (2.17)$$

$$\omega_i(\mu, T) = f_i - \mu c. \quad (2.18)$$

The weight function  $h_i$  in Eq. (2.17) interpolates between phases and satisfies  $\sum_{i=1}^N h_i(\phi) = 1$ .

$$h_i(\phi) = \phi_i^2(3 - 2\phi_i) + 2\phi_i\phi_j\phi_k. \quad (2.19)$$

The expressions for the bulk free energies  $f_i$  are given in Sec. 2.4.

With all the elements of Eq. (2.13) detailed above, we will now derive the equations of motion for this model. First, the evolution equations for the phase-fields follows Allen-Cahn dynamics:

$$\frac{\partial \phi_i}{\partial t} = -\frac{1}{\tau \epsilon} \left[ \frac{\delta \Omega}{\delta \phi_i} - \Lambda \right], \quad (2.20)$$

where  $\tau$  is the relaxation coefficient, the value of which is chosen to make the interface kinetics vanish and attain local equilibrium at the interfaces [64]. This can be implemented as follows where  $\tau_{ij}$  applies for the relaxation constant for  $i - j$  binary interfaces.

$$\tau = \frac{\sum_{i,j=1}^N \tau_{ij} \phi_i \phi_j}{\sum_{i,j=1}^N \phi_i \phi_j}. \quad (2.21)$$

A correction in the form of Lagrange multiplier  $\Lambda$ , in Eq. (2.20), is added to maintain  $\sum_{i=1}^N \phi_i = 1$  throughout the system. This can lead some  $\phi_i$  values in the system to become less than 0 or greater than 1. We check this situation using the following procedure. If  $\phi_i$  goes below 0, we replace this with 0 and, similarly, if it goes beyond 1, we replace this value with 1. This is a standard procedure for an obstacle type of potential (Eq. (2.16)) description of the system.

In Eq. (2.20), we calculate the functional derivatives  $\frac{\delta \Omega}{\delta \phi_i}$  using the calculus of variations

in the form of Euler-Lagrange equation which can be extended easily for higher order derivatives:

$$\frac{\delta\Omega}{\delta\phi_i} = \frac{\partial\Omega}{\partial\phi_i} - \nabla \cdot \frac{\partial\Omega}{\partial(\nabla\phi_i)} + \nabla^2 \cdot \frac{\partial\Omega}{\partial(\nabla^2\phi_i)} - \dots \quad (2.22)$$

Applying Eq. (2.22) to Eq. (2.13) gives the following complete expression to be calculated to arrive at the evolution equations for the  $\phi_i$  (refer Eq. (2.20)):

$$\frac{\delta\Omega}{\delta\phi_i} = \epsilon \left[ \frac{\partial a}{\partial\phi_i} - \frac{\partial a}{\partial(\nabla\phi_i)} \right] + \frac{1}{\epsilon} \frac{\partial W(\phi)}{\partial\phi_i} + \frac{\partial\omega(T, \mu, \phi)}{\partial\phi_i}. \quad (2.23)$$

Next, the evolution equations for the concentration fields are obtained from the temporal evolution of the chemical potential field  $\mu$ , which is conjugate to the composition fields  $c_i$ . Taking partial derivatives with respect to time  $t$  on both sides of Eq. (2.17) gives

$$\frac{\partial\omega}{\partial\mu_i} = \sum_{i=1}^N \frac{\partial\omega_i}{\partial\mu_i} h_i(\phi). \quad (2.24)$$

Following the expression  $\frac{\partial\omega_i}{\partial\mu_i} = -c_i$  from Eq. (2.18), we can write

$$c = \sum_{i=1}^N c_i(\mu, T) h_i(\phi). \quad (2.25)$$

Taking partial derivatives with time  $t$  on both sides results in

$$\frac{\partial c}{\partial t} = \sum_{i=1}^N \left[ \frac{\partial c_i}{\partial\mu} \frac{\partial\mu}{\partial t} + c_i \frac{\partial h_i}{\partial t} \right]. \quad (2.26)$$

Rearranging the above expression leads to a diffusion-like equation for  $\mu$ :

$$\frac{\partial\mu}{\partial t} = \left[ \sum_{i=1}^N \frac{\partial c_i}{\partial\mu} \right]^{-1} \left[ \frac{\partial c}{\partial t} - \sum_{i=1}^N c_i \frac{\partial h_i(\phi)}{\partial t} \right]. \quad (2.27)$$

$\frac{\partial c_i}{\partial t}$  in Eq. (2.27) can be derived from the conservation of solute mass in the system resulting in a continuity equation:

$$\frac{\partial c_i}{\partial t} = -\nabla \cdot (\vec{J}_i - \vec{j}_{at}). \quad (2.28)$$

A vector  $\vec{j}_{at}$ , termed the anti-trapping current, is added to the diffusion flux  $\vec{J}$  to counteract the spurious solute trapping effects arising at the thicker interfaces and thus guarantee the correct thin interface limit [52]. The origin of this correction is explained in Sec. 1.6. The expression for diffusion flux  $\vec{J}$  which depends on the mobility  $M$  of the solute atoms are given by

$$\vec{J} = -\nabla \cdot (M\nabla\mu). \quad (2.29)$$

$M$  can be expressed in terms of interpolations between different phases as

$$M = \sum_{i=1}^N M_i g_i(\phi). \quad (2.30)$$

$g(\phi)$  is a weight function to interpolate the mobility between phases. In our present work, we choose  $h_i(\phi)$  (Eq. (2.19)) to serve the purpose of  $g(\phi)$ ; however, strictly speaking, the functions to interpolate mobilities and the grand potentials need not be the same. Finally, the mobility of the solute atoms in the individual phases can be related to the interdiffusion coefficient multiplied by  $\partial c/\partial\mu$

$$M_i = D \frac{\partial c_i}{\partial \mu_i}. \quad (2.31)$$

## 2.4 Thermodynamic description of the free energy

For the free energies  $f_i$  in Eq. (2.18) we take parabolic free energies, as detailed in [73, 72]

$$f_i = A_i(T)c^2 + B_i(T)c + C_i(T). \quad (2.32)$$

$A$ ,  $B$  and  $C$  are constants, which depends on the temperature  $T$  and the equilibrium concentration  $c_{eq}$  of the phases. These coefficients can be expressed as follows:

$$\begin{aligned}
A_i(T) &= \frac{1}{2} \frac{\partial \mu}{\partial c}, \\
B_i(T) &= \mu - 2A_i^2, \\
C_i(T) &= \omega_i + A_i c_{eq}^2.
\end{aligned} \tag{2.33}$$

The free energies, the first derivatives of the free energies  $-\frac{\partial f}{\partial c}$  or  $\mu$ , as well as the second derivatives of it  $-\frac{\partial^2 f}{\partial^2 c}$  or  $\frac{\partial \mu}{\partial c}$  can be obtained from the thermodynamic fitting of Eq. (2.33) at the particular temperature  $T$  using CALPHAD databases. In our present purpose, we choose the coefficients to be equal  $A_\alpha = A_\beta = A_l = A$ , which renders equal slopes for the Liquidus and Solidus lines of the computed phase diagram. Further simplification of  $A_\alpha = A_\beta = A_l = 1$  leads the  $B$  and  $C$  coefficients to become (for a binary alloy of composition  $c_E$  undergoing eutectic reaction at an undercooling  $\Delta T$  resulting solids of compositions  $c_\alpha$  and  $c_\beta$ ):

$$\begin{aligned}
B_i &= 2(c_E - c_{eq}), \\
C_i &= c_{eq}^2 - c_E^2 + \frac{2\Delta T}{m}(c_E - c_{eq}).
\end{aligned} \tag{2.34}$$

Note that, with this approach, the expressions for the capillary lengths for the  $\alpha$ - liquid and  $\beta$ - liquid interfaces can be given by:

$$d_0^i = \frac{\gamma_{iL}}{\partial^2 f_i / \partial c^2} = \frac{\gamma_{iL}}{2A}. \tag{2.35}$$

$\gamma_{iL}$  the surface free energy of  $i - L$  interfaces.

## 2.5 Incorporation of Anisotropy

Referring to Eq. (2.15), in the presence of surface tension anisotropy (say,  $m$  - fold),  $a_c$  is no longer 1. Instead, it depends on the local orientation angle of an interface:  $\theta$ , which

is measured in between the interface normal  $\hat{n}$  and the temperature gradient  $G$ . In two dimensions,  $a_c$  takes the usual polar form:

$$a_c(\theta) = 1 + \epsilon_m \cos(m\theta), \quad (2.36)$$

where  $\theta$  is the local interface orientation angle and  $\epsilon_m$  is the degree of anisotropy of the  $ij$  interface. In two dimensions, the interface orientation  $\theta$  can be simply obtained for an  $i$ - $j$  interface from the Cartesian components of the vector  $q_{ij} = \phi_i \nabla \phi_j - \phi_j \nabla \phi_i$ : we have

$$\tan \theta = \frac{q_{ij}^{(y)}}{q_{ij}^{(x)}}. \quad (2.37)$$

Some simple anisotropy functions  $a_c(\theta)$  can also be directly expressed in terms of  $q_{ij}$  instead of  $\theta$ . Using this, we can approximate the four-fold and two-fold (for example, in  $xy$  plane) anisotropy functions to their lowest order symmetries, respectively, as:

$$a_c = 1 - \epsilon_4 [3 - 4(\hat{q}_x^4 + \hat{q}_y^4)], \quad (2.38)$$

$$a_c = 1 + \epsilon_2 (\hat{q}_x^2 - \hat{q}_y^2). \quad (2.39)$$

$\hat{q}$  is the unit normal vector, and  $\hat{q}_x$  and  $\hat{q}_y$  are the Cartesian components of it, respectively.

As explained in Chapter 1, our numerical work is motivated by the rotating directional solidification experiments. Changing the angle ( $\theta_R$ ) between the crystalline axis and the pulling direction rotates the anisotropy within the growth plane (refer to Fig. 1.19). If a growing crystal is rotated by an angle of  $\theta_R$ , in two dimensions the anisotropy function is changed from  $a_c(\theta)$  to  $a_c(\theta - \theta_R)$ . We wish to use an implementation that can easily be extended to three dimensions and arbitrary rotations. In order to achieve this, we directly work with the components of the interface normal vector and transform the equations to the reference system of the crystal with the help of the appropriate rotation matrices, which are detailed in Appendix B.

Note that, in two dimensions, the Cartesian components of the normal vector  $q_{ij}$  in the laboratory frame are given by  $q_x$  and  $q_y$ . We rotate these components by an angle of

$\theta_R$ , which brings it into the reference frame of the crystal,

$$q' = \begin{bmatrix} q'_x \\ q'_y \end{bmatrix} = \mathcal{R} \begin{bmatrix} q_x \\ q_y \end{bmatrix} \quad (2.40)$$

where  $\mathcal{R}$  is a 2-D rotation matrix

$$\mathcal{R}(\theta_R) = \begin{bmatrix} \cos \theta_R & -\sin \theta_R \\ \sin \theta_R & \cos \theta_R \end{bmatrix} = \begin{bmatrix} R_{xx} & R_{xy} \\ R_{yx} & R_{yy} \end{bmatrix}. \quad (2.41)$$

In the reference frame of the crystal, the anisotropy can be expressed in the “primed” vector components, independently of the rotation angle. For example, a simple cubic anisotropy function is given by

$$a_c(q') = 1 - \epsilon_4 \left[ 3 - 4 \left( \frac{q_x'^4 + q_y'^4}{|q'|^4} \right) \right], \quad (2.42)$$

where  $\epsilon_4$  is the anisotropy strength; a two-fold anisotropy is generated by

$$a_c(q') = 1 - \epsilon_2 \left( \frac{q_x'^2 - q_y'^2}{|q'|^2} \right) \quad (2.43)$$

for an arbitrary function  $a_c(\theta)$ , we may use that  $\tan \theta = q'_y/q'_x$ . Note that, a similar approach for rotating the normal vector components with an arbitrary angle has been utilized to incorporate a misorientation between the crystal axes and the thermal gradient in order to study the directionally solidified inclined structures in thin samples [38].

In order to calculate the functional derivative in Eq. (2.20), repeated use of the chain rule is made. For instance, we have

$$\frac{\partial a_c(q')}{\partial \phi_i} = \frac{\partial a_c}{\partial q'_x} \cdot \frac{\partial q'_x}{\partial \phi_i} + \frac{\partial a_c}{\partial q'_y} \cdot \frac{\partial q'_y}{\partial \phi_i} = \begin{bmatrix} \frac{\partial a_c}{\partial q'_x} & \frac{\partial a_c}{\partial q'_y} \end{bmatrix} \mathcal{R} \begin{bmatrix} \partial_x \phi_j \\ \partial_y \phi_j \end{bmatrix}. \quad (2.44)$$

Similarly, we find

$$\begin{bmatrix} \frac{\partial a_c(q'_{ij})}{\partial(\partial_x \phi_i)} \\ \frac{\partial a_c(q'_{ij})}{\partial(\partial_y \phi_i)} \end{bmatrix} = \begin{bmatrix} \frac{\partial a_c}{\partial q'_x} R_{xx} \frac{\partial q_x}{\partial(\partial_x \phi_i)} + \frac{\partial a_c}{\partial q'_y} R_{yx} \frac{\partial q_x}{\partial(\partial_x \phi_i)} \\ \frac{\partial a_c}{\partial q'_x} R_{xy} \frac{\partial q_y}{\partial(\partial_y \phi_i)} + \frac{\partial a_c}{\partial q'_y} R_{yy} \frac{\partial q_y}{\partial(\partial_y \phi_i)} \end{bmatrix} = -\phi_\beta \begin{bmatrix} \frac{\partial a_c}{\partial q'_x} R_{xx} + \frac{\partial a_c}{\partial q'_y} R_{yx} \\ \frac{\partial a_c}{\partial q'_x} R_{xy} + \frac{\partial a_c}{\partial q'_y} R_{yy} \end{bmatrix}. \quad (2.45)$$

In 2-D,  $|q'|$  in Eqs. (2.42, 2.43) can be defined as  $\sqrt{q_x'^2 + q_y'^2}$ . This renders the  $\frac{\partial a_c}{\partial q'_i}$  components in Eqs. (2.44, 2.45) as follows, for a 4-fold (Eq. 2.42) and 2-fold (Eq. 2.43) functions, respectively:

$$\begin{pmatrix} \frac{\partial a_c}{\partial q'_x} \\ \frac{\partial a_c}{\partial q'_y} \end{pmatrix} = 16 \epsilon_4 \begin{bmatrix} \frac{q_{ij,x}^3}{|q_{ij}|^4} - \frac{q'_{ij,x} \cdot (q_{ij,x}^4 + q_{ij,y}^4)}{|q_{ij}|^6} \\ \frac{q_{ij,y}^3}{|q_{ij}|^4} - \frac{q'_{ij,y} \cdot (q_{ij,x}^4 + q_{ij,y}^4)}{|q_{ij}|^6} \end{bmatrix}, \quad (2.46)$$

$$\begin{pmatrix} \frac{\partial a_c}{\partial q'_x} \\ \frac{\partial a_c}{\partial q'_y} \end{pmatrix} = 2 \epsilon_2 \begin{bmatrix} \frac{q'_{ij,x}}{|q_{ij}|^2} - \frac{q'_{ij,x} \cdot (q_{ij,x}^2 - q_{ij,y}^2)}{|q_{ij}|^4} \\ -\frac{q'_{ij,y}}{|q_{ij}|^2} - \frac{q'_{ij,y} \cdot (q_{ij,x}^2 - q_{ij,y}^2)}{|q_{ij}|^4} \end{bmatrix}. \quad (2.47)$$

Generally speaking, in three dimensions, we have two variants of rotation in a spherical coordinate system (see figure 2.2) –  $(\theta, \varphi)$ :  $\varphi$  is the azimuthal angle and  $\theta$  is the polar angle or the angle of elevation, similar to 2-D rotations.

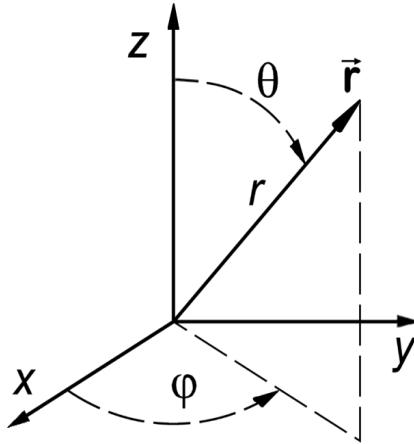


Figure 2.2: Two angles  $\varphi$  and  $\theta$  represent a spherical coordinate system.  $xy$  is the azimuthal plane. Axis  $z$  is the direction of  $\mathbf{G}$  as well as the growth direction which renders the azimuthal plane as a transverse plane of the simulation box.

In case of a rotation in the azimuthal plane in three dimensions, this is reduced to a single rotation variable, say,  $\varphi_R$  in the azimuthal plane. As a result, the corresponding



anisotropy function  $a_c(\varphi)$  becomes  $a_c(\varphi - \varphi_R)$ , and its subsequent transformation to Cartesian coordinate can be performed using a suitable rotation matrix. Such an elementary 3-D rotation matrix  $\mathcal{R}$  can be written as:

$$\mathcal{R} = \begin{bmatrix} R_{xx} & R_{xy} & R_{xz} \\ R_{yx} & R_{yy} & R_{yz} \\ R_{zx} & R_{zy} & R_{zz} \end{bmatrix} = \begin{bmatrix} \cos \varphi_R & -\sin \varphi_R & 0 \\ \sin \varphi_R & \cos \varphi_R & 0 \\ 0 & 0 & 1 \end{bmatrix} \quad (2.48)$$

Note the above rotation matrix essentially implies a 2-D rotation, in  $xy$  plane, around a fixed axis  $z$ . Similar invariant rotations can be structured, as above, by changing the axis of rotation along with possible combinations of (composite) 2-D rotations, which are detailed in Appendix B. In a similar way, explained before, these rotation matrices are incorporated in the system of equations via Eq. (2.40). If we make  $\mathcal{R}$  as the identity matrix, we recover the equations for an un-rotated coordinate frame (Eq. (2.38)). Therefore, rotation matrix representation is a generalized way to incorporate anisotropy in numerical simulations.

## 2.6 Regularized Phase-field model

As explained in Chapter 1, stability of a particular orientation is determined by the surface stiffness parameter defined by:  $a_c + \frac{d^2 a_c}{d\theta^2}$  (or,  $a_c + a_c''$ ). If the magnitude of the anisotropy strength  $\epsilon_m$  ( $m = 2, 4$ ) becomes very high to make the surface stiffness negative, then the equilibrium microstructure contains sharp corners and edges. Presence of sharp corners makes the surface normal as well as the spatial derivatives of the phase field  $\phi$  discontinuous around it leaving the phase-field equations derived beforehand ill-posed. This can be overcome by adding higher order terms in the free energy functional in Eq. (2.13) in order to penalize the curvature.

In the following, we describe two ways of regularization implementation techniques and the modified phase-field evolution equations. Egglestone et al. [74] employed a convexification of the polar plot of  $1/a_c$  to remove such ill-posedness. Wheeler [65] linearly regularized the functional adding a square of the curvature, detailed in sec. 2.6.2. Torabi et al. [75] employed the Willmore regularization technique in which square of the mean

curvature is added to the functional, detailed in sec. 2.6.1.

### 2.6.1 Willmore Regularization

In this approach, we add the following term in the functional  $\Omega$  (Eq. (2.13)).

$$\mathcal{F} = \frac{\beta}{2} \int_V \frac{1}{\epsilon^3} (w'(\phi) - \epsilon^2 \nabla^2 \phi)^2 dV \quad (2.49)$$

$\beta$  is a length scale parameter over which the equilibrium sharp corners are smoothed out.  $w(\phi)$  is the double-obstacle potential given by Eq. (2.16) and  $w'(\phi) = \frac{\partial w}{\partial \phi}$ . In the following way, the Laplacian of  $\phi$  is broken into pieces and connected to the normal vector components to obtain the modified phase-field equations,

$$\begin{aligned} \nabla^2 \phi &= \nabla \cdot \nabla \phi \\ &= \nabla \cdot \mathbf{q} \\ &= \nabla \cdot (\phi_\alpha \nabla \phi_\beta - \phi_\beta \nabla \phi_\alpha) \\ &= \phi_\alpha \nabla^2 \phi_\beta - \phi_\beta \nabla^2 \phi_\alpha \end{aligned} \quad (2.50)$$

The variational calculus of the following form is used:

$$\frac{\delta F}{\delta \phi_\alpha} = \frac{\partial F}{\partial \phi} - \nabla \cdot \frac{\partial F}{\partial (\nabla \phi)} + \nabla^2 \cdot \frac{\partial F}{\partial (\nabla^2 \phi)} \quad (2.51)$$

$$\frac{\partial F}{\partial \phi_\alpha} = -\beta \frac{1}{\epsilon} m \nabla^2 \phi_\beta \quad (2.52)$$

$$\frac{\partial F}{\partial (\nabla^2 \phi_\alpha)} = \beta \frac{1}{\epsilon} m \phi_\beta \quad (2.53)$$

$$m = w'(\phi) - \epsilon^2 (\phi_\alpha \nabla^2 \phi_\beta - \phi_\beta \nabla^2 \phi_\alpha) \quad (2.54)$$

$$w'(\phi) = \frac{16}{\pi^2} \phi_\beta \quad (2.55)$$

$$w''(\phi) = 0 \quad (2.56)$$

$$\frac{\partial F}{\partial(\nabla^2\phi_\alpha)} = \frac{\beta}{\epsilon} \left[ w'(\phi) - \epsilon^2(\phi_\alpha \nabla^2\phi_\beta - \phi_\beta \nabla^2\phi_\alpha) \right] \phi_\beta \quad (2.57)$$

$$\frac{\partial F}{\partial(\nabla^2\phi_\alpha)} = \frac{\beta}{\epsilon} \left[ \frac{16}{\pi^2} \phi_\beta^2 - \epsilon^2(\phi_\alpha \phi_\beta \nabla^2\phi_\beta - \phi_\beta^2 \nabla^2\phi_\alpha) \right] \quad (2.58)$$

$$(2.59)$$

$$\nabla \left( \frac{\partial F}{\partial(\nabla^2\phi_\alpha)} \right) = \frac{16}{\pi^2} (2\phi_\beta \nabla\phi_\beta) - \epsilon^2 \left[ \nabla\phi_\beta \phi_\alpha \nabla^2\phi_\beta + \phi_\beta \nabla\phi_\alpha \nabla^2\phi_\beta \right] \quad (2.60)$$

$$+ \phi_\beta \phi_\alpha \nabla^3\phi_\beta - 2\phi_\beta \nabla\phi_\beta \nabla^2\phi_\alpha - \phi_\beta^2 \nabla^3\phi_\alpha \quad (2.61)$$

$$\nabla^2 \frac{\partial F}{\partial(\nabla^2\phi_\alpha)} = \nabla \cdot \left( \nabla \frac{\partial F}{\partial(\nabla^2\phi_\alpha)} \right) \quad (2.62)$$

These above components update the phase-field equations following Eq. (2.22).

## 2.6.2 Linear Regularization

This approach does not depend on the potential  $w(\phi)$  like the previous case, and a simple Laplacian of phase-field ( $\phi$ ) squared serves the purpose. In this case, the additional term added to the functional  $\Omega$  is:

$$\mathcal{F} = \frac{\beta}{2} \int_V \frac{1}{\epsilon^3} (\epsilon^2 \nabla^2 \phi)^2 dV \quad (2.63)$$

Like before, a variational calculus of the following form is used to obtain the components to replace Eq. (2.22)

$$\frac{\partial F}{\partial\phi_\alpha} = \beta\epsilon(\phi_\alpha \nabla^2\phi_\beta - \phi_\beta \nabla^2\phi_\alpha) \nabla^2\phi_\beta \quad (2.64)$$

$$\frac{\partial F}{\partial(\nabla^2\phi_\alpha)} = \beta\epsilon(\phi_\alpha \nabla^2\phi_\beta - \phi_\beta \nabla^2\phi_\alpha) (-\phi_\beta) \quad (2.65)$$

$$\nabla^2 \frac{\partial F}{\partial(\nabla^2\phi_\alpha)} = -\beta\epsilon(\phi_\alpha \phi_\beta \nabla^4\phi_\beta - \phi_\beta^2 \nabla^4\phi_\alpha) \quad (2.66)$$

In this way, we obtain the regularized phase field evolution equations in order to study every possible orientations present in the system including the unstable ones.

## 2.7 Relation to sharp interface theory

Let us comment on some important features of this model with respect to the sharp interface model. First, the driving force for phase transformations from (say)  $i$  to  $j$  phase is given by the difference of grand potentials between the parent and the child phases:

$$\Delta\omega(\mu, T) = \sigma_{ij}\kappa, \quad (2.67)$$

$\sigma$  is the surface tension between phases and  $\kappa$  is the curvature of  $i-j$  interface. In the sharp interface description this is equivalent to the undercooling  $\Delta T = \Gamma\kappa$ ,  $\Gamma(= \sigma_{ij}/L)$  is the Gibbs-Thomson coefficient.

Second, the Gibbs-Thomson condition for this kind of grand potential model can be obtained using a Clausius-Clapeyron like analysis [76]:

$$\frac{\partial\mu}{\partial t} = \frac{\left(\frac{\partial\omega_i}{\partial T} - \frac{\partial\omega_j}{\partial T}\right)}{(c_i - c_j)}. \quad (2.68)$$

Using  $\frac{\partial\mu}{\partial t} = \frac{\partial\mu}{\partial c} \frac{\partial c}{\partial t}$ , we can also obtain the slopes of the phase boundary lines

$$m = 2A \frac{(c_i - c_j)}{\left(\frac{\partial\omega_i}{\partial T} - \frac{\partial\omega_j}{\partial T}\right)}. \quad (2.69)$$

The Gibbs-Thomson coefficient can similarly be derived as:

$$\Gamma_{ij} = \frac{\sigma_{ij}}{\left(\frac{\partial\omega_i}{\partial T} - \frac{\partial\omega_j}{\partial T}\right)}. \quad (2.70)$$

Finally, to achieve local equilibrium at the interface, local net kinetics of the solute atoms must vanish there. This condition has been satisfied using a thin interface analysis of a pure material solidification problem leading to a relaxation constant  $\tau$  of  $i-j$  interface:

$$\tau_{ij} = \epsilon \frac{(c_j - c_i)^2}{D \frac{\partial c_j}{\partial \mu}} \quad (0.222). \quad (2.71)$$

---

Details of this analysis as well as the evaluation of the anti-trapping current  $\vec{j}_{at}$  can be found in [64].

# Chapter 3

## Interphase Anisotropy Effects on Lamellar Eutectics

### 3.1 Introduction

It has been known for a long time that the solidification dynamics of eutectic patterns may strongly depend on the crystal orientation of the two solid phases [77]. Such crystallographic effects during eutectic growth have been neglected so far, both in theories and models, in spite of their practical importance [78, 79]. We will focus here on lamellar eutectics. In previous works [80, 81], a distinction has been made between two types of eutectic grains. A eutectic grain is defined as a region of substantially uniform crystal orientation of the two solid phases  $\alpha$  and  $\beta$ , and thus with a constant orientation relationship between the two crystals. On the one hand, in *floating* (eutectic) grains, the dynamics of the lamellar solidification front patterns is well described by the standard theory of regular eutectics. In particular, spatial inhomogeneities of the lamellar spacing are smoothed out with time by a “spacing-diffusion” process [82, 83] generically present in out-of-equilibrium pattern forming systems [84]. On the other hand, in *locked* grains, eutectic lamellae grow in a direction that is essentially aligned to a certain crystallographic plane, and are inclined (or tilted) with respect to the main growth axis  $z$  [85, 81]. The strength of this crystallographic locking effect varies between different eutectic grains. In strongly locked

grains, the spacing-diffusion process is absent [80].

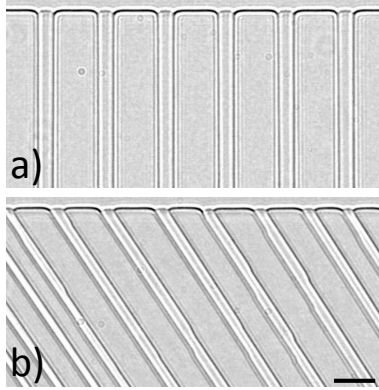


Figure 3.1: Lamellar eutectic patterns observed in situ during thin-sample directional solidification ( $V = 0.5\mu\text{m}\text{s}^{-1}$ ) of a eutectic transparent ( $\text{CBr}_4\text{-C}_2\text{Cl}_6$ ) model alloy. a) Symmetric steady-state in a “floating” eutectic grain. b) Tilted lamellae in a “locked” eutectic grain. The growth direction is vertical (liquid on top). Bar:  $20\mu\text{m}$ .

Examples of floating and locked eutectic patterns observed in thin-sample directional solidification experiments are shown in Fig. 3.1. The corresponding schematic views of the interfaces are depicted in Fig. 3.2. In the locked case, tilted lamellar microstructures are left behind in the solid by a eutectic growth front pattern that drifts laterally at a constant velocity  $V_d$  (the pattern is in a steady state in the traveling reference frame). The magnitude of the drift velocity can be large, i.e. comparable to the pulling velocity, which leads to the freezing of strongly tilted lamellae, as shown in Fig. 3.1b. In a steady-state condition, the (lamellar) tilt angle  $\theta_t$  is defined by  $\tan\theta_t = V_d/V$ . On the basis of in situ directional solidification observations using thin samples of metallic and transparent organic eutectic alloys, a conjecture was formulated recently that permits to relate the value of  $\theta_t$  to the anisotropy of the free energy of the interphase boundaries (interfacial anisotropy) [45, 41]. The main underlying hypotheses are that (i) only the S-S interfaces are anisotropic (i.e., in a nonfaceted alloy, the anisotropy of the S-L interfaces has a negligible effect on the lamellar growth dynamics), and (ii) the S-L interface keeps virtually the same shape – with mirror symmetry about the mid-plane of a lamella – as for standard (non-tilted) lamellae. The tilted pattern shown in Fig. 3.1b satisfies these conditions. In essence, under this symmetric-pattern (SP) approximation, the conjectured theory states that the Cahn-Hoffman surface tension vector  $\vec{\sigma}$  (defined in Sec. 1.4) is aligned with  $z$  (Fig.

3.2b).

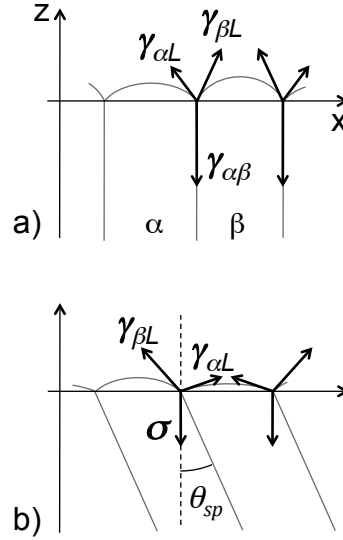


Figure 3.2: Schematic repeat units of lamellar eutectic patterns. a) Isotropic system. b) System with an interfacial anisotropy of the interphase boundary in the symmetric-pattern (SP) approximation.  $\alpha$ ,  $\beta$ : solid phases.  $L$ : liquid.  $z$ : growth direction parallel to the thermal gradient.  $x$ : direction of the isotherms.  $\theta_{sp}$ : SP-approximation lamellar tilt angle. The lateral drift velocity is given by  $\tan \theta_{sp} = V_d/V$ , with  $V$  the pulling velocity. Other symbols: see text.

The goal of the present work is to test the SP approximation by numerical simulations, in which the anisotropy of the interphase boundaries can be freely chosen. We use two different numerical models, in two dimensions. The first one is a sharp interface code, which uses the dynamic boundary-integral (BI) formalism previously developed by Karma and Sarkissian [21] (refer Sec. 3.3). This method combines an evaluation of the solute diffusion field by the boundary-integral method with an explicit front-tracking algorithm for the interface evolution. For simplicity, the S-L interfaces are assumed to be isotropic. The anisotropy of interphase boundaries is incorporated by changing the local equilibrium condition at the triple junctions from the Young to the Young-Herring law. The corresponding model equations are presented in Sec. 2.1 and a brief implementation procedure is given in Sec. 3.3. The second method is the phase-field model described in Chapter 2.

We characterize a given eutectic grain by the anisotropy function, or Wulff plot (i.e. the polar plot of the surface free energy) of the interphase boundary. It is important to note that the details of this function depend solely on the relative orientation of the



$\alpha$  and  $\beta$  crystals. In two dimensions, changing the in-plane orientation of a eutectic grain with respect to the growth axis  $z$  while keeping the relative  $\alpha\beta$  orientation fixed is equivalent to rotate the Wulff plot globally by a single angle  $\theta_R$ . Our results can be classified into two main categories, according to unstable orientations being absent or present in the Wulff shape, respectively. For all the anisotropy functions that we have tested and that do not exhibit unstable orientations, the two numerical methods give almost identical results for the tilt angle  $\theta_t$  as a function of the rotation angle  $\theta_R$ . Importantly, the value of  $\theta_t$  follows quite closely the variation of  $\theta_{sp}$  vs  $\theta_R$ , where  $\theta_{sp}$  is the tilt angle predicted by the SP-approximation. In addition, a strong locking of the lamellae onto a certain direction is well reproduced in both BI and PF simulations by using an anisotropy function with a peaked minimum. Moreover, the tilt angle is found to be largely independent of the lamellar spacing and the pulling velocity, in good agreement with the SP approximation. For anisotropies that are large enough to create orientations that exhibit a Herring instability [86], the two numerical methods give different results. In the BI simulations, a phenomenon of bistability is observed, that is, for a finite range of eutectic-grain orientations, there are *two* stable lamellar patterns with different tilt angles. Those two branches of steady-state solutions are essentially the same as the ones predicted by the SP approximation. Manifestations of a bistable behavior have indeed been observed in thin-sample solidification experiments [45]. In contrast, no such bistability is observed in the phase-field simulations.

The remainder of the chapter is structured as follows. In Sec. 3.2, we recall some facts about eutectic grains and anisotropic interfaces, present the equations of and review the SP-conjecture for the prediction of the tilt angle. In Sec. 3.4, we describe our results for various choices of the anisotropy function. In Sec. 3.5, we will discuss separately (i) a way to estimate the accuracy of measurements of the interphase boundary Wulff plot using experimental observations with the so-called rotating directional-solidification method [41], and (ii) possible reasons for the absence of hysteretic behavior in the high-anisotropy case in the PF simulations. Conclusions and perspectives are presented in Sec. 3.6.

## 3.2 Background

### 3.2.1 Anisotropic inter-phase boundaries

A lamellar-eutectic solid consists of eutectic grains made of crystals of the solid phases  $\alpha$  and  $\beta$  with uniform orientations. A (eutectic) grain hence constitutes a heterophase bicrystal. The relative orientation between the lattices of the two phases (constant within a grain) determines the interphase boundary energy and its anisotropy, which may therefore vary between grains. For a description of interphase configurations in directional solidification, we need to specify the orientation of the bicrystal and that of the interphase boundary with respect to the temperature gradient and the sample plane of the directional solidification setup. In two dimensions, two angles with respect to the temperature gradient axis are sufficient for a complete specification of these orientations.

Consider first a bicrystal in a fixed orientation with respect to the temperature gradient. Let  $\hat{n}$  be the unit normal vector of the interphase boundary, and  $\theta$  the angle between  $\hat{n}$  and the x axis (we have  $n_x = \cos\theta$  and  $n_z = \sin\theta$ ). Furthermore, let the anisotropic interphase boundary energy be given by

$$\gamma_{\alpha\beta}(\theta) = \bar{\gamma}_{\alpha\beta} a_c(\theta), \quad (3.1)$$

where  $\bar{\gamma}_{\alpha\beta}$  is a constant and  $a_c(\theta)$  is a dimensionless function.

With their help of Cahn-Hoffman  $\vec{\xi}$  and  $\vec{\sigma}$  vectors (defined in Sec. 1.4), the equilibrium shape of a  $\beta$  inclusion inside an  $\alpha$  matrix and the anisotropic equilibrium condition at trijunction points can be obtained in a simple way. As explained in Chapter 1, the Wulff plot is defined by  $\vec{r}(\theta) = \gamma_{\alpha\beta}(\theta)\hat{n}$  and the minimum-energy shape (Wulff shape) is traced by plotting the vector  $\vec{\xi}(\theta)$ . For low anisotropies that satisfy  $\gamma_{\alpha\beta}(\theta) + \gamma''_{\alpha\beta}(\theta) > 0$  for all orientations, the Wulff shape is smooth. If the interface stiffness  $\gamma_{\alpha\beta}(\theta) + \gamma''_{\alpha\beta}(\theta)$  becomes negative for a given value of  $\theta$ , a flat interface of this orientation is unstable with respect to the formation of a hill-and-valley structure (Herring instability [86]). In this case, the plot of  $\vec{\xi}$  as a function of  $\theta$  has self-intersections, and the Wulff shape is given by the inner convex part only (refer to the Fig. 1.17). The other parts, often called “ears”,

consist of three segments delimited by turning points (see for example Ref. [87] for details and illustrations). The interface stiffness is negative only on the middle segment, but all orientations located on the “ears” are missing from the physically observable convex equilibrium shape.

When the bi-crystal is rotated with respect to its reference configuration by an angle  $\theta_R$ , the interphase energy becomes

$$\gamma_{\alpha\beta}(\theta) = \bar{\gamma}_{\alpha\beta} a_c(\theta - \theta_R). \quad (3.2)$$

We choose the reference configuration ( $\theta_R = 0$ ) such that an interphase orientation of minimal energy is aligned with the growth direction. Note that positive and negative  $\theta_R$  thus correspond to rotations to the left and to the right with respect to a minimum-energy direction. Below, we will essentially test two types of anisotropy functions. The first one is of the standard form used for the modeling of crystals with  $m$ -fold symmetry, namely,

$$a_m(\theta) = 1 - \epsilon_m \cos m\theta, \quad (3.3)$$

where  $\epsilon_m$  is the  $m$ -fold anisotropy coefficient. It should be noted that for interphase boundaries, at which two centrosymmetric crystals meet, a 2-fold anisotropy is always expected (since two opposite orientation vectors describe the same surface). The second type of anisotropy function that we will study is motivated by the observation of strong locking of growth directions onto certain crystallographic planes. This usually occurs when the two solid phases exhibit an epitaxial orientation relationship [85]. In this case, the locking planes correspond to sharp cusp-like minima in the  $\gamma_{\alpha\beta}(\theta)$  function. In order to avoid the additional difficulties related to the regularization of the cusp (see for example [88]), we prefer to use a deep and narrow, but smooth minimum, which we model by a Gaussian in the anisotropy function, that is,

$$a_g(\theta) = 1 - \epsilon_g \exp\left[-(\theta/w_g)^2\right], \quad (3.4)$$

where  $\epsilon_g$  is the amplitude, and  $w_g$  is the width of the Gaussian. For both types of anisotropy, a finite range of forbidden orientations appears for large enough values of the anisotropy coefficient. In our simulations, we also used linear combinations of the functions  $a_m$  (with  $m = 2, 4$ ) and  $a_g$ ,

$$a_c(\theta) = 1 - \epsilon_g \exp\left[-(\theta/w_g)^2\right] - \epsilon_2 \cos 2\theta - \epsilon_4 \cos 4\theta \quad (3.5)$$

with various values of the parameters  $\epsilon_m$ ,  $\epsilon_g$  and  $w_g$ . This form can reproduce well typical anisotropies that have been obtained from experiments [41] and molecular dynamics simulations [89]. More details on these anisotropy functions are given in Appendix C using  $\gamma - \theta$  plots, Wulff plots and  $\vec{\xi}$ -vector plots.

Let us comment on how the sharp-interface problem introduced previously needs to be modified in order to take the interphase boundary anisotropy into account. Since we suppose that the S-L interfaces remain isotropic (which should be a good approximation for nonfaceted substances), the Gibbs-Thomson conditions, Eq. (2.5), are unchanged. In addition, since we still assume that there is no diffusion in the solid, we do not need to write a local-equilibrium condition along the interphase boundaries. Therefore, the only change that intervenes in the equations is a modification of the local-equilibrium condition at the trijunction, which becomes a Young-Herring equation, that is,

$$\gamma_{\alpha L} \hat{t}_{\alpha L} + \gamma_{\beta L} \hat{t}_{\beta L} + \vec{\sigma} = 0, \quad (3.6)$$

with  $\vec{\sigma}$  given by Eq. (1.31). Note that the  $\vec{\sigma}$  vector is not parallel to the interphase boundary (Fig. 3.3a).

### 3.2.2 Theoretical predictions for the tilt angle

The SP approximation that allows us to obtain a prediction for the growth angle is based on the experimental findings presented in Refs.[45, 41]. It was found that, even for lamellae that grow at a large angle with respect to the temperature gradient, the shape of the S-L interface is close to the one observed for well-aligned lamellae. More precisely, the “heads”

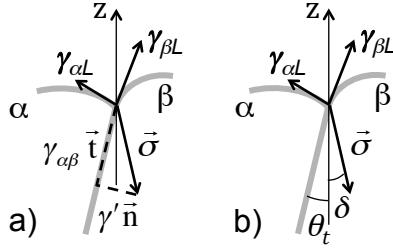


Figure 3.3: a) Illustration of the Young-Herring equilibrium condition at the trijunction.  $\vec{n}$  and  $\vec{t}$ : normal and tangent unit vectors of the interphase boundary. b) Definition of the tilt angle  $\theta_t$  and the angle  $\delta$  between  $\vec{\sigma}$  and  $z$ .

of the lamellae are approximately mirror-symmetric with respect to the mid-plane of the lamellae, which means that the contact angles of the S-L interfaces at the trijunctions are nearly the same on both sides of a lamella (to within the resolution of the experiments). Considering the Young-Herring condition of Eq. (3.6), a strictly symmetric shape is possible only if the vector  $\vec{\sigma}$  is aligned with the  $z$  axis. Using the fact that  $\hat{t}_{\alpha\beta} = (\sin\theta, -\cos\theta)$  and  $\hat{n}_{\alpha\beta} = (\cos\theta, \sin\theta)$  in the  $(x, z)$  plane, the condition that the  $x$  component of  $\vec{\sigma}$  is zero writes

$$\gamma_{\alpha\beta}(\theta - \theta_R)\sin\theta + \gamma'_{\alpha\beta}(\theta - \theta_R)\cos\theta = 0. \quad (3.7)$$

For a fixed orientation  $\theta_R$  of the eutectic grain, this is a nonlinear equation for the interface orientation  $\theta$ , which can easily be solved numerically for arbitrary anisotropy functions  $a_c(\theta)$ . As long as the interface stiffness  $\gamma_{\alpha\beta}(\theta) + \gamma''_{\alpha\beta}(\theta)$  is positive for all angles, this equation has a unique solution. For negative stiffness, there are ranges of  $\theta_R$  for which there exist three solutions, of which one corresponds to an orientation that is present on the equilibrium shape, one to an unstable orientation, and the third to a metastable orientation with positive stiffness that is missing on the equilibrium shape (belonging to an “ear”). This is the prediction against which we will compare our numerical results. As mentioned, we will note  $\theta_{sp}$  the value of  $\theta$ , solution of Eq. (3.7), which is predicted by the SP approximation.

As will be seen below, a steady state with tilted lamellae obtained from our simulations generally does not follow exactly the prediction of Eq. (3.7). The departure from the conjecture can be quantified by the value of the angle between the  $\vec{\sigma}$  vector and the  $z$

axis, which we will denote by  $\delta$  in the following, as illustrated in Fig. 3.3b. The SP approximation predicts  $\delta = 0$ .

### 3.3 Boundary-integral method

For our BI calculations, we have adapted the method developed by Karma and Sarkissian [21]. In the quasistationary approximation, valid for slow growth velocities, the solute diffusion equation, Eq. (2.3) can be replaced by the Laplace equation,  $\vec{\nabla}^2 u = 0$ . The use of Green's function techniques then permits to transform this partial differential equation together with the boundary conditions at the interface into a single integro-differential equation along the S-L front. The numerical procedure to calculate the time evolution of the growth front is as follows. The interfaces are discretized with the help of marker points that are uniformly spaced along the interface. The gradient of the concentration field  $u$ , and thus the interface velocity from Eq. (2.4), is obtained from the boundary-integral equation for each interface point except for the trijunction points. After having moved forward the interface points, the new position of the trijunction point is found by solving Eq. (1.19), with the new positions of the first point on each interface taken as input, and the position of the trijunction as unknown. This equation is solved by a relaxation scheme. More details can be found in Ref. [21].

Since, under our hypotheses, the S-L interfaces remain isotropic, the only change that is necessary to incorporate the S-S interfacial anisotropy in this model is in the calculation of the trijunction positions. We have replaced Eq. (1.19) by Eq. (3.6); in other words, we have replaced the vector  $\gamma_{\alpha\beta}\hat{t}_{\alpha\beta}$  by the vector  $\vec{\sigma}$  in the routine that calculates the new trijunction positions.

#### 3.3.1 Parameters

We have chosen as a convenient test case a model eutectic alloy with symmetric phase diagram and properties, that is,  $m_\alpha = -m_\beta$ ,  $u_\beta = -u_\alpha$ , and  $\gamma_{\alpha L} = \gamma_{\beta L}$ . In the following, we will therefore drop the phase indices of all parameters (capillary and thermal lengths)

for simplicity. We also choose the average value of the S-S interface free energy to be equal to the S-L one ( $\bar{\gamma}_{\alpha\beta} = \gamma_{\alpha L}$ ), which would yield trijunction angles of  $120^\circ$  for isotropic interfaces. We will specify the simulation parameters using dimensionless ratios, normalizing all lengths with the diffusion length

$$l_D = \frac{D}{V}. \quad (3.8)$$

We work at the eutectic composition and in the limit of slow velocities and low temperature gradients, which implies  $d_0/l_D \ll 1$ ,  $d_0/l_T \ll 1$ , and the Péclet number  $Pe = \lambda/l_D \ll 1$ , where  $\lambda$  is the lamellar spacing. It may be useful to mention that the value of the Jackson-Hunt minimum undercooling spacing  $\lambda_{JH}$  under these conditions is given by

$$\lambda_{JH} \approx 3.844\sqrt{d_0 l_D}. \quad (3.9)$$

As we shall see below, in the regime that we have investigated, the results depend very little on the detailed choice of the parameters.

## 3.4 Results

### 3.4.1 General remarks

Our standard simulation procedure is as follows: we start from a pre-existing pair of lamellae (usually taken from a previous steady-state calculation) and slightly change the rotation angle  $\theta_R$  at a predetermined time step. Immediately after the change in  $\theta_R$  (within a solidification distance of less than one lamellar spacing), the lamellae select a new tilt angle (Figs. 3.4 and 3.5). With the model Wulff plots that we have implemented, and in the range of control parameters that we have used, the calculations always converged toward a steady-state pattern. We let the system evolve for typically 3–10 lamellar spacings before we measure the steady-state tilt angle  $\theta_t$  of the interphase boundary. In BI simulations, the inclination of the interphase boundary (and those of the tangents to the S-L interfaces at the trijunctions, as well as the  $\vec{\sigma}$  vector) is automatically given as output data of the

simulation. In PF simulations,  $\theta_t$  is measured at a distance from the trijunction of several times the interface thickness, as imposed by the diffuse nature of the trijunction. It was, however, not possible, with our PF method, to extract numerically the contact angles in the moving anisotropic trijunction with a reasonable accuracy. The same is true for the angle  $\delta$  that quantifies the departure from the SP approximation.

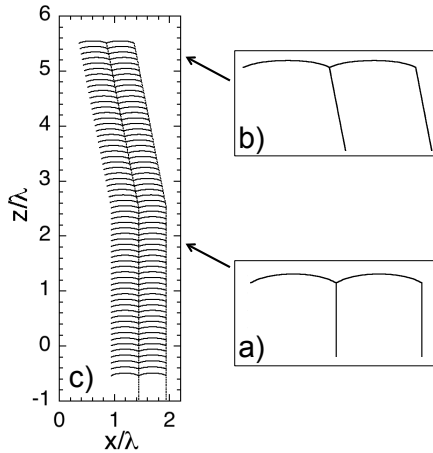


Figure 3.4: Steady-state lamellar patterns (BI simulations). a) Symmetric pattern without anisotropy. b) Tilted pattern with anisotropic interphase boundaries (anisotropy function given by Eq. (3.4);  $\epsilon_g = 0.2$  ;  $w_g = 0.1$ ;  $\theta_R = 3\pi/48 \approx 11.25^\circ$  ;  $Pe = 0.024$  ;  $\theta_t = 11.0^\circ$ ). c) Spatio-temporal diagram showing the steady-state dynamics corresponding to a) and b), successively, and the brief transient after the anisotropy was turned on.

In Figs. 3.4 and 3.5, we show illustrative examples of drifting patterns calculated with the BI and the PF codes, respectively. In both cases, we chose anisotropy functions with a peaked minimum, which can produce locked lamellar patterns for a certain  $\theta_R$  range. The relation between the shape of the anisotropy function and the tilt angles will be detailed below. For the time being, let us comment on some general features of tilted lamellar growth patterns.

First, the selection of a new steady-state tilt angle after a change of the rotation angle  $\theta_R$  occurs very rapidly (over a solidification distance of less than  $\lambda$ ), so that the interphase boundary left behind in the solid exhibits a sharp bend, see Figs. 3.4c and 3.5b. Second, in tilted patterns, the shape  $\zeta(x)$  of the S-L interfaces most often looks “flatter” than in the fully isotropic case (Fig. 3.4a,b), in agreement with experimental observations. This results from the fact that the modulus of  $\vec{\sigma}$  is smaller than the isotropic reference value



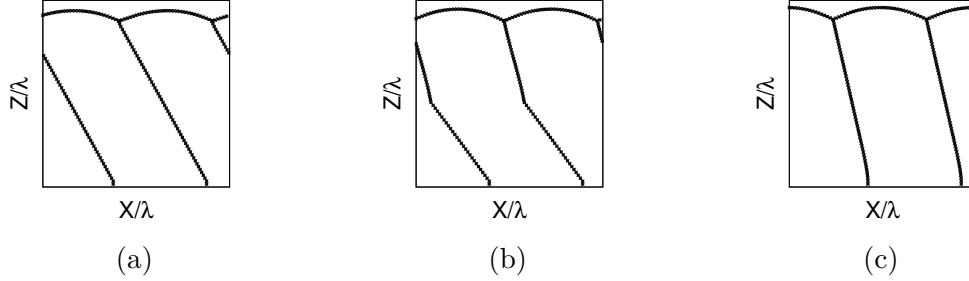


Figure 3.5: Drifting lamellar patterns in the PF model; the anisotropy function is given by Eq. (3.5) with  $\epsilon_g = 0.2$ ,  $w_g = 0.1$ ,  $\epsilon_2 = 0.0854$ , and  $\epsilon_4 = 0.0221$  (the same function as in Fig. 3.10 below): (a) “locked” tilted state ( $\theta_t = 29^\circ, \theta_R = 30^\circ$ ), (b) transition from a locked to an unlocked tilted state upon change of  $\theta_R$  from  $35^\circ$  to  $40^\circ$ , (c) unlocked tilted state ( $\theta_t = 10.8^\circ, \theta_R = 50^\circ$ ). Other parameters:  $d_0/l_D = 7.9 \times 10^{-3}$ ,  $l_T/l_D = 3.167$ .

of the surface free energy, and hence the dihedral angle between the two S-L interfaces at a trijunction is larger than in the isotropic case. Third, the S-L interfaces exhibit a certain degree of asymmetry, a quantitative measure of which can be given by the ratio  $[\zeta(x) - \zeta(-x)]/\zeta_0$ , with  $\zeta_0$  the amplitude of the S-L cap (and  $x$  being centered in the middle of a lamella). In the case of Fig. 3.4b, that quantity is of about 5%. This is equivalent to stating that (as shown by the BI simulations) the value of  $\delta$  is not zero. The sign of  $\delta$  is opposite to that of  $\theta_t$ , which indicates that the diffusion field tends to oppose the lateral drift of the lamellar pattern (as could be expected given the stability of non-tilted lamellar pattern for  $\lambda$  close to  $\lambda_{JH}$  in the absence of anisotropy).

Before studying the dynamics of tilted-lamellar solidification patterns by varying the characteristics of the  $\alpha\beta$  Wulff plot, we have tested the influence of two control parameters, namely, the lamellar spacing  $\lambda$ , and the Péclet number  $Pe$ , on the tilt angle, for a given crystallographic configuration. Figure 3.6 shows the variation of  $\theta_t$  as a function of  $\lambda/\lambda_{JH}$  for given values of the other control parameters and for a fixed Wulff plot (BI simulations). In the scanned  $\lambda/\lambda_{JH}$  range, the variations of  $\theta_t$  are very small (a fraction of a degree). Moreover, the angle  $\delta$ , which characterizes the departure from the SP approximation remains smaller than 1 degree (in absolute value). This indicates that the steady-state tilt angle  $\theta_t$  is smaller than, but close to the SP-approximation value  $\theta_{sp}$ . It

can be seen that for small lamellar spacings,  $\delta$  tends towards zero and  $\theta_t$  towards  $\theta_{sp}$  with decreasing  $\lambda$ . The Jackson-Hunt analysis predicts that for  $\lambda = \lambda_{JH}$ , the contributions of the interface curvature and the diffusion field to the front undercooling are of equal magnitude, whereas for smaller spacings capillarity dominates over the composition variations due to diffusion. Since the SP approximation takes into account only capillary phenomena, it is not surprising to see that it becomes more accurate in the small-spacing limit. It should also be mentioned that, in extended systems with isotropic interfaces, a lamellar elimination instability occurs for spacings below a threshold spacing that is lower than but close to  $\lambda_{JH}$  [83]. The value  $\lambda \approx 1.75\lambda_{JH}$  at which  $\theta_t$  passes through a minimum (and  $-\delta$  through a maximum) more or less corresponds to a change of the shape of the S-L interface, which, for the larger  $\lambda$  values, exhibits a concave part in the center of each lamella (it may also be noted that, for isotropic interfaces, the lamellar pattern undergoes an oscillatory instability for  $\lambda \approx 2.2\lambda_{JH}$  [21]).

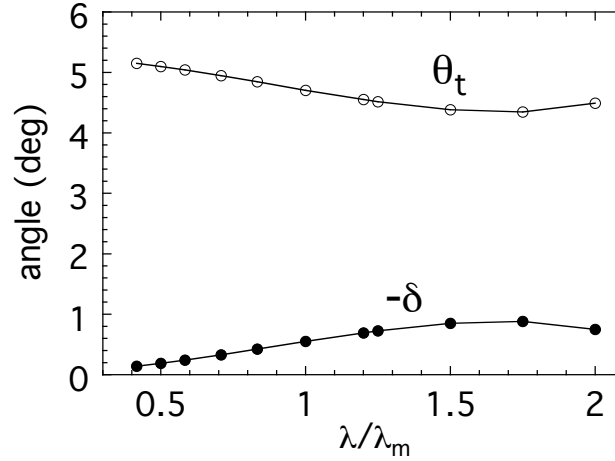


Figure 3.6: Steady-state tilt angle  $\theta_t$  obtained from BI simulations as a function of the reduced lamellar spacing  $\lambda/\lambda_{JH}$ , at constant  $G$  and  $V$  ( $d_0/l_D = 1.9531 \times 10^{-5}$ ,  $l_T/l_D = 4$ ). The angle  $-\delta$  is also plotted ( $\delta$  is the angle between  $\vec{\sigma}$  and  $z$ ). Anisotropy function  $a_c(\theta) = 1 - 0.05 \cos[2(\theta - \theta_R)]$ ;  $\theta_R = \pi/3$  ( $\theta_{sp} = 5.3^\circ$ ).

Figure 3.7 shows the variation of  $\theta_t$  with the Péclet number  $Pe$ , calculated with the PF method by varying the diffusion coefficient  $D$  in the liquid (this is equivalent to varying the velocity  $V$ ), at fixed  $\lambda$ ,  $d_0$ , and  $l_T$ . The graph shows a decreasing, essentially linear variation of  $\theta_t$  with  $Pe$ . This indicates that the effect of the diffusion field increases when

$Pe$  increases, and, again, that it is in opposition to the lateral drifting motion of the pattern. A linear fit of the data indicates that the value of  $\theta_t$  extrapolated to  $Pe = 0$  remains slightly smaller than the SP-approximation value ( $\theta_{sp} = 9.07^\circ$ ). Nevertheless, the variation of  $\theta_t$  remains very small over the (relatively large) range of scanned  $Pe$  values.

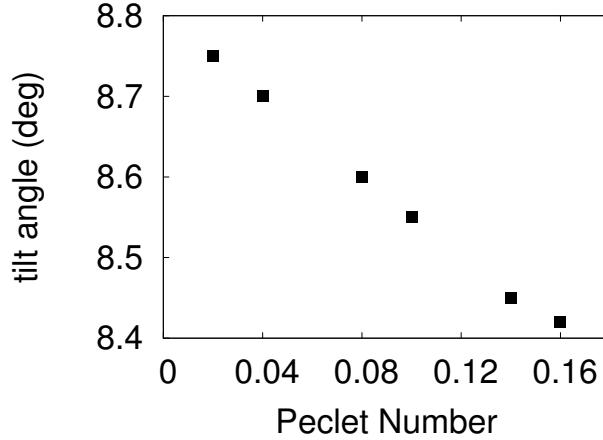


Figure 3.7: Lamellar tilt angle vs Péclet number at constant  $\lambda/d_0 = 20.25$ ,  $d_0/l_T = 2.496 \times 10^{-3}$ ;  $a_c = 1 + 0.04 \cos[4(\theta - \theta_R)]$ ,  $\theta_R = 15^\circ$  ( $\theta_{sp} = 9.07^\circ$ ).

In conclusion, the anisotropy-driven lamellar tilt angle is very little sensitive to the exact values of  $\lambda$  and  $Pe$  provided that  $\lambda$  is close to  $\lambda_{JH}$  and  $Pe \ll 1$ . Therefore, simulations performed at a fixed  $\lambda$  value close to  $\lambda_{JH}$ , and  $Pe$  significantly less than unity are fully representative of the behavior of the system over a large, experimentally relevant range of the main control parameters. In the following, the BI simulations were performed with  $Pe = 0.024$ ,  $d_0/l_D = 1.9531 \times 10^{-5}$ ,  $l_T/l_D = 4$ , and the PF simulations with  $Pe = 0.16$ ,  $d_0/l_D = 7.9 \times 10^{-3}$ ,  $l_T/l_D = 3.167$ . In both cases,  $\gamma_{\alpha L} = \gamma_{\beta L} = \bar{\gamma}_{\alpha\beta} = 1$ .

### 3.4.2 Anisotropy functions without missing orientations

Figure 3.8 shows the variation of  $\theta_t$  as a function of the rotation angle  $\theta_R$ , calculated by both BI and PF, for a simple two-fold anisotropy ( $m = 2$ ) given by Eq. (3.3). Temperature gradient, growth velocity, and lamellar spacing were held constant. The results of both simulation methods follow quite closely the SP approximation, up to differences that do not exceed a degree. As expected, we find symmetric, non-tilted patterns when either

the minimum or the maximum of  $\gamma$  is aligned with  $z$ . Somewhere in between these orientations, the value of  $\theta_t$  passes thus through a maximum for an orientation that depends on the anisotropy function. We checked that this maximum increases when the anisotropy coefficient is increased. Overall, however, the tilt angle remains much smaller than  $\theta_R$  over a full rotation range. In other words, a weak crystallographic anisotropy, though it has a clearly detectable effect on the dynamics of lamellar eutectic patterns, is not sufficient to induce a significant locking ( $\theta_t \approx \theta_R$ ). For convenience, we will call “unlocked patterns” such weakly anisotropic tilted lamellar patterns. Let us mention again that the values of  $d_0/l_D$ ,  $l_T/l_D$  and  $Pe$  are actually different for BI and PF ; the results thus demonstrate once more that the influence of all of these parameters is weak in realistic conditions.

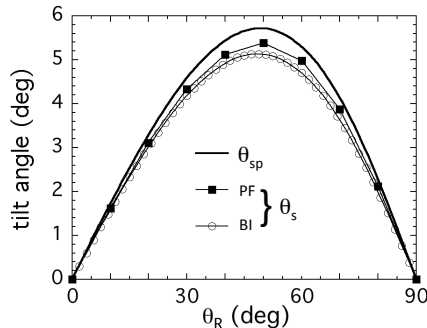


Figure 3.8: Lamellar tilt angle as a function of the rotation angle  $\theta_R$ . Weak, two-fold symmetry anisotropy of the interphase boundary ( $a_c = 1 - 0.05 \cos[2(\theta - \theta_R)]$ ). The SP-approximation angle  $\theta_{sp}$ , and the steady-state angle  $\theta_t$  obtained with the BI and PF simulations are both shown. In this graph, as well as in the following, the represented  $\theta_R$  range is limited to  $[0, \pi/2]$  for obvious symmetry reasons.

Next, we have investigated a situation in which a mild lamellar locking takes place. We use an anisotropy function according to Eq. (3.5), with  $\epsilon_g = 0.05$ ,  $w_g = 0.195$ ,  $\epsilon_2 = 0.0854$ ,  $\epsilon_4 = 0.0221$  (Fig. 3.9). This function was chosen so as to smoothly reproduce the Wulff plot extracted (assuming the SP approximation) from the experimental data of Figure 7 of Ref. [41] (see discussion below). The corresponding Wulff shape is an oval with markedly flattened sides (but without straight facets, and without forbidden orientations). The variation of  $\theta_{sp}$  with  $\theta_R$  is continuous and univalued. The simulation results for  $\theta_t$  nicely follow the SP-approximation curve.

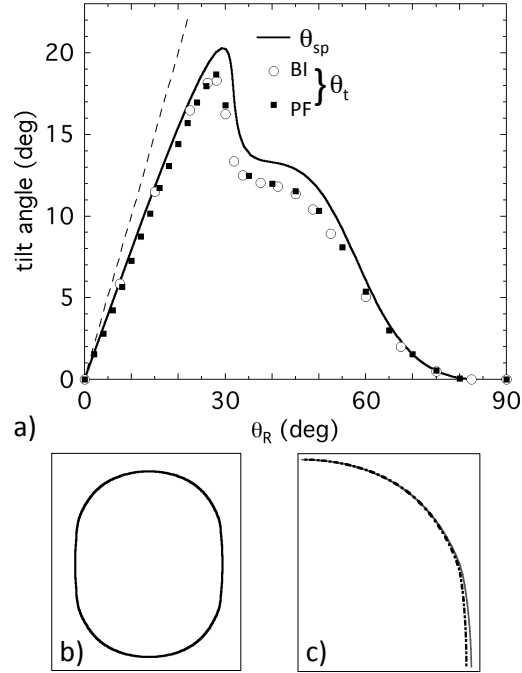


Figure 3.9: a) Lamellar tilt angle as a function of the rotation angle  $\theta_R$ . Mild lamellar locking effect caused by a shallow, smooth local minimum in the Wulff plot of the interphase boundary (see text). Same symbols as in Fig. 3.8. Dashed line: slope 1. b) Wulff shape ( $\theta_R = 0$ ). c) Partial view of the Wulff shape (dash-dotted line) and the shape reconstructed from the  $\theta_t$  data of Fig. 3.9 under the SP approximation (thin line).

Let us analyze the graph in Fig. 3.9 in more details. The variation of  $\theta_t$  is essentially linear for  $\theta_R$  ranging from 0 to about 20 degrees (we recall that for  $\theta_R = 0$ , the interphase boundary plane of minimum energy is aligned with the temperature gradient). However, the slope is substantially less than 1 [a linear best fit yields a slope of about 0.76 for  $\theta_{sp}$ , 0.73 for  $\theta_t(\text{BI})$  and 0.72 for  $\theta_t(\text{PF})$ ]. In other words, in this regime, the inclination angle of the interphase boundary remains close to, but departs by a measurable amount from the minimum-energy plane, which defines a mild locking effect. For rotation angles larger than, say, 45 degrees in Fig. 3.9, the lamellar growth dynamics escapes the influence of the Gaussian minimum of the Wulff plot. In this unlocked-pattern region, the value of  $\theta_t$  is solely determined by the  $\cos 2\theta$  and  $\cos 4\theta$  terms in the  $a_c$  function (in this  $\theta_R$  range, we checked that  $\theta_t$  remains equal to 0, as it should, when  $\epsilon_2$  and  $\epsilon_4$  are set to 0). In an intermediate  $\theta_R$  interval, there is a steep, but smooth transition between a

nearly-locked and an unlocked behavior. In this crossover range, the departure of  $\theta_t$  from the SP approximation is larger than in the rest of the graph. The value of the angle  $\delta$  as it is given by BI simulations more or less follows the same variation as  $\theta_t$  as a function of  $\theta_R$  (not shown). It reaches a maximum (of about  $2^\circ$ ) in the crossover region, but this maximum remains small as compared to the corresponding  $\theta_t$  value ( $\approx 18^\circ$ ).

### 3.4.3 Anisotropy with missing orientations

A strong lamellar-locking effect (Fig. 3.10a) can be reproduced by using an anisotropy function of the same form as that of Fig. 3.9, but with a deeper and sharper Gaussian ( $\epsilon_g = 0.2$  and  $w_g = 0.1$ ; see Eq. 3.4). This modification of the Wulff plot entails the appearance of two (quasi) facets, and four "ears" with long metastable branches and sharp-edge junctions in the Wulff shape of the interphase boundary (see inset in Fig. 3.10a). Let  $\theta_u$  and  $\theta_l$ , where  $\theta_u < \theta_l$ , be the tilt angle values at which  $\gamma + \gamma'' = 0$  on the interval  $[0, \pi/2]$  ( $\theta_u \approx 25^\circ$  and  $\theta_l \approx 70^\circ$  in the example shown in Fig. 3.10). The SP approximation predicts three distinct parts in the  $\theta_{sp}$  vs  $\theta_R$  curve: (i) an essentially linear strongly locked branch with a slope close to 1, which runs from  $\theta_R = 0$  to  $\theta_R = \theta_l$ ; (ii) an unlocked, although (weakly) anisotropic, branch for  $\theta_R$  ranging from  $\theta_u$  to  $\pi/2$ ; (iii) an intermediate branch, which connects the end points of the locked and unlocked branches, and is, presumably, not observable given that the interface boundary is unstable ( $\gamma + \gamma'' < 0$ ) along its entire length. In the  $[\theta_u, \theta_l]$  interval, two (locked and unlocked) values of the lamellar tilt angle are possible for a given eutectic-grain orientation. In this bistable range, there is a value  $\theta_e$  of the rotation angle (here, approximately  $45.3^\circ$ ) at which  $\sigma$  has the same value for both branches – this corresponds to a sharp edge in the convex equilibrium shape.

Both BI and PF simulations reproduce the two separate locked and unlocked branches (Fig. 3.10a). They demonstrate, in particular, the existence of a strong locking effect over a large orientation range, as predicted by the SP approximation. The two methods exhibit, however, a somewhat different behavior in the bistable interval. In the BI simulations, starting from the situation where the facet is aligned with the temperature gradient

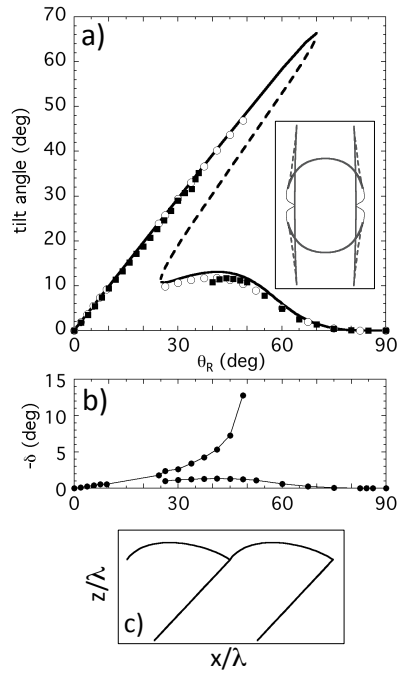


Figure 3.10: a) Lamellar tilt angle as a function of the rotation angle  $\theta_R$ . Strong lamellar locking effect with a sharp local minimum in the Wulff plot (see text). Same symbols as in Fig. 3.8. Inset: Wulff plot (thin line) and Wulff shape (thick line). Dashed lines: unstable branches. b) Angle  $\delta$  of  $\vec{\sigma}$  with  $z$  as a function of  $\theta_R$  (BI simulations). c) Shape of the lamellar pattern with the largest  $\theta_t$  value ( $\approx 48^\circ$ ) simulated with the BI code.

( $\theta_R = 0$ ), the system closely follows the locked branch upon increasing  $\theta_R$ , up to a limit angle at which it jumps abruptly to the unlocked branch. The jump occurs well before the turning point  $\theta_l$ , at a value of  $\theta_R$  which is close to  $45^\circ$ . This point can be only attained if  $\theta_R$  is successively increased along the locked branch, and the maximum value of  $\theta_t$  depends on the step size in  $\theta_R$ . It is thus clearly initial-condition dependent and has no obvious connection with the sharp-edge angle  $\theta_e$ . This limit value of  $\theta_t$  in the simulations is also compatible with previous in situ observations of tilted lamellar patterns. Reversely, when  $\theta_R$  is decreased stepwise starting from  $\theta_R = \pi/2$ , the system describes the whole unlocked branch, within numerical accuracy. This hysteresis is expected for a bistable system. It should be noted that the approach of the limit tilt angle along the locked branch also corresponds to a steep, apparently diverging increase of the  $\delta$  angle (Fig. 3.10b). This indicates that, at large tilt angles, the SP approximation, while it still correctly predicts the values of the tilt angle, becomes inaccurate with regards to other aspects of the dynamics. For instance, in contradiction with its basic assumption, the shape of the S-L interface becomes markedly asymmetric at large tilt angles, as can be seen in Fig. 3.10c.

In contrast with the BI simulations, no hysteresis is observed in the PF simulations. More precisely, no states on the locked branch have been observed for rotation angles larger than about  $35^\circ$ : when  $\theta_R$  is increased beyond that value, the lamellae switch to the unlocked state. The opposite jump from the unlocked to the locked state was found to occur at the same value of  $\theta_R$  (with an uncertainty of about  $1^\circ$ ) in runs that were started on the unlocked branch and in which the rotation angle was successively decreased. A refinement of the grid and a decrease in the interface thickness by a factor of two produced a change in this critical value that did not exceed two to three degrees. In contrast, an increase of the amplitude  $\epsilon_g$  of the Gaussian in the anisotropy function led to a marked increase of the discontinuous-jump angle.



## 3.5 Discussion

### 3.5.1 Reconstructing the anisotropy function

A practical aim of the present study was to give a numerical support to a recent experimental work based on a *rotating directional solidification* (RDS) method [45, 41]. A brief overview of the method is given in Sec. 1.5. This method uses a standard thin-sample directional solidification setup, and permits, in addition, to rotate the sample at constant angular speed about an axis perpendicular to the (two-dimensional) sample. Under a few, not very restrictive, conditions (zero translation speed, center of rotation placed on the eutectic isotherm, quasi-two-dimensional and quasistatic nature of the front pattern dynamics), this is equivalent to continuously varying the rotation angle  $\theta_R$  of a given eutectic grain with respect to the thermal gradient axis, as we have done in the above calculations. More precisely, the lamellar tilt angle  $\theta_{rds}$  observed over time during a correctly set-up RDS experiment is equal to the steady-state tilt angle  $\theta_t$  at the current value of  $\theta_R$ . Moreover, in the SP approximation, this entails that the RDS trajectories of the trijunction points are centrosymmetric closed curves homothetic to the section of the Wulff shape of the interphase boundaries by the sample plane, from which a two-dimensional anisotropy function of the interphase interface can be derived (see Ref. [45]). The anisotropy function used in Fig. 3.9 was derived from the RDS pattern of a nearly locked grain by this method. As a test for the accuracy of this method, we have reconstructed the Wulff shape from the *calculated*  $\theta_t(\theta_R)$  points under the SP assumption. The two shapes are identical to within experimental error (a few percents of the position vector), as can be seen in Inset 2 of Fig. 3.9. In conclusion, the errors due to the SP approximation are generally not larger than the experimental uncertainties, which validates the use of the SP approximation in the exploitation of the RDS patterns.

### 3.5.2 Bistability in the numerical simulations

The most important difference between the results of BI and PF simulations is the absence of bistability in the  $\theta_t(\theta_R)$  curves obtained with the PF code. As discussed previously, such

a bistable behavior should follow from the existence of states of positive stiffness on the “ears” of the Wulff plot. In addition, there is clear evidence of bistability in experimentally observed RDS patterns of strongly locked grains, as illustrated in Figure 3.11 (also see Ref. [41]). Therefore, the BI method seems to be in better agreement both with the SP theory and with experiments.

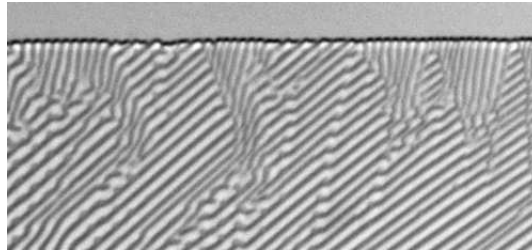


Figure 3.11: Experimental observation of a coexistence of eutectic-growth domains with two different tilt angles in a single eutectic grain. Rotating directional solidification of a thin (10- $\mu\text{m}$  thick) sample of a eutectic  $\text{CBr}_4\text{-C}_2\text{Cl}_6$  alloy. Horizontal dimension: 450  $\mu\text{m}$ .

Whereas quantitative differences between phase-field and sharp-interface models have often been reported, such a strong qualitative difference between the two methods is a striking finding. Let us first discuss – and, actually, rule out – one possible source for this difference. It is well known that PF models need to be *regularized* for anisotropy functions that generate missing orientations. Indeed, for orientations with negative stiffness, the evolution equations for the phase fields become ill-posed. This corresponds, in the free-boundary problem, to unstable growth modes with arbitrarily high growth rates in the limit of vanishing wavelengths (absence of stabilization by capillarity). This behavior can be regularized by a convexification of the polar plot of  $1/\gamma$  [74], or by the addition of higher-order derivatives in the free-energy functional [65, 75]. Since the former method requires a re-calculation of the convexification for each new choice of anisotropy function, we have preferred to use the latter by following Torabi *et al.* [75], who have added to the free energy the square of the mean interface curvature. The details of this procedure is given in Sec. 2.6.2.

As expected, with the help of this regularization, we have obtained the correct equilibrium shape for a  $\beta$  inclusion inside an  $\alpha$  matrix, even for anisotropy functions with missing orientations such as the example used for generating Fig. 3.10. However, this modification

did not appreciably alter the results for lamellar growth: still no bistable behavior was observed in the PF model, and the value of the angle at which the “jump” from the locked to the unlocked branch occurs was not appreciably modified.

We believe that the origin of the difference between BI and PF results is the behavior of the diffuse trijunctions in the PF model. Indeed, in Ref. [73], it was found by direct comparison between PF and BI simulations that the dynamics of diffuse trijunctions deviates from the predictions of sharp-interface models: since the solute diffusivity remains non-zero within the diffuse interfaces, the S-S interface can actually *move* close to the trijunction point, contrary to the assumptions made in the one-sided model of solidification, in which the diffusivity becomes zero immediately behind the (sharp) interface. Moreover, a rotation of the trijunction point by a finite angle was observed that persisted even in the sharp-interface limit [73]. Since such effects are present even for isotropic interfaces, one may expect them to be even more important here, where the anisotropic surface energy creates strong “Herring torques”. Indeed, we have observed in our simulations that the S-S interface tends to slightly change its orientation upon approaching the trijunction region. Therefore, it is possible that the PF model explores a wider range of orientations within the trijunction region than the BI model, which could facilitate the switching between different solution branches.

It should also be noted that the regularization outlined in Sec. 2.6.2 was developed and validated only for simple interfaces between two phases, and may therefore not be complete in the vicinity of trijunction points. It is possible that the bistable behavior observed in the BI simulations could be recovered by a PF model with correctly regularized trijunction points. However, since the analytic understanding of trijunction points currently is very limited, it is not clear how such a regularization should be carried out. For all these reasons, a more detailed study of moving diffuse trijunctions certainly is an interesting subject for future work.

## 3.6 Conclusions and perspectives

We have investigated lamellar eutectic growth with anisotropic S-S interphase boundaries, using two different numerical methods: a dynamic boundary-integral and a phase-field code. We have obtained good agreement between our numerical results and the prediction of a recent approximate theory for the growth direction as a function of anisotropy and orientation of the growing bicrystal, which uses the symmetric pattern approximation. For smooth anisotropy functions (no missing orientations), the two methods are in excellent agreement. If the anisotropy is strong enough to induce missing orientations around a deep minimum in the  $\gamma$  plot, BI exhibits a bistable regime that is in agreement with theoretical predictions and experimental observation, but is not found in the PF model.

The numerical simulations demonstrate that the real growth shapes are not exactly symmetric, but that this departure from the hypothesis that underlies the SP theory leads only to small differences in the steady-state tilt angle, for various choices of anisotropy functions. Moreover, these differences are virtually independent of the growth velocity and local spacing, at least in the regime of slow growth (small Peclet numbers) and for spacings close to the minimum-undercooling spacing. Since these conditions are found in many experiments, these results firmly establish the SP theory as a useful tool for predicting the growth angles of lamellar eutectics. In particular, experiments with the rotating directional solidification setup can be used to obtain *quantitative* information on anisotropy functions, as discussed in Sec. 3.5. It should be noted that in the present numerical study we have limited ourselves to a symmetric phase diagram and to growth at the eutectic composition; however, since the tilt angle is mainly fixed by the (anisotropic) capillary effects, we do not expect major differences for other phase diagrams or compositions.

The important qualitative difference between the predictions of BI and PF simulations is an interesting finding in itself, since correctly designed PF models are usually a faithful representation of the corresponding free-boundary problems. While we have not succeeded in pinpointing the exact origin of the difference between PF and sharp-interface models, we believe that the key point is the dynamic behavior of diffuse anisotropic triple junctions. This is an interesting subject for further studies.

---

Despite this open problem, in the regime of low anisotropy (without missing orientations), BI and PF simulations show an excellent agreement. This implies that these models can be used to explore the behavior of anisotropic eutectics beyond steady-state growth. In particular, it would be interesting to address the effect of anisotropy on the various instabilities that are known to occur in lamellar eutectics: short-wavelength oscillations [21, 22], spacing diffusion [82, 83], and the zig-zag instability [90, 91]. Without any doubt, the stability boundaries will depend on the strength of the anisotropy, but it seems difficult to predict in which way without the help of numerical simulations. Finally, it is straightforward to implement anisotropic PF models in three dimensions, which opens the possibility to explore numerically the anisotropy effects on eutectic growth in bulk samples, as will be described in the next chapter.

# Chapter 4

## Interphase Anisotropy Effects on Bulk Lamellar Eutectics

### 4.1 Introduction

Despite decades of research, the growth of lamellar eutectics in bulk samples is still ill-understood. Experiments as well as simulations have been performed to address the following subjects in regard to the lamellar eutectics: spacing ( $\lambda$ ) selection in the stationary patterns [91]; formation of eutectic maze structures [92]; transition of lamellar pattern into rods [92]; role of transverse temperature gradients [93]. However, to our knowledge, the role of crystalline anisotropy on the bulk lamellar eutectics has never been addressed before.

It is as of yet unknown by which mechanism the preferred orientations develop during the freezing of metals and alloys [94]. In the context of directional casting, a large numbers of randomly orientated grains in the chill zone grow into fewer orientations. These orientations continue to grow in the melt at the expense of other less favourable orientations, resulting into a columnar structure of favourably oriented grains. Similarly, in the context of directional eutectic solidification, development of such preferred orientations leads to periodic lamellar arrays along an unified direction. In the present work, we investigate the role of anisotropy in the development of such preferred orientations in

bulk lamellar eutectics. In addition, we apply this force in a view to elucidating new microstructural features, involving: (a) an irregular maze of lamellae or labyrinth, which may order fully or partially in presence of anisotropy; (b) an ideal lamellar array, which tends not to form in bulk eutectic microstructures for isotropic surface energies and (c) a preferred orientation, which is set by competing eutectic grains with anisotropic and isotropic interphases in which the anisotropic eutectic grain completely overwhelms the isotropic eutectic grain. Interestingly, this bears a significant perspective through which one can think of an intricate maze of lamellae transforms into regular lamellar arrays. In this work, we shed some light on such a mechanism to transform these mazes into regular lamellar arrays in a bulk composite. Moreover, during materials processing, many dislocations or fault lines get activated which can instigate a two-fold mechanism in the operating plane of the eutectic microstructures, leading to a ordered structure [95]. Even though the mechanism is quite simple, its importance in the formation of a regular lamellar arrays has never been appreciated before.

The structure of this chapter is as follows. First, we outline the procedural details of the simulations including parameter estimations in Sec. 4.2. In Sec. 4.3, we present the results and discuss the possible mechanisms of the microstructural features. Finally, we conclude in Sec. 4.4 with a possible outlook.

## 4.2 Simulation Details

### 4.2.1 Parameters

We consider a generic binary eutectic alloy of symmetric phase diagram with  $m_\alpha = -m_\beta$ ,  $u_\beta = -u_\alpha$ , and  $\gamma_{\alpha L} = \gamma_{\beta L} = \bar{\gamma}_{\alpha\beta}$ . Three major length scales, namely  $d_0$ ,  $l_D$  and  $l_T$ , dominate the pattern dynamics. While  $d_0$  is an intrinsic materials parameter,  $l_D$  and  $l_T$  are related to the directional solidification parameters. As we deal with a symmetric alloy, both solid phases present in the system must possess the same values of these lengths; henceforth, we drop all the indices for the sake of clarity.

As the pattern evolves with time, the length scale coming out of resultant dynamics

scales as  $\lambda \sim \sqrt{d_0 l_D} f(l_D/l_T)$  [96]. We work at the eutectic composition and the limit of low velocities and thermal gradients. In this limit, the evolving (micro-)structure seems to select a characteristic spacing [14], which scales as

$$\lambda_{JH} \sim V^{-0.5}. \quad (4.1)$$

Hence, the lateral size of the simulation box is taken as  $\sim 5\lambda_{JH}$ , which should be sufficient to capture a faithful picture of the pattern formation process. Interestingly, all of the above scaling laws can be described by the dimensionless Péclet number,  $Pe$ , defined as  $\lambda/l_D$ . In numerical simulations, we use experimentally similar values of  $d_0/l_D \approx 1.6 \times 10^{-4}$ ,  $l_T/l_D \approx 6$  and  $d_0/\lambda_{JH} \approx 1.5 \times 10^{-2}$ , which are well within  $pe \ll 1$  limit. We express the time scale  $\tilde{t}$  in the units of  $D/V^2$ .

Surface tension anisotropy of the individual interfaces are directly incorporated in our multi-phase-field model, as described in Chapter 2. We use different anisotropy functions (refer Appendix C) with suitable degrees of anisotropy ( $\epsilon_m$ ) conforming to the limit of positive surface stiffness  $\gamma + \gamma''$ , beyond of which phase-field equations become ill-posed [75]. This strictly sets the upper limit of  $\epsilon_m$  which can be used in the simulations: 1/15 for 4-fold and 1/3 for 2-fold. We vary  $\epsilon_m$  in our simulations to study its effects on the evolving patterns ranging from a strongly anisotropic to a weakly anisotropic one. Moreover, we primarily focus on the anisotropy of the  $\alpha\beta$  inter-phase boundary on pattern formation, as this is supposed to be the major force according to symmetric pattern approximation [41]. Effect of S-L interfacial anisotropy is considered negligible and, hence, not included in the scope of the present work.

### 4.2.2 Procedures

We start with a “random pattern”: an almost equal volume fractions of  $4\Delta x \times 4\Delta y \times h$  boxes of  $\alpha$  and  $\beta$  phases are randomly distributed throughout the simulation domain.  $h$  is the perpendicular distance from the bottom of the simulation domain to the initial solid front and  $\Delta x$  and  $\Delta y$  are the grid spacings in x- and y-directions, respectively. The



edges of the solid boxes are taken as four times the grid spacing to keep the boxes stable and make them grow in subsequent microstructural evolution. As the solid advances a particular distance in the liquid, we pull out a pre-defined length of solid from the bottom of the box, because there is no diffusion in the solid. Further, such pullback keeps the front stationary ( $z = 0$ ) in the laboratory frame; thus, we save a considerable amount of computation time and storage.

In x- and y-directions we use either periodic or Neumann boundary conditions. In particular, Neumann boundary condition mimics the directional solidification experiments in which the sample is confined between two glass plates where the flux of the solute vanishes. In our simulations, for most of the cases, we put this boundary condition along, at least, one of the directions to make the boundaries act like a wall and the evolving solids meet at the boundaries at normal angle. This way, effects of geometrical factors are minimised during the pattern formation process.

All simulations are carried out in a rectangular box discretized into  $160 \times 160 \times 80$  grid cells with  $\epsilon/\Delta x = \epsilon/\Delta y = \epsilon/\Delta z = 0.75$ . Besides, we set a numerically interface thickness value of  $\epsilon/d_0 = 1.6$ , well within the limit in which results become almost independent of interface thickness.

## 4.3 Results

### 4.3.1 Lamellar tilt

We begin with 3-D extensions of our previous work (Chapter 3): anisotropy of the  $\alpha\beta$  interphase boundary determines the orientation of the lamellar eutectics in 2-D. If we include an in plane polar rotation of  $\theta_R$  to the crystalline axis of the growing solid with respect to the temperature gradient, the interphase tilts at a steady state tilt angle of  $\theta$  to maintain the local interphase equilibrium at the trijunction (refer Eq. (3.7))

$$\gamma_{\alpha\beta}(\theta - \theta_R) \sin \theta + \gamma'_{\alpha\beta}(\theta - \theta_R) \cos \theta = 0 \quad (4.2)$$

This is the essence of symmetric pattern approximation [45]. We simulate the growth of a pair of lamella of spacing  $\lambda_{JH}$ , as in Fig. 4.1a, with a smooth anisotropy function in rotating coordinate frame, where the rotation  $\theta_R$  can be applied in the  $xz$ - plane or the  $yz$ - plane (refer figure 2.2), parallel to the imposed thermal gradient. We found the tilt of the lamellae (Fig. 4.1b) is consistent with the approximation given by Eq. (4.2). Moreover, the tilt angle, the lamellae make with the growth axis for different rotations, closely follow the solution of this approximation (Fig. 4.2). This, indeed, cements our confidence that the approximation, which relies only on the interphase boundary anisotropy, works in 2-D as well as in 3-D.

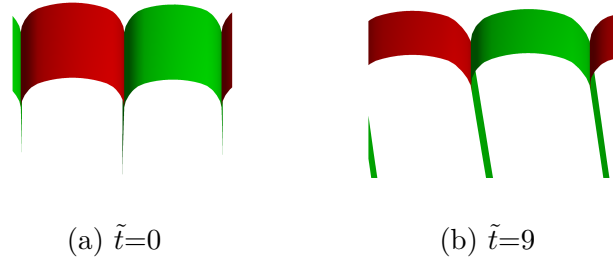


Figure 4.1: A period of lamellae: (a) untilted and (b) tilted state. Colors of  $\alpha$  and  $\beta$  are red and green, respectively.

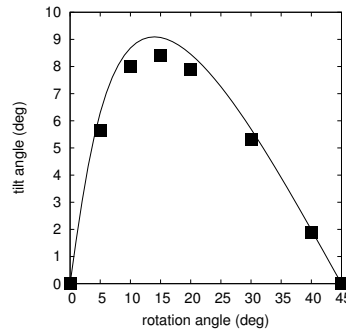


Figure 4.2: Simulated  $\theta_t$  excellently follows the theoretically predicted value for an anisotropy function  $a_c = 1 + 0.04 \cos[4(\theta - \theta_R)]$ .

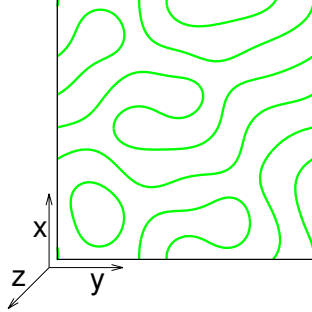


Figure 4.3:  $\alpha\beta$  interfaces in the transverse plane ( $xy$ ) of the solid which is growing in the  $z$  direction. The interfaces are contoured at  $\phi_\alpha = \phi_\beta = 0.5$ .

### 4.3.2 Structural selection in single eutectic grain

Eutectic solidification produces a rich variety of microstructures in three dimensions. We show some exemplary structures for different anisotropy functions and, subsequently, explain the dynamics for these kind of structural evolution. Moreover, to quantify these microstructures, we calculate the local orientation angles of the S-S interfaces of a particular 2-D plane, as in Fig. 4.3, which contains the anisotropy, transverse to the growth direction. At any interface point, the local interface orientation angle can be defined as:  $\Theta = \tan^{-1}(\hat{n}_y/\hat{n}_x)$ ,  $\hat{n}_y$  and  $\hat{n}_x$  are the orthogonal components of a unit normal vector  $\hat{n}$  defined by  $\frac{\nabla\phi_i}{|\nabla\phi_i|}$  in which  $\phi_i$  signifies the local phase field parameter of the solid  $i$ .

At first, for the sake of completeness, we will describe the pattern formation in the absence of anisotropy when  $\bar{\gamma}_{\alpha\beta} = \gamma_{\alpha L} = \gamma_{\beta L}$ . We begin with a “random pattern” of equal volume fractions of  $\alpha$  and  $\beta$ , as in Fig. 4.4a, and impose periodic boundary conditions along  $x$ - and  $y$ - directions. After some time, a complex network of lamellae forms, shown in Fig. 4.4b. We can see that such labyrinthine structure is locally ordered in many areas, but globally there is no order at all. This is further clarified with the help of a histogram of local interface orientation angles in Fig. 4.4c. Moreover, initial phase evolution of such systems is found to be very fast and towards the end it slows down so much that it seems the system never reaches an ordered state. In the intermediate stages, the pattern consists

of many fragments of “broken” lamellae, which must reconnect to form a regular system. However, such reconnection is hindered for an isotropic system, and we obtain a random lamellar pattern. Experiments on isotropic organic lamellar eutectic alloy of  $\text{CBr}_4 - \text{C}_2\text{Cl}_6$  have also confirmed the existence of such random lamellar maze patterns which persist over the entire duration of the experiments [93, 97].

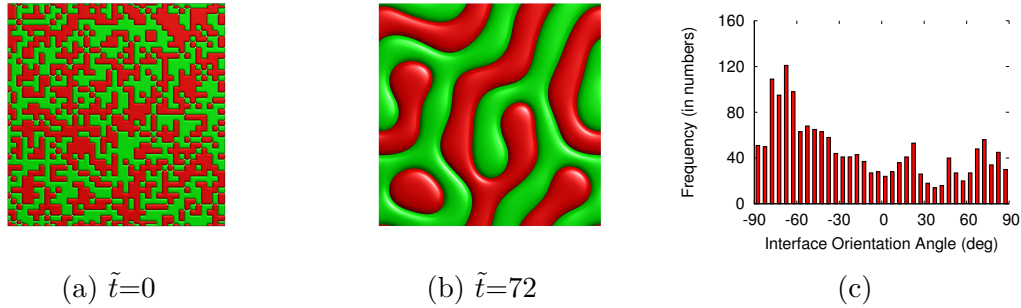


Figure 4.4: A random pattern isotropically evolves to a random lamellar pattern; colors of  $\alpha_1$  and  $\beta_1$  are red and green, respectively. Fig. 4.4c confirms the random spread in interface orientation angles in a labyrinth.

In contrast to the isotropic case, if we impart a certain degree of anisotropy to the system, an ordering is induced in the resultant microstructures. In Figs. 4.5 we show few exemplary four-fold anisotropic morphologies and it indeed exhibit certain arrangements of the  $\alpha\beta$  solids. In Fig. 4.5a, a lamella-like morphology is seen along with a zigzag type of interfaces with sharp bends or corners which are attributed to high degrees of anisotropy. These zigzag lamellae can not become fully ordered because of the faults present in the system (see the green lamella ends) rendering the phases unable to reconnect. For a smaller degree of anisotropy, a more (wavy) lamella-like configuration could be seen, as in Fig. 4.5b, yet an ideal lamellar structure seems never possible. Moreover, co-existence of a lamellar and rod-like structures could also be possible for suitable degrees of anisotropy. Note, for equal phase fractions with equal interphase energies such patterns are never seen [92]. Thus, anisotropy in the interphase boundaries modifies the pattern selection mechanisms in eutectic solidification.

Even though the four-fold symmetry of the anisotropy is the most important one for metallic alloys, effects from the two-fold anisotropy can be quite significant in the S-S

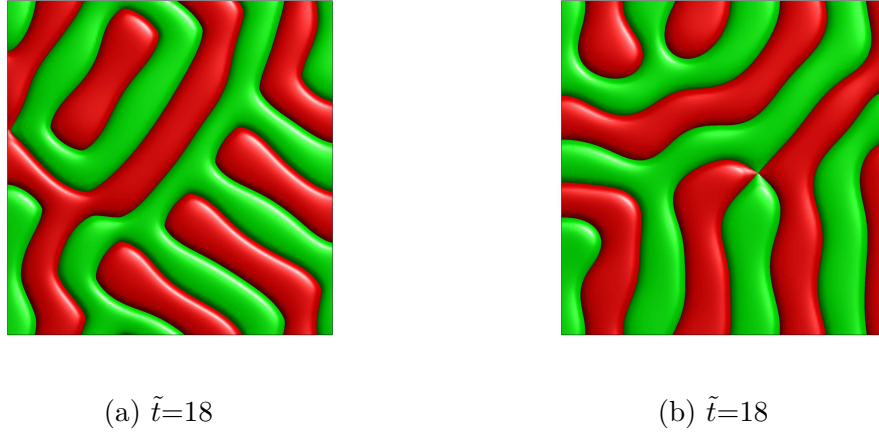


Figure 4.5: 4-fold phase evolution for  $a_c = 1 + \epsilon_4 \cos[4(\varphi - \varphi_R)]$ :  $\epsilon_4 = 6\%$  in Fig. 4.5a and  $0.5\%$  in Fig. 4.5b;  $\varphi_R = 40^\circ$ . Colors of  $\alpha$  and  $\beta$  are red and green, respectively.

interface formation during directional solidification [6, 45]. Four-fold is natural for S-L interfaces because of the interaction between a cubic (solid) and an isotropic (liquid) phase, whereas two-fold is natural for S-S interfaces because of the interaction between two cubic solid phases. Moreover, as explained in Chapter 3, at the interphase boundaries, where two centrosymmetric crystals meet, a 2-fold anisotropy is always expected (since two opposite orientation vectors describe the same surface). If we apply a two-fold anisotropy in the transverse plane ( $xy$ ) of the growing solid or in the plane of the isotherms, we obtain a perfectly periodic regular lamellar structure (Fig. 4.6). In other words, 2-fold anisotropy induces a favourable orientation to the lamellar arrangement in the transverse plane of the growing solid. Note that, the minimum energy directions in Figs. 4.6a,4.6b are selected by the anisotropic interphase energy  $a_c(\varphi - \varphi_R)$  and also by the geometric conditions set at the boundaries.

We have studied the kinetics and statistics of these regular lamellar microstructures. In particular, we focus on the time scale over which an absolute random pattern evolves into a perfectly ordered state and, subsequently, compare the kinetics of such ordering for varying strengths of anisotropy. At first, we measure the local orientation angles ( $\Theta$ ) of the corresponding interfaces. We gather the statistics of the interfaces of the sample plane in terms of  $\Theta_i$  and then calculate the standard deviation,  $\Delta\Theta$ , of  $N$  interface points with

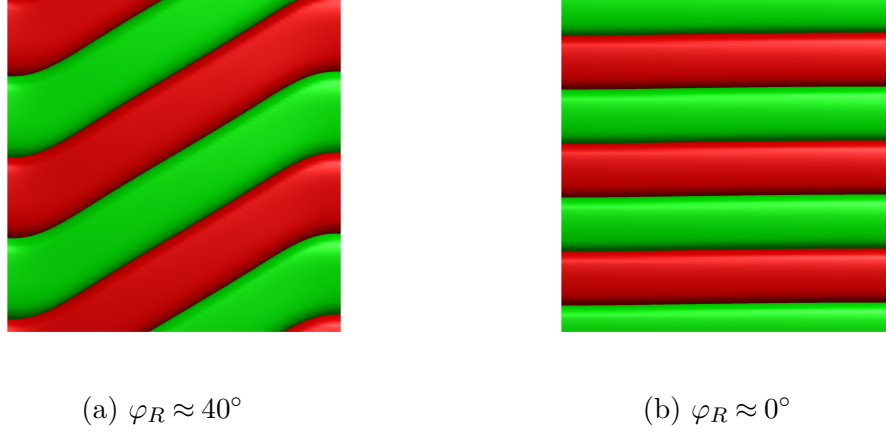


Figure 4.6: An initial random configuration of Fig. 4.4a with Neumann boundary condition along one of the directions in the azimuthal plane results into ideal lamellar arrays with a preferred direction at  $\tilde{t}=36$ . The anisotropy function being used:  $a_c = 1 + 0.3 \cos[2(\varphi - \varphi_R)]$ . Colors of  $\alpha$  and  $\beta$  are red and green, respectively.

an average of all  $\Theta_i$ ,  $\langle \Theta \rangle$ , using the expression:

$$\Delta\Theta = \sqrt{\frac{1}{N} \sum_{i=1}^N (\Theta_i - \langle \Theta \rangle)^2} \quad (4.3)$$

In Fig. 4.7, we show the temporal evolution of  $(\log)\Delta\Theta$  for different strengths of 2-fold anisotropy. Two things are evident from this figure: first, variation of  $\Delta\Theta$  or spread in orientation decreases with time. This suggests that the system is becoming more and more regular with time by decreasing the number of distinct orientations of the  $\alpha\beta$  solid interfaces. Second, as the strength of anisotropy increases, the rate at which the systems gets ordered is amplified. This can be understood by verifying the variation of slopes that the temporal orientational variation makes for various strengths of anisotropy in Fig. 4.7. All of these signify that the characteristics of these systems can be expressed mathematically by a standard exponential decay equation of the first order:  $\Delta\Theta \approx A \exp(-t/\tau)$ ;  $A$  is a constant and  $1/\tau$  is the decay rate. Note, for  $\epsilon_2$  of 15%, 20% and 30%, we obtain similar characteristic decay rates which can be due to a smaller simulation domain.

There are several other interesting features arise from these microstructures. Refer to the plateau forms for  $\epsilon_2 = 10\%$  in Fig. 4.7. This corresponds to a defect or fault

formation in the microstructure, similar to the one shown in Fig. 4.8a. These faults are inherent in bulk solidification microstructures and it can significantly reduce the kinetics of the topological connections between the phases. Mathematically, this can be explained as follows. As the defects hinder the possible connections between phases with its counterparts, the orientation distribution ( $\Delta\Theta$ ) of the evolving ( $\alpha\beta$ ) interfaces does not evolve any further, and we end up with a stagnant plateau in the temporal  $\Delta\Theta$  plot. If, somehow, these defects get eliminated from the microstructure, then, a perfect regular structure is obtained. As the system becomes free from the defects,  $\Delta\Theta$  exhibit the exponential behaviour with time. This is illustrated in Fig. 4.7, for  $\epsilon_2 = 10\%$ , where removal of defects (see the sharp change in the slope) triggers an exponential decaying of  $\Delta\Theta$ , similar to the non-defect forming systems ( $\epsilon_2 = 30\%, 25\%$  etc.). However, in the long run, it may also be possible that the defect is stable and can not be eliminated. In that case, the system can not rearrange itself into a regular array (Fig. 4.8a), and a horizontal plateau forms in the temporal  $\Delta\Theta$  plot (Fig. 4.8b). This clearly suggests that anisotropy itself can not remove the defects from microstructures.

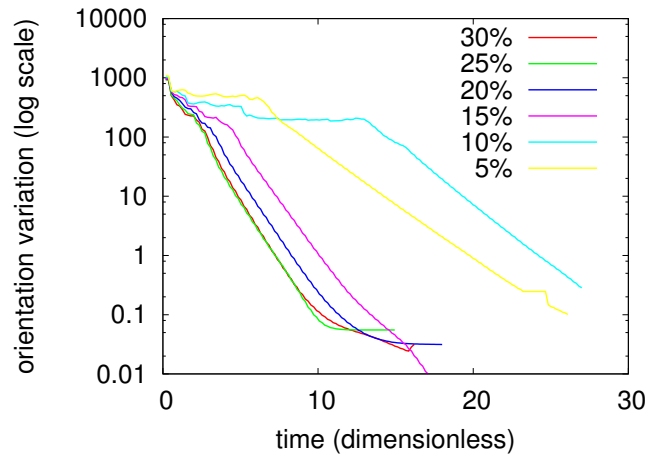


Figure 4.7: Temporal variation of spread in orientation for various strengths of 2-fold anisotropy

Next, we have examined the effects of 2-fold anisotropy on the interphase boundary components ( $\alpha\beta$ ,  $\alpha L$ ,  $\beta L$ ) in regard to the origin of the preferable orientations in the above described regular lamellar structures. Numerically speaking, separately, 2-fold anisotropy on either S-S or on S-L interfaces bring into existence a perfect lamellae (Figs.

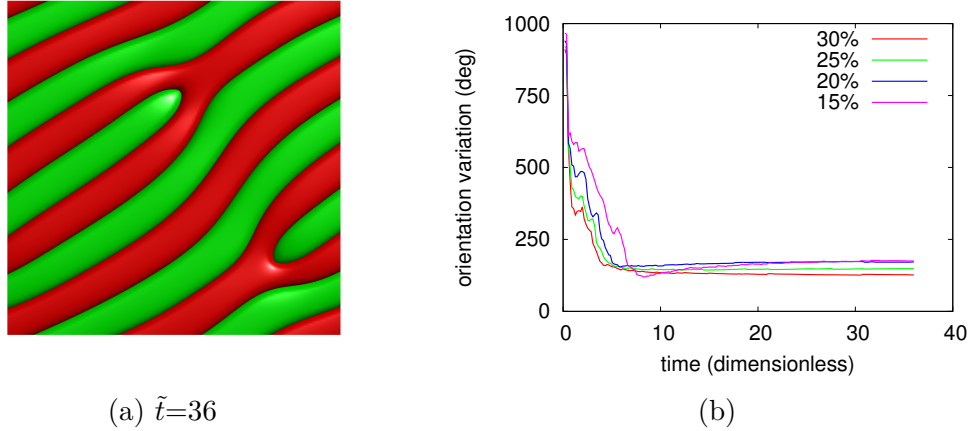


Figure 4.8: (a) Formation of a defect in lamellar solidification (b) Spread in orientation with time

4.9a, 4.9b); the preferred alignment of which is set by anisotropy of either S-S or S-L anisotropic boundaries. To identify this component, we perform a simulation where both type of interfaces are equally anisotropic (same  $\epsilon_2$ ), yet they experience different azimuthal rotation angles  $\varphi_R$ . Recall,  $\varphi_R$  (Fig. 2.2) selects the orientations of the resulting  $\alpha\beta$  lamellae in the azimuthal plane. In this setting, the S-S interface is not assigned any kind of rotation ( $\varphi = 0^\circ$ ) whereas S-L interfaces are rotated by an arbitrary angle other than zero (say,  $\varphi = 40^\circ$ ). The result is shown in Fig. 4.9b, in which the rotation angle the resultant pattern selects, corresponds to the minimum energy orientation of the S-S interface. The statistical distribution of the local interface orientation angles ( $\approx 0^\circ$ ) of the S-S interfaces in Fig. 4.9c indeed proves this point. Thus, qualitatively, it is confirmed that favourable orientations of the  $\alpha\beta$  crystals correspond to the minimum of the S-S interface energy.

### 4.3.3 Multiple eutectic grains

Until now, we have discussed the development of preferred orientations in a single eutectic grain consisting of one set of eutectic phases  $\alpha$  and  $\beta$ . However, an experimental microstructure generally contains multiple grains with many chemically and/or physically similar or dissimilar phases, which triggers even more complex interactions between preferred



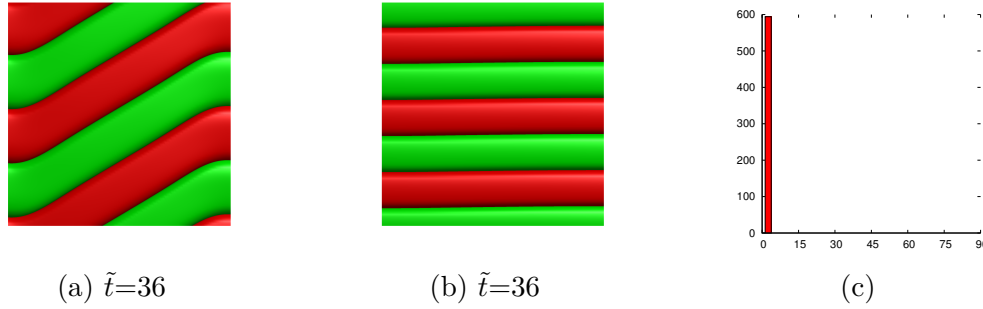


Figure 4.9: An initial random configuration of Fig. 4.4a with isolate boundary condition along one of the directions: (a) an ideal lamellar arrays with a preferred direction, (b) arrays are arranged at a zero angle with  $y$  axis, (c) histogram of interface orientation angles, scanned from a plane of Img. 4.9b. Colors of  $\alpha$  and  $\beta$  are red and green, respectively.

directions and interfacial energies in between them. Recent experiments by Hecht et al. [97] suggest that the irregular eutectic maze structures that form in Al - Cu alloys (Fig. 4.4b) never become regular in experimentally accessible time scale unless such mazes are forced into regular arrays by some factors. Lateral temperature gradient is one of the factors [93]. The other potential factor can be the anisotropy of the interphase boundaries [97]. In the Al-Al<sub>2</sub>Cu binary microstructures, which form during bulk eutectic solidification of Al-Cu-Ag ternary alloys, the initial phase evolution is labyrinthine which eventually leads to few locally regular regions. These are locally aligned at favourable directions but they do not belong to the energy minimum of the interphase orientation relationships. Once these relationships are established at the growth front, the favourable orientations outgrow the unfavourable orientations. In this way, the most competitive grain wins in the multi-grain eutectic solidification process. In the present work, we make a first attempt towards the understanding of the transformation of mazes into a regular lamellar pattern using numerical simulations. To study this, minimally, we need two different eutectic grains, i.e, two sets of  $\alpha, \beta$  phases, labelled as  $\alpha_1\beta_1$  and  $\alpha_2\beta_2$ . These grains are chemically homogeneous: compositions of  $\alpha_1$  and  $\beta_1$  in grain 1 is equivalent to  $\alpha_2$  and  $\beta_2$ , respectively, in grain 2. In turn, this makes  $\alpha_1/\alpha_2$  and  $\beta_1/\beta_2$  behave like grain boundaries (GB), which are treated as isotropic. The S-S boundaries between  $\alpha_1/\beta_1$  are treated as anisotropic whereas the  $\alpha_2/\beta_2$  S-S boundaries are considered isotropic. As we have more phases in the simulation box now, evolution of initial “random pattern” (Fig. 4.10a) is even more

violent than the single grain simulations, and it was required to use larger cube edges, in the order of eight times the grid spacing, to stabilize the evolving structure.

Our primary objective is to study the competition between different orientations represented by these two grains as well as to address the stability of the interfaces on the resultant morphologies. For this purpose, we vary the anisotropic  $\alpha_1/\beta_1$  interphase energy using suitable 2-fold anisotropy functions,

$$a_c = 1.0 + 0.3 \cos[2(\varphi - \varphi_R)] \quad (4.4)$$

$$a_c = 1.6 + 0.3 \cos[2(\varphi - \varphi_R)] \quad (4.5)$$

The essence of the anisotropy functions are such that for Eq. (4.4) the anisotropic interfaces possess minimum surface energy when compared to other interfaces in equilibrium. In contrast, Eq. (4.5) is used to increase the energy of anisotropic interfaces with reference to isotropic interfaces. In this way, we employ a microscopic orientation competition between the isotropic and anisotropic interfaces of these grains. Recall, the basis of isotropic surface energy is set by  $a_c = 1$ .

In Fig. 4.10, we show the microstructural evolution which corresponds to Eq. (4.4). Initially a labyrinth of all the phases form and the resultant microstructure is completely disordered. This further develops into a few local regular arrangements of the anisotropic  $\alpha_1\beta_1$  lamellae at certain places, yet the pattern is still globally disordered (Fig. 4.10b). These anisotropic local arrangements grow faster and become bigger because of higher undercooling present in front of them compared to the surrounding isotropic counterparts. This sets the driving force, and the anisotropic interfaces continue to grow by eating out the neighbouring isotropic interfaces until they completely outgrow them. And, finally, the system is left with only  $\alpha_1\beta_1$  anisotropic interfaces which are aligned along a minimum energy direction. This is quantified by a histogram plot of the volume fraction distribution of the existing phases with time (Fig. 4.11). In brief, surface tension anisotropy along the interphase boundaries induce a orientation relationship between the anisotropic phases yielding a regular lamellar array from an irregular eutectic maze (Figs. 4.4b, 4.10b).

However, on the other hand, if the  $\alpha_1\beta_1$  anisotropic interfaces possess higher energy

compared to  $\alpha_2\beta_2$  isotropic interfaces (Eq. (4.5)), no anisotropic interface is seen in steady state and several isolated islands of anisotropic  $\alpha_1\beta_1$  phases remain dispersed in the sea of isotropic  $\alpha_2\beta_2$  phases (Fig. 4.12). This confirms that at equilibrium the interfaces with overall minimum surface energy dominate the microstructure formation. In addition, compared to the previous situation, in this case, even though there are no anisotropic  $\alpha_1\beta_1$  interfaces exist at the end, still the system can not get rid of these  $\alpha_1\beta_1$  bulk phases. This can be explained as follows. As isotropic grain always give birth to a labyrinth, there is no distinct set of orientation relationship for  $\alpha_2\beta_2$  isotropic interfaces. Whereas, the anisotropic  $\alpha_1\beta_1$  interfaces have specific orientation relationship, however, in this case, it does not belong to the energy minimum of the inter-phase boundaries. Hence, energetically, there should be no anisotropic interfaces in the microstructures, yet the isotropic interfaces can not drive them out in the pattern selection process. In other words, there are two types of energy involved in this process: one for the interface formation and the other to align the interfaces at a favourable direction. As the energy required for the formation of anisotropic interfaces is higher, these interfaces are not stable and hence do not appear in the microstructures. Moreover, like in the previous case, it is possible to have a set of preferred orientations by anisotropic interfaces but the energy cost of these directions is higher. If, somehow, the anisotropic interfaces can be stabilized, for example by reducing the energy of the favourable directions using Eq. (4.4), then only, these interfaces can dominate the microstructure formation and subsequently overwhelm the other grains in the microstructure, resulting into a regular lamellae (like Fig. 4.10).

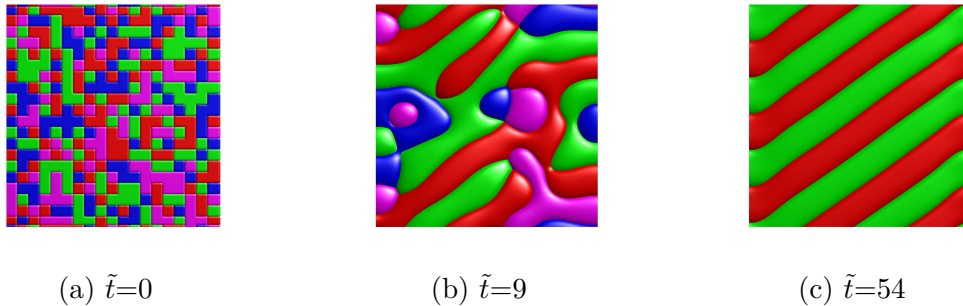


Figure 4.10: Temporal evolution of two eutectic grains according to Eq. (4.4); colors of  $\alpha_1$ ,  $\beta_1$ ,  $\alpha_2$  and  $\beta_2$  are red, green, blue and magenta, respectively. Note, interfaces between  $\alpha_1$  and  $\beta_1$  are anisotropic.

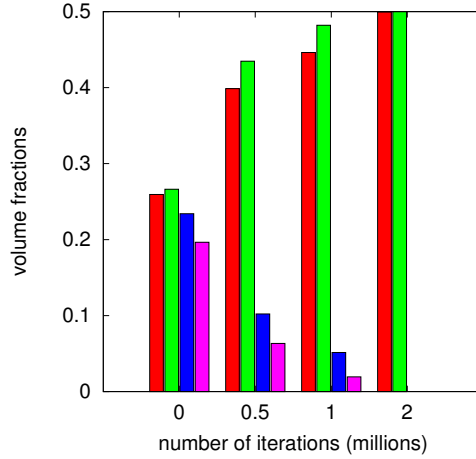


Figure 4.11: Histogram plot of volume fraction distribution with time for Fig. 4.11; colors of  $\alpha_1$ ,  $\beta_1$ ,  $\alpha_2$  and  $\beta_2$  are red, green, blue and magenta, respectively.

## 4.4 Conclusions and Outlook

We have studied the morphological evolution of a symmetric binary eutectic alloy in presence of the anisotropy in three dimensions. Anisotropy along the S-S interphase boundaries dominates the pattern formation in these bulk eutectic solidification microstructures. A wealth of morphologies can form in three dimensions. In absence of anisotropy, a complex network of lamellae or a labyrinth forms. If anisotropy (4-fold) is included along the interphase boundaries, unique patterns like zigzag- and wavy- lamallae appear in the microstructures. In addition, presence of weak anisotropy (2-fold) in the azimuthal plane of the growing solid leads to regular lamellar arrays with/without defects along with a preferred orientation, which is a minimum energy direction.

Next, we present simulation results with two different eutectic grains to study the competition between different orientations represented by these two grains. We use suitable 2-fold anisotropy functions to scale the interfacial energies between these two grains. In all steady state microstructures, first of all, it is seen that the existing interfaces belong to the lowest surface energy. In addition, we also show that the surface tension anisotropy forces a set of orientation relationships to the underlying crystal structure of the anisotropic grain. If these interface orientations correspond to the energy minima, then the anisotropic

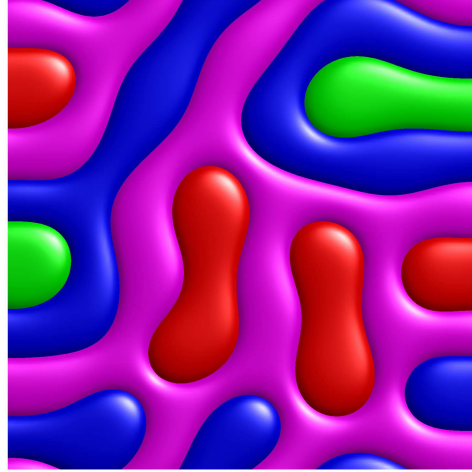


Figure 4.12:  $\alpha_1\beta_1$  anisotropic grain possess higher interfacial energies compared to  $\alpha_2\beta_2$  isotropic grain;  $\tilde{t} = 56$ , colors of  $\alpha_1$ ,  $\beta_1$ ,  $\alpha_2$  and  $\beta_2$  are red, green, blue and magenta, respectively.

grain grow at the expense of the isotropic grain and eventually wipes it out from the microstructure. Interestingly, this mechanism bears a significant consequence where a random disordered eutectic maze transforms into a regular lamellar array.

Even though the stability of the steady state patterns which is set by the speed ( $V$ ) - spacing ( $\lambda$ ) relationship during the coupled growth of the eutectic solids are well-known in isotropic systems [21] yet such picture is still incomplete in presence of complex anisotropic interactions. In addition, the range of phase fractions over which the “normal” morphologies, namely lamellae and rod, exist in presence of anisotropy needs to be verified. Lamella-rod transition would be an another interesting problem in this context. One could, furthermore, simulate a ternary system with an additional component to produce even an wider variety of fascinating morphologies.

# Chapter 5

## Influence of grain boundary anisotropy during directional solidification

### 5.1 Introduction

The onset of morphological instability and the subsequent microstructural evolution during unidirectional solidification, performed at a chosen velocity and fixed thermal gradient, is a significant aspect in physics and materials science because it is an excellent example to study interfacial phenomena and because it is an beautiful pattern forming process [2, 1]. Without GB, the instabilities that arise in the interfaces are defined by certain critical values of the control parameters, either by the pulling speed  $V$  or by the temperature gradient  $G$ . This is elaborated in Chapter 1. However, in the presence of grain boundaries, the picture is more complicated. Because, now, the solute profile ahead of the solid-melt interface interacts with the GB groove at the trijunction [98]. Along this direction, Coriell and Sekerka [99] first studied the morphological instability in presence of such GBs and suggested that the GB groove itself acts as a source of undulation, which evolves into cells at the same critical values predicted by MS. All these instability limits are successfully elucidated in numerous experimental and numerical studies [10, 11, 99, 100, 101].

In a microstructure, when two grains grow next to each other, a GB forms with a groove in between them. The misorientation between these grains distinguishes two different types of GB attached to the groove: high-angle GB (HAGB) and low-angle GB (LAGB) or sub-boundary (SB) [102]. These grain boundaries possess quite different physical properties; for instance, SBs form at the lower temperature and, hence, are relatively dry and, thus, it can possess significant capillary anisotropy [69]. This adds another level of complexity to the interactions between the trijunction groove and the solute profiles ahead of it. Despite decades of research, a very little is known about these complex interactions.

A experimental study by Bottin et al. [69] examined the effects of SB anisotropy on the orientation selection of the participating grains. They suggested that, if the solidification velocity remains below the CS limit, SBs grow at a finite angle with respect to the growth axis. Then, as the velocity exceeds this limit, it can not continue to grow with this drift angle; an instability is already activated around the trijunction, initiating a breakdown of the planar solid-melt interface, and, as a result, SBs start to grow towards the growth direction. Thereafter, as the velocity hits the cellular-instability MS threshold, the nearly planar interface completely breaks into cellular structures with the formation of shallower or deeper grooves, accompanied with amplified solute profiles. In this regime, SBs are found to be growing perpendicular to the growth front.

The corresponding analytical calculations as well as the theoretical approach of the aforementioned work of Bottin et al. [69] has been meticulously illustrated by Faivre et al. in a recent work [103]. Interestingly, a recent similar study on lamellar eutectic growth has been pursued along this direction [72]. In this present work, as a first attempt, we explore such influence of the SB anisotropy towards the orientation selection in the spirit of morphological instabilities delimited by the CS and MS critical velocities using numerical calculations.

We attempt to simulate the growth of a GB in the presence of anisotropy, for different pulling velocities ranging from 0 to the cellular-instability threshold and beyond. Moreover, mobility of these boundaries are found to be significantly affecting the steady state morphologies. Finally, we shed some light on the orientation selection in the presence

of multiple SBs present in the simulation box. The structure of this chapter is arranged as follows. In the next section, we provide the necessary background details of our work regarding the instability limits, physical characteristics of different types of grain boundaries and the theoretical prediction of the tilt angle of the anisotropic SBs. In Sec. 5.3, we describe the significant parameters in the phase-field code which controls the morphological evolution. In Sec. 5.4, results are presented for the evolution of anisotropic SBs in three different velocity regimes: below CS, above MS and in between these two limits. Finally, a conclusion is drawn and a short perspective is given in Sec. 5.5.

## 5.2 Background

### 5.2.1 Morphological instability

Morphological instability determines the shape of a S-L interface in a crystallization process. Referring to the Chapter. 1, in essence, below  $V_{MS}$  the S-L interfaces grow with a planar or a nearly planar front. And above  $V_{MS}$ , the cellular-instability threshold, the planar or nearly planar interface completely breaks into cells and then dendrites.

### 5.2.2 Grain Boundary (GB) and Sub-Boundary (SB)

When two grains with chemical homogeneity impinge on each other, a GB forms in between them [13, 104] (see Fig. 5.1). At the GB, these grains meet at a dihedral angle of  $\alpha$  and, thus, a groove is formed in response to the force balance of the GB and S-L boundary tensions.

$$\alpha = 2 \cos^{-1} \left( \frac{\gamma_{gb}}{2\gamma_{sl}} \right) \quad (5.1)$$

When the angle between these adjoining grains is large enough, the result is a high-angle GB. The recent experiments of Bottin et al. [69] suggest that these boundaries are wetted by the liquid and become mobile. Contrary to this, a low-angle GBs or SBs form, which are essentially dry and are almost immobile. Moreover, because of such wetting, HAGBs



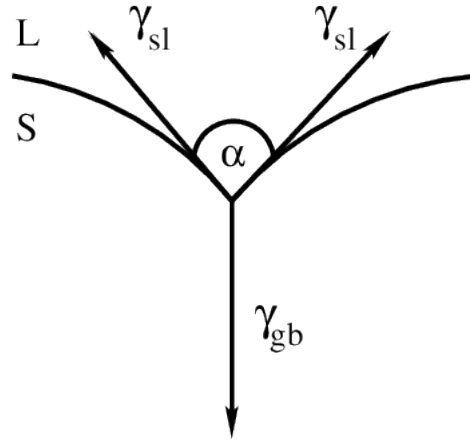


Figure 5.1: Formation of a GB groove by balancing the surface and GB tensions at the intersection of a GB with a free surface

are generally isotropic and grows essentially parallel to the growth direction, intersecting the S-L boundary at right angles. In contrast, sub-boundaries are dry, and can possess significant amount of capillary anisotropy leading to the lateral drift of the SBs at an angle with the growth axis [69]. Moreover, these SBs can change their growth directions, or, precisely, the tilt angles, depending on the interactions with the neighbouring boundaries.

Coriell and Sekerka [99] first studied the effects of such boundaries on the morphological instabilities. They concluded that the GB itself can provide a built-in distortion to the S-L interfaces, which remains planar below  $V_{MS}$ , and, with increasing velocity, at first, parallel ridges form around the groove signifying the onset of CS limit, and, then, after surpassing  $V_{MS}$ , cellular or dendritic structure results.

### 5.2.3 Anisotropic interphase boundaries

As discussed in Sec. 5.2.2 that HAGB's are isotropic in nature, and grow parallel to the growth direction. Hence, a local equilibrium exist at the trijunction satisfied by Young's law:  $\gamma_{1L}\hat{t}_{1L} + \gamma_{2L}\hat{t}_{2L} + \gamma_{gb}\hat{t} = 0$ . In contrast, SBs are strongly anisotropic, and, hence, the trijunction obeys the anisotropic Young-Herring equation [103]. Considering Fig. 5.2, we arrive at:

$$\gamma_{1L}\hat{t}_{1L} + \gamma_{2L}\hat{t}_{2L} + \vec{\sigma} = 0 \quad (5.2)$$

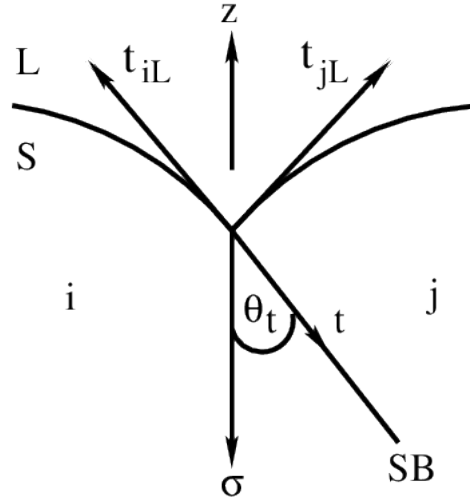


Figure 5.2: Anisotropic force balance at a SB trijunction in unidirectional solidification

In order to study the anisotropic behaviour of the SB, one needs to impart a suitable anisotropy function to the SB, and then, follow the response of this boundary to this function. One of such function could be of the following shape (Eq. (5.3)), which is composed of smooth Gaussian minimum, which is an approximation for a cusp, to make it mathematically differentiable with respect to the interface orientation angle  $\theta$  (similar to Eq. (3.4)).

$$a_c(\theta) = 1 - \epsilon_g \exp\left[-\frac{\theta^2}{w_g^2}\right] \quad (5.3)$$

Here,  $\epsilon_g$  is the magnitude of the anisotropy and  $w_g$  is the width of the cusp. The motivation behind using such anisotropy function is that when the system stays at the cusp, the SB follows an minimum energy configuration with a certain amount of torque ( $d\gamma/d\theta$ ) being present at the trijunction making the SB groove asymmetric. In contrast, the system remains isotropic while it stays outside of the cusp, i.e., in the horizontal part of the  $\gamma - \theta$  plot (refer Fig. C.3a in appendix C).

#### 5.2.4 Theoretical prediction of the tilt angle

Recall that the Young-Herring condition (Eq. (5.2)) is satisfied at the anisotropic SB trijunctions. In the spirit of experimental observations related to a straight and a tilted

SB, the S-L interfaces does not see any change in its shape as it remains almost mirror symmetric in both the cases. This signifies that, the major effect of anisotropy is included in the SB itself. Believing this is strictly true,  $\vec{\sigma}$  vector of the SB should direct parallel to the growth direction  $z$  ( $\vec{\sigma} \parallel z$ ). Under these hypotheses, differentiating the  $\vec{\sigma}$  vector with respect to the  $x$  coordinate must gives zero, resulting into a non-linear equation similar to Eq. (3.7). This equation gives analytical solutions, in terms of  $\theta_t$ , for an arbitrary  $\theta_R$ , against which we will compare our numerical results.

The above analysis is valid as long as the S-L interface is planar or nearly-planar, indicating that the system is below CS limit. Beyond this limit, the morphological instabilities come into play (refer Sec. 5.2.1). A recent theoretical study by Faivre et al. [103] has shed some light regarding the growth direction of the SB in this morphologically unstable regime. Their work suggests that, as the planar interface starts to break while reaching the CS limit, the SB can not continue to grow laterally, and the angle it makes with the growth axis decreases rapidly with the increasing velocity, and when MS velocity limit is reached, the SB should grow parallel to the growth direction, similar to an isotropic GB. In essence, for  $V < V_{MS}$ , the SB should tilt at a finite angle following Eq. (3.7); for  $V_{MS} < V < V_{MS}$ , the tilt angle should decrease rapidly; and for  $V > V_{MS}$ , SB should grow parallel to the growth direction  $z$ . The following figure schematically represents these three regimes of SB tilt angles in response to the system velocity  $V$ .

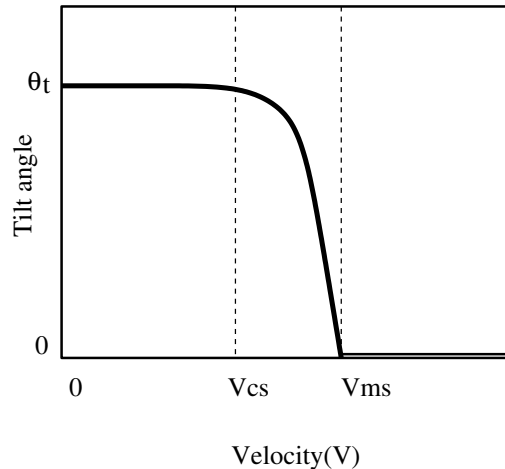


Figure 5.3: Schematic representation of the tilt angles ( $\theta_t$ ) in three different velocity ( $V$ ) regimes during directional solidification

## 5.3 Method

Recall that, for eutectic solidification, two dissimilar chemical phases, namely  $\alpha$  and  $\beta$ , constitute the system. In contrast, here, we use two grains of the same phase, say  $\alpha_1$  and  $\alpha_2$ , to make up the system. This way, a GB is introduced in the system between these grains. Anisotropy is imparted in this S-S boundary and we examine its evolution with time for different velocities — below CS limit, in between CS and MS limit and above MS limit — using the standard evolution equations for the phase fields and the composition fields in a multi-phase-field method, as described in Chapter 2.

### 5.3.1 Parameters

We constitute a dilute alloy system by considering only the one side of a generic symmetric eutectic phase diagram. Then, we constitute two phases of same chemical composition of this dilute alloy to make up the system. These phases share same length scales, which describe the system, namely,  $l_D$ ,  $l_T$  and  $d_0$ . The definitions of these lengths can be found in Sec. 1.2.3. Moreover, we still use parallel solidus and liquidus lines which signifies the partition coefficient  $k = 1$ .

Recall, GB provides a built-in distortion to the adjoining solid-melt interfaces and we explore the effects of this deformation to develop into cellular structures, which appear at a length scale comparable to the MS linear stability theory (refer Sec. 1.2.3). Therefore, in order to study such behaviour, the system size should be within the marginal stability limits (onset of positive  $w_k$ ) of MS analysis. In our present work, for the smallest system, the simulated box has a length of  $\lambda/d_0 \approx 20$ , and, similarly, for the largest system, it is  $\approx 40$ .

Moreover, we examine the intensity of this instability by decreasing the temperature gradient  $G$  or by increasing the solidification rate  $V$ . This modifies the thermal ( $l_T$ ) and diffusive ( $l_D$ ) length scales of the system. Noting,  $l_T = l_D$  determines the CS limit as well as the  $V_{MS}$ , we have used a minimum value of  $l_T/l_D \approx 1.5$ , which is above the MS limit, to simulate cellular structures with shallower grooves. Furthermore, the maximum value of  $l_T/l_D \approx 30$  is used to study deep cells. The corresponding  $d_0/l_T$  values for the

aforementioned  $l_T/l_D$  ratios are  $\approx 0.06$  and  $0.3$ , respectively. Referring to Eq. (1.17), the calculated values for  $\lambda_{MS}$  for the two systems described above are  $\approx 70$  and  $\approx 160$ , respectively.

## 5.4 Results

We probe the orientation of a anisotropic SB in three different velocity regimes: below the CS limit, above the MS limit and in between these two limits. In addition, we also examine the interaction between multiple SBs towards the orientation selection around these critical limits.

### 5.4.1 Behaviour of SB below CS

In Fig. 5.4(a), we show the equilibrium orientation of a SB for a situation when the solidification velocity is below the CS limit. As expected, the solid-melt interface remains planar or nearly planar in this regime and the anisotropic SB makes a finite angle with the growth axis  $z$ . This tilt angle of the SB is verified with the SP approximation, as explained in Sec.5.2.4. In Fig. 5.4(b), we present the analytical solutions of the SB tilt angles using this approximation. Considering the anisotropy function (Eq. (5.3)) used in our simulations, there exists three branches of analytical solutions. One correspond to a locked branch, in between  $0 \sim 70$  deg rotations: this is a minimum energy plane along which the boundaries tend to align preferentially. Another stable branch is at zero angle, in between  $15 \sim 90$  deg rotations, to signify the growth of the boundaries parallel to growth direction. Moreover, in addition to these stable branches, there exists one unstable branch of negative surface stiffness ( $\gamma + \gamma'' < 0$ ) connecting the ends of the aforementioned branches. Therefore, this anisotropy function exposes multiple tilt solutions for a arbitrary rotation angle imparted on the bi-crystal.

We superimpose the numerically obtained tilt angles of the SB on the analytical curve in Fig. 5.4(b). We successfully simulate these angles, precisely, 0-20 degrees, on the locked branch, and 21 - 90 degrees, on the unlocked branch. Even though, our results closely

follow the SP theoretical prediction, however, we did not find more than one tilt angle of SB, for a particular rotation angle. Interestingly, below CS regime, sub-boundaries behave similar to the interphase boundaries in lamellar eutectics [72], as long the solid-melt interface remains nearly planar. Moreover, in the eutectic study, also, no bi-stable solutions were found using phase field simulations. Note, in the eutectic case, we obtained solutions along the locked branch upto  $\sim 35$  degrees. This discrepancy between eutectic and GB can be due to the fact that the solute diffusion field is very different when compared to eutectics: solute is rejected on both sides of the trijunction here, whereas it diffuses from one side to the other in eutectics.

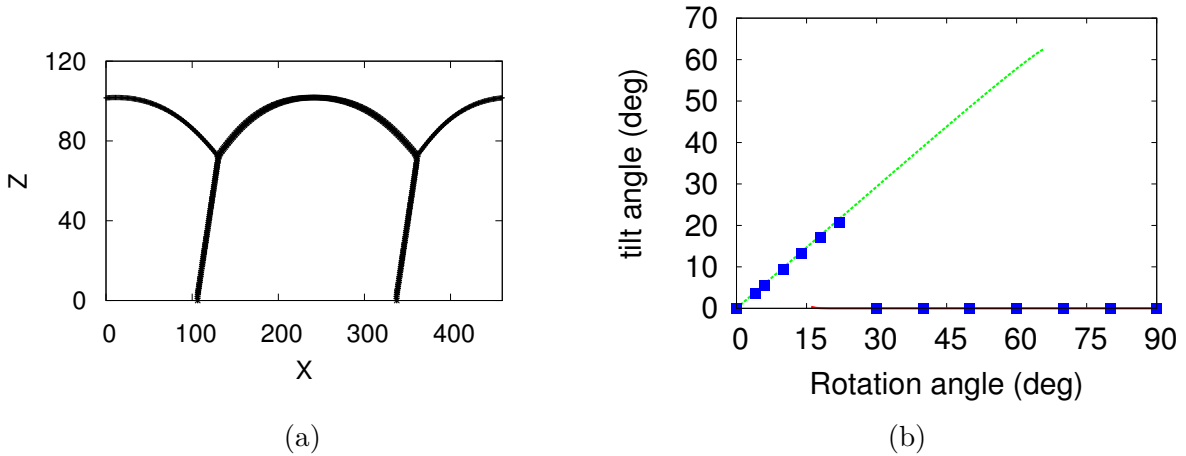


Figure 5.4: Below CS: (a) SB tilts at a finite angle with a planar solid-melt interface (b) numerically obtained SB tilt angles are imposed on the analytical solution of Eq. (3.7)

### 5.4.2 Above MS

Above MS critical velocity, cellular structure results with shallower or deeper grooves depending on the value of the ratio  $G/V$ . In this regime the degree of distortion around the SB can be very large, and may lead to a very wavy SB profile, as shown in Fig. 5.5. Such wavy nature makes it inconvenient to measure the tilt angle of the boundaries. The behaviour suggests that the PF model equations are ill-posed in this regime. To overcome such a strong curvature features along SB, we regularize the free energy of the SB with a

procedure outlined in Sec. 2.6.2.

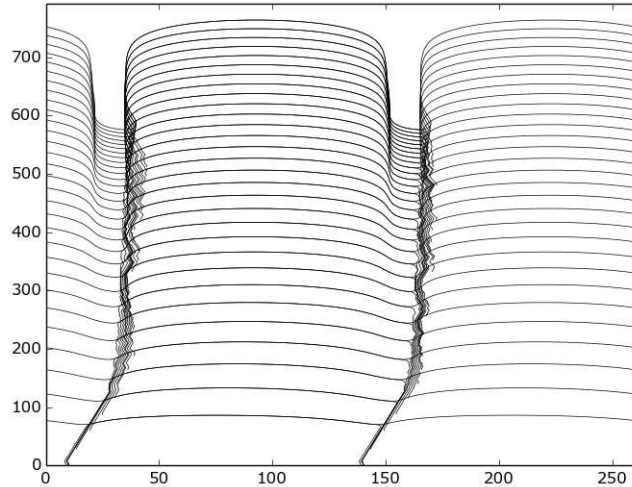


Figure 5.5: Superimposed snapshot pictures of the interfaces above MS suggests a Herring instability along the S-S boundary. Note that units of lengths are in grid spacing.

### Effect of finite mobility

The effects of the regularization are shown in Fig. 5.6. The first obvious effect is that the sharp curvature features along the boundaries are gone to end up with a smooth profile. Moreover, it exposes the intrinsic mobile nature of the grain boundaries between the two chemically homogeneous phases. The temporal drift of the boundaries (towards left) proves this point. In these circumstances, we found that the SB behaves in a similar way to as below CS, i.e., it grows at a finite angle. This signifies that the locked branch remains locked and the unlocked branch remains unlocked even beyond the MS velocity, in the presence of finite mobility of the SB. However, the theory predicts that, in this regime, SB should grow straight to make a zero angle with respect to the growth axis. Interestingly, even though the SB can not orient itself straight, the trajectory of the trijunction in the spatio-temporal plot falls onto a nearly straight line (see Fig. 5.6). In essence, the trijunction, in this case, obeys the theoretical prediction, while the SB behind it does not. This motivates us to make the boundaries immobile to follow the trijunction trajectory in the subsequent numerical simulations.

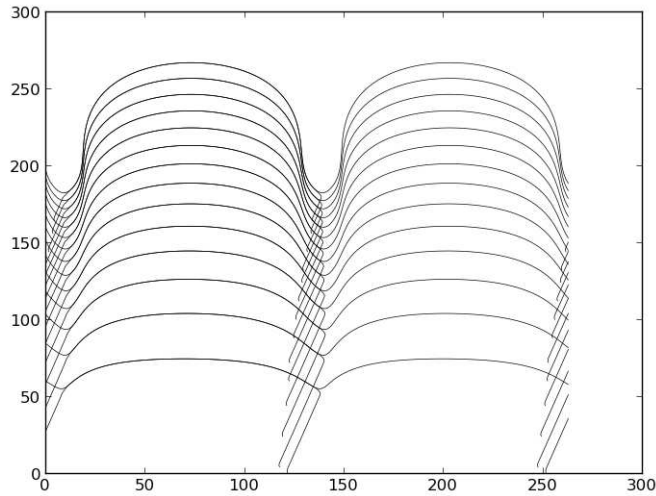


Figure 5.6: Superimposed snapshot pictures of the interfaces above MS: effects of finite mobility on the orientation selection of SB. Note that units of lengths are in grid spacing.

### Effect of zero mobility

We adopt two ways to imply zero mobility to the SB's in our numerical simulations. In our multi-phase-field code, mobility of the individual boundaries can be altered by modifying the relaxation coefficient ( $\tau$ ) during the evolution of the order parameter in the Allen-Cahn equation (Compare Eq. (2.11) and Eq. (2.20)). Note that, the mobility varies inversely proportionally with  $\tau$ . We use  $\tau_{gb} \gg \tau_{sl}$  to make the kinetics of the SB slower, compared to the solid-melt interfaces. One more approach to this problem can be pursued by multiplying a factor to the  $\tau$  of the solid(1)-solid(2) boundaries as follows:

$$\tau_{12} = \frac{1}{\tau_{12}} \left(1 - \frac{1}{4} \phi_1 \phi_2\right) \quad (5.4)$$

This essentially makes the mobility zero for the order parameter ( $\phi$ ) contour of 0.5, which denotes the boundary between phases  $\alpha_1$  and  $\alpha_2$ . We check, these two approaches essentially give similar picture of the SB dynamics. In our present work, we use the first approach to modify the SB mobility.

The results for the mobility modification of the SB is shown in Fig. 5.7(a). As expected, the SB, now, behave like the trijunction, as in the previous case, and follow the straight trajectory of the trijunction. Moreover, at the beginning, the SB attempts to orient



towards minimum energy direction set by the anisotropy of the SB; however, the strong instability gradient set by a velocity far beyond the MS limit force the SB to make a sharp transition towards the zero angle orientation. Another physical explanation to this could be that, the SB is unable not drift laterally with the massive liquid present at its groove and, hence, tilts back towards the straight direction. Thus, we obtain the zero angle branch of the SB in this regime, as predicted by the theoretical calculations (refer Fig. 5.3). It is worthwhile to mention here that the asymmetric GB groove profile in Fig. 5.7(b) forms due to the presence of the system at the cusp of the anisotropy function leading to a finite torque at the trijunction.

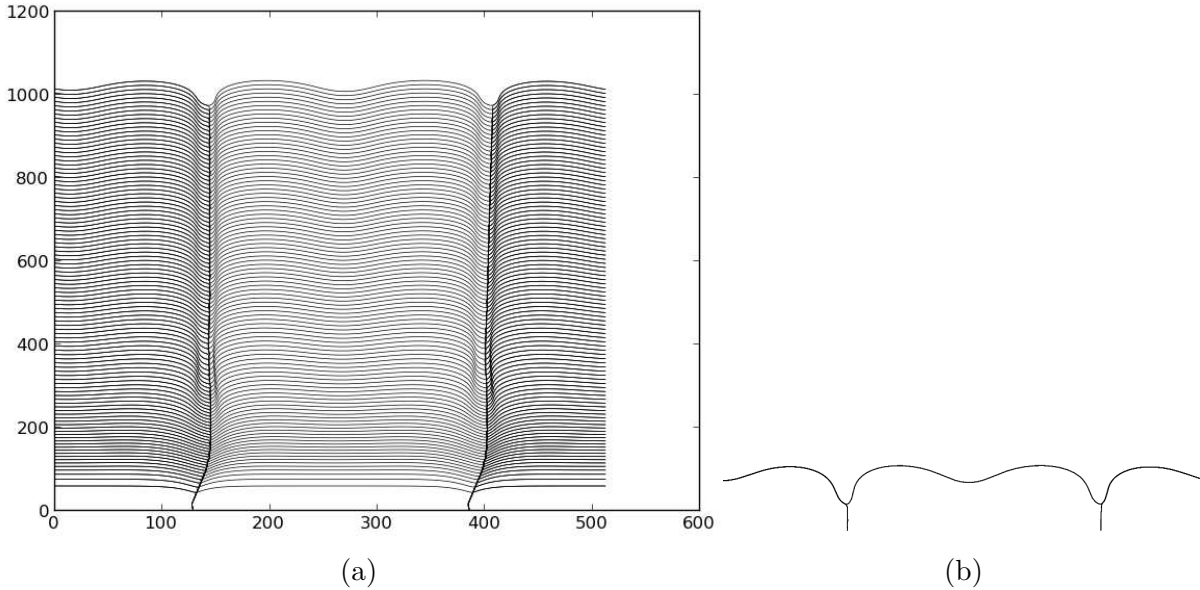


Figure 5.7: (a) Superimposed snapshot pictures of the interfaces above MS: Effects of zero mobility on the SB (b) Asymmetry of the GB groove profile

### 5.4.3 Above CS, Below MS

When the system crosses the CS limit, planar interface starts to break down. Two parallel ridges or hump forms around the GB groove signifying the onset of CS, and this hump continues to grow into cells when MS limit is reached. Therefore, the approximation to predict the SB orientation ( $\vec{\sigma}||z$ ) deviates strongly as we move further from CS limit, and

hence, the tilt angle starts to decrease rapidly. It is difficult to quantify the SB orientations in this regime, because the interface shapes depend strongly on the proximity to these limits. For example, SB orientation, immediately after the CS limit will not be similar to the orientation immediately before the MS limit, since the solid-melt interfaces have been changed significantly, resulting into a different local equilibrium condition at the trijunction. Therefore, we show one of such orientation map of SB in this regime in Fig. 5.8. Two things are obvious from this spatio-temporal orientation diagram. SB stays in the locked state or minimum energy direction for a longer time, and the transition from the high angle branch to the low angle branch is smoothly varying. Plus, in this regime, the theoretically predicted tilt angle is rather small yet non-zero. Therefore, the morphologies formed in this limit pose striking differences in compared to the morphologies formed above MS velocity.

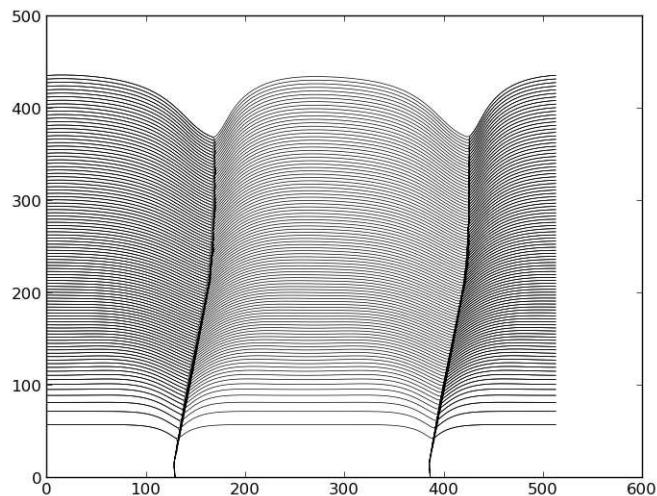


Figure 5.8: Superimposed snapshot pictures of the interfaces in between the CS and MS critical velocity limits

#### 5.4.4 Interaction between SBs

Experimentally, it is seen that the SB in a microstructure interact with the neighbouring SBs [69]. We present few simulations with interacting SBs to shed some light along this direction. The interaction is set between SBs, which can be either isotropic or anisotropic, and the regime we scan is below CS as well as above MS.

### Below MS

We present results for below the CS limit, where one of the SBs is anisotropic and others are isotropic, in Fig. 5.9. We observe that the isotropic SB grows parallel and the anisotropic SB drifts at an angle with the growth axis. This is expected, as both SBs are already set at minimum energy directions, and hence, they do not interact with each other except the spacing adjustments, in between the grains, to orient the boundaries in the preferred directions. Moreover, as the solid-melt interfaces grow with a planar front, these preferred directions can be quantified by the SP approximation theory. When all the boundaries

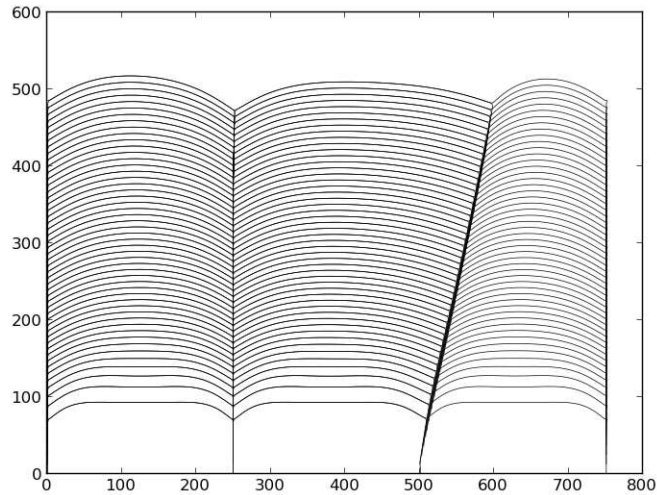


Figure 5.9: Superimposed snapshot pictures of the interfaces below CS: interaction between isotropic and anisotropic SBs

are anisotropic, the corresponding result is shown in Fig. 5.10. All the SBs follow the minimum energy direction set by the anisotropy.

### Above MS

Above the MS limit, anisotropic SBs change orientations, and during this dynamical process, they can interact with the neighbouring boundaries leading to optimal directions in which the boundaries grow all together. In Fig. 5.11, we show an instance of such interactions between SBs. Effects of this interaction is obvious in the anisotropic SB, which changes direction appreciably with time. When the anisotropic SB changes direction, it

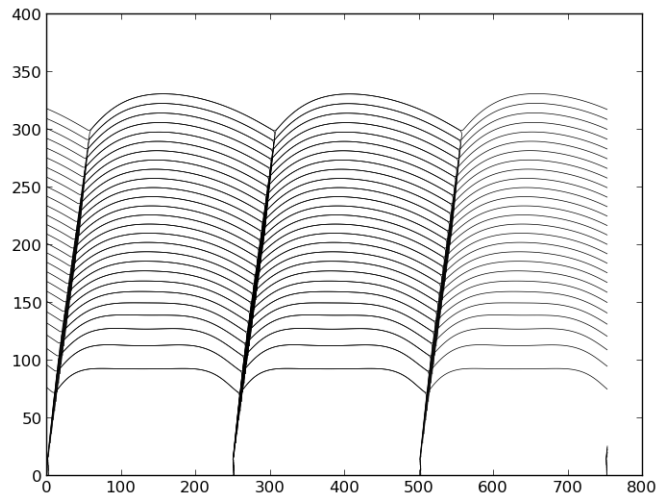


Figure 5.10: Superimposed snapshot pictures of the interfaces below CS: interaction between anisotropic SBs

attracts the SB close to it leading to an optimal spacing of the individual grains in the morphology. And, once, the optimal spacing is established for each grains, sub-boundaries follow their minimum energy directions and grow parallel to the growth direction.

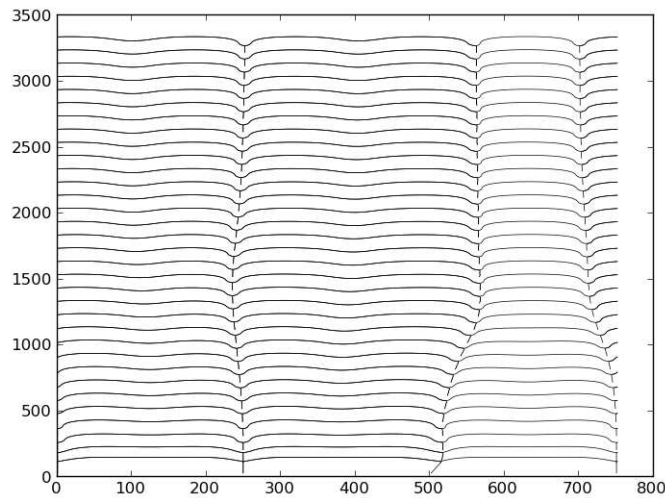


Figure 5.11: Superimposed snapshot pictures of the interfaces above MS: interaction between isotropic and anisotropic SBs

The results for interaction between anisotropic SBs are presented in Fig. 5.12. As expected, unable to drift laterally, all the anisotropic boundaries suddenly tilt back towards the growth axis with all the grains having equal wavelength.

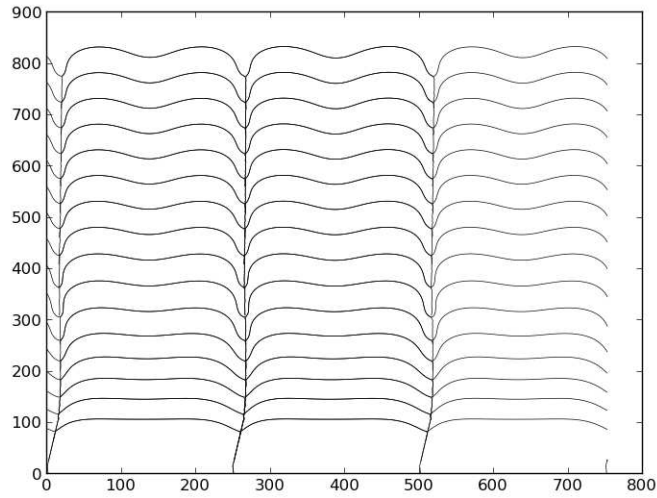


Figure 5.12: Superimposed snapshot pictures of the interfaces above MS: interaction between anisotropic SBs

## 5.5 Conclusions and Outlook

In this present work, we have used a multi-phase-field model to study the effects of strong capillary anisotropy on the orientation selection of the SBs in directional solidification of a dilute alloy. More specifically, we have increased the solidification rate  $V$  from 0 to the cellular-instability threshold and beyond to explore three different regimes of interest — below CS, above MS and in between these two limits. As the theory suggests, if we increase the velocity from 0 to the cellular-instability threshold (MS), SBs explore an angular range from a finite angle to a zero angle, and the transition happens in a rapidly decreasing manner.

Our numerical results suggest that, below the CS limit, SB indeed grows at an angle with respect to the growth axis with planar solid-melt interfaces ahead of it and this tilt angle closely follow the SP approximation theory. In contrast, two situations were observed above MS. For a finite mobility of the SBs, it continue to drift laterally at an angle prescribed by the SP theory; however, interestingly, the trajectory of the trijunction in a successive time plot follows a straight line. Since, in this regime, the theoretical tilt angle is approximated to zero, which is obeyed by the trijunction only, while SB still enjoys drifting at a finite angle, and, therefore, it can be concluded that the trajectory of

the trijunction is a more faithful representation of the tilt angle. When a zero mobility is enforced into the SBs, it obediently follow the trijunction trajectory making a nearly zero angle with the growth axis. Moreover, in the regime of the velocity in between the aforementioned limits, angular transition of SB occurs from a finite angle to a zero angle. This transition is, however, difficult to quantify, because vicinity of either CS or the MS limit significantly affect the interface shapes, and, hence, the resultant SB orientations. Qualitatively, this transition was found to be sharper and shorter, as we go from CS to MS limit. Finally, we shed some light on interacting SBs and it was found that such interactions can alter the kinetic path of the orientation selection, while the equilibrium morphology remains the same.

The picture is still unclear in the transition region delimited by CS and MS instability. This was very difficult to pursue because of numerous factors, such as, interface shapes (which progressively deform as we approach towards MS resulting different local equilibrium conditions at the trijunction), mobility, depth of grooves etc., are active in this regime, and hence, numerous simulations are needed to quantify this transition. However, this can be a prospective avenue for future work. In addition, meticulous analysis of the SB groove depth profiles can lead to another promising measure towards the quantification of our results. Finally, the anisotropy functions we have employed in this work are theoretically motivated. Hence, we can not compare these results with a real alloy system.

# Chapter 6

## Overall summary, Conclusions and Outlook

In this thesis, we use a multi-phase-field model to simulate solidification microstructures in the presence of anisotropy in two- and three dimensions. In particular, we install S-S boundary anisotropy in our code to study the development of orientations in the evolving patterns during S-L phase transitions.

At first, we simulate the growth of an eutectic lamella in the presence of inter-phase boundary anisotropy, in two dimensions. In the presence of anisotropy, lamellae grow at an angle with respect to the growth axis. We quantify this angle for different anisotropy functions, and compare it with a theoretical prediction, which postulates an analytical solution for an arbitrary rotation applied to the lamellar configuration, while keeping the relative orientation of the eutectic phases fixed. Two types of anisotropy functions are used in this study. For “standard” smooth anisotropy functions, the theory predicts a single solution for a particular rotation angle. Our numerical results closely follow this solution. In addition to this, in experiments, it is also observed that lamella can exhibit multiple tilt angles. To study such systems, we use an anisotropy function in the form of a deep yet smooth Gaussian to introduce multi-valued solutions for a particular rotation angle — one for the “crystallographically”-locked high-angle branch, one for the unlocked low-angle branch and one for an unstable branch. For this anisotropy function, we use

---

a sharp-interface boundary integral (BI) code to compare the results obtained using the PF code. The locked branch is well reproduced by the PF method up to a certain angle ( $\approx 35$  deg). While the PF method can produce only one solution for a single rotation angle, BI can produce two different solutions for the same rotation angle. Therefore, however, PF can find the solutions for both the branches, locked and unlocked, yet, it is unable to find two independent solutions at the same time. The merit of the BI goes to its ability to reproduce such bi-stable behaviour in these systems. Such physical discrepancies between the PF and the BI results can roughly be explained as follows. In the sharp interface or BI code, the trijunction is a point and, hence, can only explore one orientation at a particular time, whereas in diffuse interface models like PF, trijunction is diffuse and, hence, can explore a wide range of orientations around it and, once, a particular orientation is selected, the system can not bypass to other solutions.

Then, we perform simulations in three dimensions to shed some light on the development of preferred orientations in bulk solidification microstructures. In the context of directional eutectic solidification, development of such preferred orientations leads to periodic lamellar arrays along a unique direction. In the spirit of our previous 2D work, we have exploited anisotropy along the interphase boundaries as a driving force to develop these selected orientations. In bulk lamellar eutectics, there exists complex interactions between multiple eutectic grains and interphases. We study the competition between these interphase orientations using suitable anisotropy functions. In the absence of anisotropy, the microstructure contains random lamellar patches, because no orientation is particularly selected. When anisotropy is imparted, the microstructure begins to order depending on the underlying crystal structure of the solid. Complex interactions between the interphases in solid develop a labyrinth or random lamellar pattern in the beginning and, then, a few locally ordered patches appear with time. Once such locally exist minimum energy orientation relationships (OR) are established in the plane of isotherms, it continue to grow overwhelming all the surrounding unfavourable orientations in the microstructure. In this way, a preferred orientation is selected in the microstructure.

Finally, we repeat our eutectic study in two dimensions, but now, instead of two



---

dissimilar chemical phases, we use two chemically homogeneous phases to introduce a GB in the microstructure. This GB installs an in-built distortion to the solid-melt front, and we study the interaction of this deformation with the solute diffusion field in the spirit of morphological instability delimited by the CS and the MS critical velocities. In particular, we study the orientation selection of a LAGB or SB in these critical velocity limits. It is worthwhile to mention that, as the experiments suggest, these SBs possess a significant capillary anisotropy. Therefore, we simulate the growth of an anisotropic SB for different solidification velocities ranging from 0 to the cellular-instability threshold and measure the orientation it makes with respect to the growth axis. For a velocity below the CS limit, the SB grows at a finite angle with respect to the growth axis, and this angle is characterized in the same essence as the tilt angle is determined for the eutectic case. For a velocity above the MS limit, the SB grows at an angle of nearly zero, parallel to the growth axis. And, in between these two limits, a transition occurs from a finite angle to the zero angle, as we go from the CS to the MS limit. This transition is very difficult to quantify for numerous reasons. However, qualitatively, the results agree on the fact that, as we traverse from the CS to the MS limit, the transition becomes quicker, since the intensity of the instability is amplified with increased solidification rate. These numerically obtained tilt angles successfully agree a relevant theoretical prediction.

Our work opens many avenues for future research. In the thin-film lamellar eutectic case, the reasons for the discrepancies between the PF and the BI results, concerning bi-stability, are still unclear. In the text, we blame the diffusive nature of the trijunction for this. Hence, a detailed characterization of the trijunction region is necessary, because, we observe that, the change of orientations is triggered at this particular region forcing the interphase to select a biased orientation. In addition, a proper regularization in the trijunction may be helpful to counter the overlapping of high energy unstable orientations leading to erroneous orientations. A similar study on eutectic alloys with asymmetric phase diagram could also provide interesting insight in the orientation selection problem.

In the bulk eutectic case, the multi-grain orientation competition is indeed interesting which can be pursued for further studies to obtain a more detailed understanding in regard

to the experimental observations. For instance, the time scale over which the orientation relation (OR) is established in these microstructures from a completely disordered structure and, then, its becoming into a perfectly ordered structure can be very interesting prospect towards the production of composite structures in a industrial as well as in smaller laboratory scale. This *priori* information can save a lot of time as well as other significant resources in the production cycle. Plus, comparing the OR-developed simulated microstructures with the relevant experimental observations can produce significant insights to this grain selection problem [85].

In regard to the GB problem, the orientation selection of the SBs in between the CS and the MS limits is still a open question. The nature of this transition depends on numerous factors including the interface shapes, proximity to the critical limits, groove height, anisotropy etc., which again vary with the instability intensity factors  $G$  and  $V$ . Complex interactions between all these factors determine the nature of such angular transition. If any simplified empirical relationships can be established towards the selection of a SB orientation, we may obtain a clearer picture in this regime. Moreover, different anisotropy functions can produce different physical behaviour in the system. For example, the anisotropy function we work with does not exhibit missing orientations and the transition happens in a continuous manner. However, for an anisotropy function with missing orientations, a sharp jump may be possible.

Finally, a little is known about the “true” anisotropy functions in real materials. More information, from experiments or atomistic simulations, is needed before quantitative predictions for specific materials can be made.

# Appendix A

## Anisotropy Implementation Techniques

Here, we will discuss in more detail several technical points about our phase-field model; these are mostly known facts, but it seems useful to recall them briefly here in the spirit of implementing the anisotropy in our model.

Consider a two-phase system characterized by a single phase field  $\phi$ , with an interfacial free-energy functional of double-obstacle type

$$\Omega = \int [K(\nabla\phi)^2 + H\phi(1-\phi)] dV \quad (\text{A.1})$$

where  $K$  and  $H$  are constants and  $\phi$  is restricted to the interval  $[0, 1]$ . The equilibrium interface profile is given by

$$\phi(x) = \begin{cases} 0 & x/W < -\pi/2 \\ \frac{1}{2} + \frac{1}{2} \sin\left(\frac{x}{W}\right) & -\pi/2 \leq x/W \leq \pi/2 \\ 1 & x/W > \pi/2 \end{cases} \quad (\text{A.2})$$

for an interface normal to the  $x$  direction centered at the origin, with

$$W = \sqrt{\frac{K}{H}}. \quad (\text{A.3})$$

Furthermore, the standard evaluation of the surface excess free energy (the additional energy created by the presence of an interface) yields

$$\gamma = \frac{\pi}{4} \sqrt{KH}. \quad (\text{A.4})$$

Equations (A.3) and (A.4) can be inverted to express the constants  $K$  and  $H$  in terms of the surface free energy  $\gamma$  and the length scale  $\epsilon = 4W/\pi$ :

$$K = \gamma\epsilon, \quad (\text{A.5})$$

$$H = \frac{16\gamma}{\pi^2\epsilon}. \quad (\text{A.6})$$

It can easily be verified that this calculation remains valid for a binary interface (an interface between phases  $i$  and  $j$  along which  $\phi_i + \phi_j = 1$  and all other phase fields are zero) in the multi-phase-field setting; therefore, the parameters  $\gamma_{ij}$  in Eqs. (2.14) and (2.16) are directly the surface free energies of the respective interfaces.

In order to generate an anisotropy surface free energy that depends on the interface orientation ( $\theta$ ) according to

$$\gamma_{\alpha\beta}(\theta) = \bar{\gamma}_{\alpha\beta} a_c(\theta), \quad (\text{A.7})$$

where  $\bar{\gamma}_{\alpha\beta}$  is a constant and  $a_c(\theta)$  is the dimensionless anisotropy function, Eq. (A.4) can still be used, but the coefficients  $K$  and/or  $H$  need to be orientation-dependent. The “standard” procedure (see for example [105]) is to keep  $H$  constant and to write  $K(\theta) = \bar{K} a_c^2(\theta)$ . According to Eq. A.3, this creates variations in the interface thickness  $W$ , which becomes proportional to  $a_c$ . This can be avoided by letting  $K(\theta) = \bar{K} a_c(\theta)$  and  $H(\theta) = \bar{H} a_c(\theta)$ . Finally, it is also possible to keep the gradient energy coefficient constant and to write  $H(\theta) = \bar{H} a_c^2(\theta)$ , which leads to  $W \sim 1/a_c(\theta)$ .

It should be noted that each of these choices generates different equations of motion for the phase field. The functional derivative, for any functional of the form

$F = \int_V f(\phi, \nabla\phi, \nabla^2\phi)$  is explicitly given by

$$\frac{\delta F}{\delta\phi} = \frac{\partial f}{\partial\phi} - \sum_{i=x,y,z} \partial_i \frac{\partial f}{\partial(\partial_i\phi)} + \sum_{i,j=x,y,z} \partial_{ij}^2 \frac{\partial f}{\partial(\partial_{ij}^2\phi)}, \quad (\text{A.8})$$

where  $\partial_i\phi$  denote the Cartesian components of  $\nabla\phi$ . Since the interface orientation  $\theta$  can be expressed as a function of  $\nabla\phi$ , the second term on the right-hand-side acts on any  $\theta$ -dependent term in the functional. We have implemented the evolution equations corresponding to the three possibilities outlined above, and have compared the results for a few selected examples. We have found no significant differences. The results presented in the main text are obtained with the anisotropy function in the square gradient term only. In order to treat crystals that are rotated with respect to the temperature gradient (laboratory frame), we use coordinate transformations involving rotation matrices, as discussed in Sec. 2.5.

# Appendix B

## Rotation Matrices in 2-D and 3-D

### B.1 2-D

Basic properties of an elementary rotation matrix  $R$  are [106, 107]:  $R$  is invertible and  $\det R = 1$ ; mathematically  $R^{-1} = R^T$ , or  $RR^T = 1$

In 2-D,  $R$  can be expressed as:

$$R(\theta) = \begin{pmatrix} \cos \theta & -\sin \theta \\ \sin \theta & \cos \theta \end{pmatrix} \quad (\text{B.1})$$

Above rotation matrix rotates the coordinate axes clockwise. In turn, the axes points are rotated anti-clockwise.

### B.2 3-D

There are two invariants in 3-D rotation system:

- Axis of rotation: keeping an axis fixed while other two axes are rotated around the fixed axis. This essentially implies a 2D rotation in the rotating plane.
- Angle of rotation: (3 variants) Looking from the -X or -Y or -Z direction expose

*anti-clockwise* rotation of the axes points

- (i) Fixed axis: if the fixed axis is X then the rotation plane is YZ and (say) the respective rotation angle is  $\omega$

$$R_x(\omega) = \begin{pmatrix} 1 & 0 & 0 \\ 0 & \cos\omega & -\sin\omega \\ 0 & \sin\omega & \cos\omega \end{pmatrix} \quad (\text{B.2})$$

- (ii) Fixed axis: Y gives the rotation plane XZ with a rotation angle:  $\theta$

$$R_y(\theta) = \begin{pmatrix} \cos\theta & 0 & \sin\theta \\ 0 & 1 & 0 \\ -\sin\theta & 0 & \cos\theta \end{pmatrix} \quad (\text{B.3})$$

- (iii) Fixed axis: Z; rotation plane: XY; rotation angle:  $\kappa$

$$R_z(\kappa) = \begin{pmatrix} \cos\kappa & -\sin\kappa & 0 \\ \sin\kappa & \cos\kappa & 0 \\ 0 & 0 & 1 \end{pmatrix} \quad (\text{B.4})$$

- (iv) Composite Rotation: Combination of 2D rotations – Rotating around x first and then around y and lastly around z – produce an unique 3D rotation.

$$R_c = R_z(\kappa)R_y(\theta)R_x(\omega) \quad (\text{B.5})$$

The resultant  $3 \times 3$   $\mathbf{R}_c$  matrix is fully expressed below:

$$\begin{pmatrix} \cos\kappa\cos\theta & \cos\kappa\sin\theta\sin\omega - \sin\kappa\cos\omega & \cos\kappa\sin\theta\cos\omega + \sin\kappa\sin\omega \\ \sin\kappa\cos\theta & \sin\kappa\sin\theta\sin\omega + \cos\kappa\cos\omega & \sin\kappa\sin\theta\cos\omega - \cos\kappa\sin\omega \\ -\sin\theta & \cos\theta\sin\omega & \cos\theta\cos\omega \end{pmatrix} \quad (\text{B.6})$$

In a similar fashion, one can obtain the rotation matrices for a *clockwise* rotation. In our study, we judiciously choose the rotation matrices to obtain the system of model equations.



# Appendix C

## Choice of Anisotropy $\gamma$ Functions

### C.1 4-fold

In polar coordinate system, the standard four-fold surface tension anisotropy is written in the following form:

$$\gamma(\theta) = \gamma_i(1 + \epsilon_4 \cos 4\theta). \quad (\text{C.1})$$

$\theta$  is the angle between interface normal and the growth axis (say,  $z$ ).  $\epsilon_4$  is the strength of anisotropy in the surface tension and  $\gamma_i$  is the isotropic part of the surface tension. We can co-relate this polar form into the Cartesian normal vector descriptions of the system using  $\mathbf{n}_x/\mathbf{q}_x$  and  $\mathbf{n}_y/\mathbf{q}_y$  in a following way:

$$\begin{aligned} \cos 4\theta &= 2\cos^2 2\theta - 1 & (\text{C.2}) \\ &= \cos^2 2\theta - \sin^2 2\theta \\ &= (2\cos^2 \theta - 1)^2 - (2\sin \theta \cos \theta)^2 \\ &= 4\cos^4 \theta - 4(1 - \sin^2 \theta) + 1 - 4\sin^2 \theta(1 - \sin^2 \theta) \\ &= 4(\cos^4 \theta + \sin^4 \theta) - 3 \\ \therefore \gamma &= \gamma_i(1 + \epsilon_4(4(\cos^4 \theta + \sin^4 \theta) - 3)) \\ \therefore \gamma &= \gamma_i[1 - \epsilon_4(3 - 4(\cos^4 \theta + \sin^4 \theta))] \end{aligned}$$

Here, cosine and sin (polar coordinate) are the normal vectors in (Cartesian coordinate) x- and y- directions respectively. If we consider a normal vector in the following form:

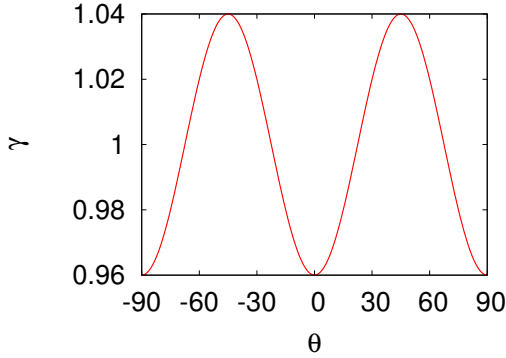
$$\mathbf{q}_{ij} = \phi_i \nabla \phi_j - \phi_j \nabla \phi_i, \quad (\text{C.3})$$

the corresponding anisotropic surface tension is given by,

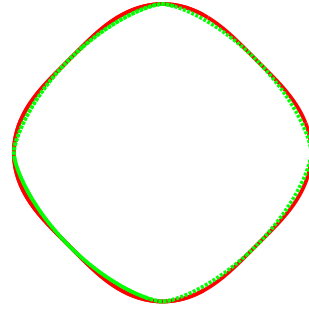
$$\gamma = \gamma_i \left[ 1 - \epsilon_4 \left( 3 - 4 \left( \frac{\mathbf{q}_x^4 + \mathbf{q}_y^4}{|q|^4} \right) \right) \right]. \quad (\text{C.4})$$

$$|q| = \sqrt{q_x^2 + q_y^2}$$

In the following, Eq. (C.1) is plotted and the corresponding symmetry is presented.



(a)  $\gamma - \theta$  plot



(b) Wulff shape: 4fold symmetry

## C.2 2-fold

Polar form of such symmetries:

$$\gamma(\theta) = \gamma_i (1 + \epsilon_2 \cos 2\theta). \quad (\text{C.5})$$

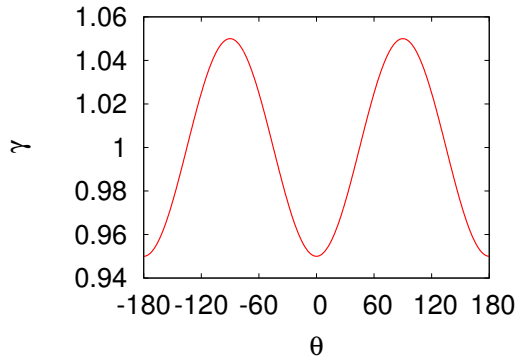
Applying the similar approach described above, we obtain the reduced form:

$$\gamma = \gamma_i (1 + \epsilon_2 (\cos^2 \theta - \sin^2 \theta)). \quad (\text{C.6})$$

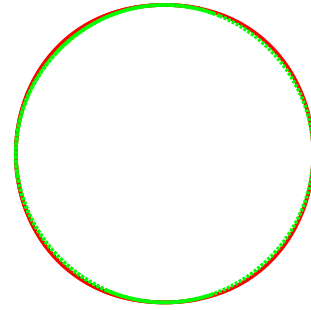
For a  $\mathbf{q}$  vector representation of the system anisotropy,  $\gamma$  becomes

$$\gamma = \gamma_i \left[ 1 + \epsilon_2 \left( \frac{\mathbf{q}_x^2 - \mathbf{q}_y^2}{|q|^2} \right) \right]. \quad (\text{C.7})$$

In the following, Eq. (C.5) is plotted and the corresponding symmetry is presented.



(a)  $\gamma - \theta$  plot



(b) Wulff shape: 2fold symmetry

### C.3 In presence of a cusp

A cusp is defined by a magnitude as well as by the depth, which can be represented using a normalized Gaussian function [45]. Magnitude of the cusp signifies the strength of the anisotropy which is designated as  $\epsilon_g$  and the depth of it described by parameter  $w_g$ .

In our work, we use the Gaussian of following form:

$$\gamma(\theta) = \gamma_i \left( 1 - \epsilon_g \exp \left[ -\frac{\theta^2}{w_g^2} \right] \right). \quad (\text{C.8})$$

For the  $\mathbf{q}$  vector representation of a system anisotropy it reduces to:

$$a_c(q) = 1 - \epsilon_g \exp \left( -\frac{\theta^2}{w_g^2} \right), \quad (\text{C.9})$$

in which  $\theta$  can be substituted as  $\tan^{-1} \frac{q_y}{q_x}$ . In the following, Eq. (C.8) is plotted and the corresponding symmetric shapes are presented. Note the equilibrium shape of a crystal can be computed using a combinations of normal  $\hat{n}$  and tangent vectors  $\hat{t}$ :  $\gamma \hat{n} + \gamma' \hat{t}$ . If some

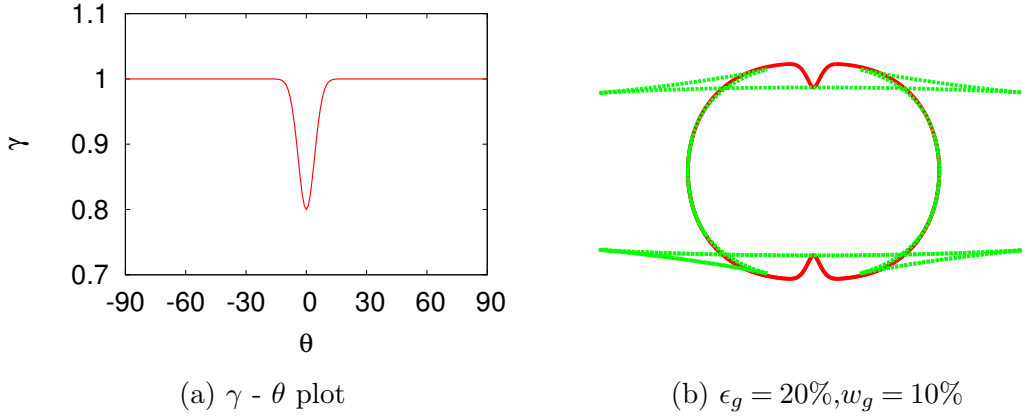


Figure C.3: (a)  $\gamma - \theta$  plot of function C.8 (b) parametric plot of  $\gamma$  (red) and the equilibrium shape (green) for the parameters listed above

parts of the equilibrium shape comes out of the the  $\gamma$  plot in the form of “ears” as in Fig. C.3, there are some orientations ( $\theta$ ) present in the system which are unstable ( $\gamma + \frac{d^2\gamma}{d\theta^2} > 0$ ) and are termed as missing orientations. Moreover, adjusting the two parameters  $\epsilon_g$  and  $w_g$  one can tune the anisotropy function to exhibit or not to exhibit the missing orientations in the system.

## C.4 Composite Anisotropy Function

Note, the previous  $\gamma$  function (Fig. C.3a) have two distinctive features: strongly anisotropic part in the cusp and the horizontal isotropic part. However, one can add another physical feature in the picture by smoothing out the cusp following a smooth transition between the anisotropic and the isotropic parts of the  $\gamma$  function as in Fig. C.4a. Such a composite anisotropy function can be represented using a combinations of the Gaussian and other smooth anisotropy functions like two-fold and four-fold [45]:

$$\gamma(\theta) = \gamma_i \left( 1 - \epsilon_g \exp \left[ -\frac{\theta^2}{w_g^2} \right] - \epsilon_2 \cos[2\theta] - \epsilon_4 \cos[4\theta] \right). \quad (\text{C.10})$$

The definitions of all the elements are the same as before.

In Fig. C.4b, the equilibrium crystal shape is presented using such  $\gamma$  function which does not exhibit any missing orientations.

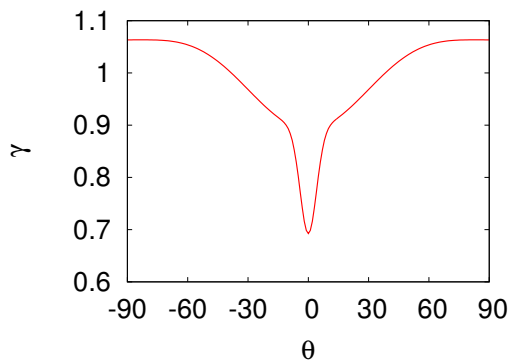
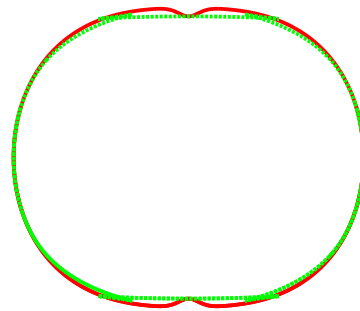
(a)  $\gamma - \theta$  plot(b)  $\epsilon_g = 5\%, \epsilon_2 = 8\%, \epsilon_4 = 2\%, w_g = 20\%$ 

Figure C.4: (a)  $\gamma - \theta$  plot of function C.10 (b) parametric plot of  $\gamma$  (red) and the equilibrium shape (green) for the parameters listed above

# Bibliography

- [1] W. Kurz and D.J. Fisher. *Fundamentals of solidification*. Number v. 1. Trans Tech Publications, 1986.
- [2] D. M. Stefanescu. *Science and Engineering of Casting Solidification*. Number v. 2. Springer, 2009.
- [3] G.J. Davies. *Solidification and casting*. Wiley, 1973.
- [4] Klaus Kassner. *Pattern formation in diffusion-limited crystal growth*. World Scientific, 1996.
- [5] Heiner Müller-Krumbhaar, Wilfried Kurz, and Efim Brener. *Materials Science and Technology*. Wiley-VCH Verlag GmbH & Co. KGaA, 2006.
- [6] B. Utter and E. Bodenschatz. Dynamics of low anisotropy morphologies in directional solidification. *Physical Review E*, 66:051604, 2002.
- [7] Brian utter. *Low anisotropy growth in directional solidification*. PhD thesis, Cornell University, 2001.
- [8] H. Biloni and W.J. Boettinger. Chapter 8 - solidification. In Robert W. CahnPeter Haasen, editor, *Physical Metallurgy (Fourth Edition)*, pages 669 – 842. North-Holland, Oxford, fourth edition edition, 1996.
- [9] W. A. Tiller, K. A. Jackson, J. W. Rutter, and B. Chalmers. The redistribution of solute atoms during the solidification of metals. *Acta Metallurgica*, 1:428, 1953.

- [10] W. W. Mullins and R. F. Sekerka. Stability of a planar interface during solidification of a dilute binary alloy. *J. appl. Phys.*, 35:444, 1964.
- [11] J. S. Langer. Instabilities and pattern formation in crystal growth. *Rev. Mod. Phys.*, 52:1, 1980.
- [12] A. Prince. *Alloy phase equilibria*. Elsevier Pub. Co., 1966.
- [13] D.A. Porter and K.E. Easterling. *Phase Transformations in Metals and Alloys, Third Edition (Revised Reprint)*. Taylor & Francis, 1992.
- [14] K. A. Jackson and J. D. Hunt. Lamellar and rod eutectic growth. *Transactions of the Metallurgical Society of AIME*, 236:1129, 1966.
- [15] M. Hillert. The role of interfacial energy during solid state phase transformations. *Jernkontorets Ann.*, 141:773, 1957.
- [16] M. Plapp and A. Karma. Eutectic colony formation: A stability analysis. *Phys. Rev. E*, 60:6865, 1999.
- [17] A. Dennstedt and L. Ratke. Microstructures of directionally solidified Al-Ag-Cu ternary eutectics. *Transactions of Indian Institute of Metals*, 65:777–782, 2012.
- [18] A. Choudhury, M. Plapp, and B. Nestler. Theoretical and numerical study of lamellar eutectic three-phase growth in ternary alloys. *Physical Review E*, 83:051608, 2011.
- [19] G.A. Chadwick. *Eutectic Alloy Solidification*. Progress in materials science. Pergamon, 1963.
- [20] K. Kassner and C. Misbah. Spontaneous parity-breaking transition in directional growth of lamellar eutectic structures. *Phys. Rev. A*, 44:6533–6543, 1991.
- [21] A. Karma and A. Sarkissian. Morphological instabilities of lamellar eutectics. *Metall. Mat. Trans. A*, 27:635, 1996.
- [22] M. Ginibre, S. Akamatsu, and G. Faivre. Experimental determination of the stability diagram of a lamellar eutectic growth front. *Phys. Rev. E*, 56(1):780, 1997.

- [23] D. D. Double. Imperfections in lamellar eutectic crystals. *Materials Science and Engineering*, 11:325–335, 1973.
- [24] K. Kassner and C. Misbah. Growth of lamellar eutectic structures: The axisymmetric state. *Phys. Rev. A*, 44:6513–6532, Nov 1991.
- [25] M. Plapp. Three dimensional phase-field simulations of directional solidification. *Journal of crystal growth*, 303:49–57, 2007.
- [26] J.W. Martin, J.W. Martin, R.D. Doherty, and B. Cantor. *Stability of Microstructure in Metallic Systems*. Cambridge Modular Sciences. Cambridge University Press, 1997.
- [27] R.W. Balluffi, S. Allen, and W.C. Carter. *Kinetics of Materials*. Wiley, 2005.
- [28] Physical Review. Some theorms on the free energies of crystal surfaces. *The European Physical Journal Plus*, 82(1):87–93, 1951.
- [29] DW Hoffman and JW Cahn. Vector thermodynamics for anisotropic surfaces .1. fundamentals and application to plane surface junctions. *Surface Science*, 31:368, 1972.
- [30] M. Fleck, L. Mushongera, D. Pilipenko, K. Ankit, and H. Emmerich. On phase-field modeling with a highly anisotropic interfacial energy. *The European Physical Journal Plus*, 126(10):95, 2011.
- [31] M. Rappaz, J. Friedli, A. Mariaux, and M. Salgado-Ordorica. The influence of solid-liquid interfacial energy anisotropy on equilibrium shapes, nucleation, triple lines and growth morphologies. *Scripta Materilia*, 62:904–909, 2010.
- [32] M. Asta, C. Beckermann, A. karma, W. Kurz, R. Napolitano, M. Plapp, G. Purdy, M. Rappaz, and R. Trivedi. Solidification microstructures and solid-state parallels: Recent developments, future directions. *Acta Materialia*, 57:941–971, 2009.



- [33] S. Akamatsu, G. Faivre, and T. Ihle. Symmetry-broken double fingers and seaweed patterns in thin film directional solidification of a nonfaceted cubic crystal. *Physical Review E*, 51(5):4751–4773, 1995.
- [34] J. Deschamps, M. Georgelin, and A. Pocheau. Crystal anisotropy and growth directions in directional solidification. *Europhys. Lett.*, 76 (2), pp. 291-297 (2006), 76(2):291–297, 2006.
- [35] J. Deschamps, M. Georgelin, and A. Pocheau. Growth directions of microstructures in directional solidification of crystalline materials. *Phys. Rev. E*, 78:011605, 2008.
- [36] A. Pocheau, J. Deschamps, and M. Georgelin. Maximal curvature and crystal orientation on directionally solidified dendrites. *Phys. Rev. E*, 81:051608, 2010.
- [37] Morteza Amoorezaei, Sebastian Gurevich, and Nikolas Provatas. Orientation selection in solidification patterning. *Acta Materialia*, 60(2):657–663, 2012.
- [38] Jihene Ghmadh, Jean-Marc Debierre, Julien Deschamps, Marc Georgelin, Rahma Guérin, and Alain Pocheau. Directional solidification of inclined structures in thin samples. *Acta Materialia*, 74:255 – 267, 2014.
- [39] Tomohiro Takaki, Munekazu Ohno, Takashi Shimokawabe, and Takayuki Aoki. Two-dimensional phase-field simulations of dendrite competitive growth during the directional solidification of a binary alloy bicrystal. *Acta Materialia*, 81(0):272–283, 2014.
- [40] D. Tournet and A. Karma. Growth competition of columnar dendritic grains: A phase-field study. *Acta Materialia*, 82(0):64–83, 2015.
- [41] S. Akamatsu, S. Bottin-Rousseau, M. Şerefoğlu, and G. Faivre. Lamellar eutectic growth with anisotropic interphase boundaries: Experimental study using rotational directional solidification. *Acta Materialia*, 60:3206–3214, 2012.
- [42] H Jones. The solid–liquid interfacial energy of metals: calculations versus measurements. *Materials Letters*, 53(4–5):364–366, 2002.

- [43] R.E. Napolitano, Shan Liu, and R. Trivedi. Experimental measurement of anisotropy in crystal-melt interfacial energy. *Interface Science*, 10(2-3):217–232, 2002.
- [44] Kuo-An Wu, Alain Karma, Jeffrey J. Hoyt, and Mark Asta. Ginzburg-landau theory of crystalline anisotropy for bcc-liquid interfaces. *Phys. Rev. B*, 73:094101, 2006.
- [45] S. Akamatsu, S. Bottin-Rousseau, M. Şerefoğlu, and G. Faivre. A theory of thin lamellar eutectic growth with anisotropic interphase boundaries. *Acta Materialia*, 60:3199–3205, 2012.
- [46] A. Dougherty. Surface tension anisotropy and the dendritic growth of pivalic acid. *Journal of crystal growth*, 110:501–508, 1991.
- [47] R. S. Qin and H. K. Bhadesia. Phase field method. *Materials Science and Technology*, 26:803–811, 2010.
- [48] Nikolas Provatas and Ken Elder. *Phase-Field Methods in Materials Science and Engineering*. Wiley-VCH Verlag GmbH & Co. KGaA, 2010.
- [49] Nele Moelans, Bart Blanpain, and Patrick Wollants. An introduction to phase-field modeling of microstructure evolution. *Calphad*, 32(2):268 – 294, 2008.
- [50] L-Q Chen. phase-field models for microstructure evolution. *Annu. Rev. Mater. Res.*, 32:113–140, 2002.
- [51] M. Plapp. Unified derivation of phase-field models for alloy solidification from a grand-potential functional. *Physical Review E*, 84:031601, 2011.
- [52] B. Echebarria, R. Folch, A. Karma, and M. Plapp. Quantitative phase-field model of alloy solidification. *Phys. Rev. E*, 70(6):061604, 2004.
- [53] I. Steinbach. Phase-field models in materials science. *Modelling Simul. Mater. Sci. Eng.*, 17:073001, 2009.
- [54] W. J. Boettinger, J. A. Warren, C. Beckermann, and A. Karma. Phase field simulation of solidification. *Annu. Rev. Mater. Res.*, 32:163–194, 2002.

- [55] Oliver Penrose and Paul C. Fife. Thermodynamically consistent models of phase-field type for the kinetic of phase transitions. *Physica D: Nonlinear Phenomena*, 43(1):44–62, 1990.
- [56] S.-L. Wang, R.F. Sekerka, A.A. Wheeler, B.T. Murray, S.R. Coriell, R.J. Braun, and G.B. McFadden. Thermodynamically-consistent phase-field models for solidification. *Physica D: Nonlinear Phenomena*, 69(1–2).
- [57] G. B. McFadden, A. A. Wheeler, R. J. Braun, S. R. Coriell, and R. F. Sekerka. Phase-field models for anisotropic interfaces. *Phys. Rev. E*, 48:2016–2024, 1993.
- [58] G. Caginalp and W. Xie. Phase-field and sharp-interface alloy models. *Phys. Rev. E*, 48:1897–1909, 1993.
- [59] Alain Karma. Phase-field model of eutectic growth. *Phys. Rev. E*, 49:2245–2250, 1994.
- [60] I. Steinbach, F. Pezzolla, B. Nestler, M. Seeßelberg, R. Prieler, G.J. Schmitz, and J.L.L. Rezende. A phase field concept for multiphase systems. *Physica D: Nonlinear Phenomena*, 94(3):135–147, 1996.
- [61] J. Eiken, B. Böttger, and I. Steinbach. Multiphase-field approach for multicomponent alloys with extrapolation scheme for numerical application. *Phys. Rev. E*, 73:066122, 2006.
- [62] B. Nestler and A. A. Wheeler. A multi-phase-field model of eutectic and peritectic alloys: numerical simulation of growth structures. *Physica D*, 138:114–133, 2000.
- [63] Britta Nestler, Harald Garcke, and Björn Stinner. Multicomponent alloy solidification: Phase-field modeling and simulations. *Phys. Rev. E*, 71:041609, 2005.
- [64] A. Choudhury and B. Nestler. Grand-potential formulation for multicomponent phase transformations combined with thin-interface asymptotics of the double-obstacle potential. *Physical Review E*, 85:021602, 2012.

- [65] A. A. Wheeler. Phase field theory of edges in an anisotropic crystal. *Proc. R. Soc. A*, 462:3363–3384, 2006.
- [66] Seong Gyoon Kim, Won Tae Kim, and Toshio Suzuki. Phase-field model for binary alloys. *Phys. Rev. E*, 60:7186–7197, 1999.
- [67] D. A. Cogswell and W. C. Carter. Thermodynamic phase-field model for microstructure with multiple component and phases: The possibility of metastable phases. *Physical Review E*, 83:061602, 2011.
- [68] U. Hecht et al. Multiphase solidification in multicomponent alloys. *Materials Science and Engineering R*, 46:1–49, 2004.
- [69] S. Bottin-Rousseau, S. Akamatsu, and G. Faivre. Dynamical polygonization below the cellular-bifurcation threshold in thin-sample directional solidification. *Physical Review B*, 66:054102, 2002.
- [70] J. W. Cahn and J. E. Hilliard. Free energy of a nonuniform system. i. interfacial free energy. *The Journal of Chemical Physics*, 28(2):258–267, 1958.
- [71] Abhik Choudhury. *Quantitative phase field model for phase transformations in multi-component alloys*. PhD thesis, Karlsruhe Institute of Technology, 2012.
- [72] S. Ghosh, S. Akamatsu, S. Bottin-Rousseau, G. Faivre, A. Choudhury, and M. Plapp. Intrephase anisotropy effects on lamellar eutectics: A numerical study. *Physical Review E*, 91:022407, 2015.
- [73] R. Folch and M. Plapp. Quantitative phase-field modeling of two-phase growth. *Physical Review E*, 72:011602, 2005.
- [74] J.J. Eggleston, G.B. McFadden, and P.W. Voorhees. A phase-field model for highly anisotropic interfacial energy. *Physica D*, 150:91–103, 2001.
- [75] S. Torabi, J. Lowengrub, A. Voigt, and S. Wise. A new phase-field model for strongly anisotropic systems. *Proc. R. Soc. A*, 465:1337–1359, 2009.

- [76] Kumar Ankit, Rajdip Mukherjee, Tobias Mittnacht, and Britta Nestler. Deviations from cooperative growth mode during eutectoid transformation: Insights from a phase-field approach. *Acta Materialia*, 81(0):204 – 210, 2014.
- [77] LM Hogan, RW Kraft, and FD Lemkey. Eutectic grains. *Adv. Mater. Res.*, 5:83–216, 1971.
- [78] U. Hecht et al. Multiphase solidification on multicomponent alloys. *Materials Science and Engineering Reports*, 46:1–49, 2004.
- [79] J. Llorca and V. M. Orera. Directionally solidified eutectic ceramics. *Progress in Materials Science*, 51:711, 2006.
- [80] B Caroli, C Caroli, G Faivre, and J Mergy. Lamellar eutectic growth of  $CBr_4 - C_2Cl_6$ : effect of crystal anisotropy on lamellar orientations and wavelength dispersions. *J. Cryst. Growth*, 118:135–150, 1992.
- [81] S Akamatsu, G Faivre, and S Moulinet. The formation of lamellar-eutectic grains in thin samples. *Metall. Mater. Trans. A*, 32:2039, 2001.
- [82] S. Akamatsu, M. Plapp, G. Faivre, and A. Karma. Pattern stability and trijunction motion in eutectic solidification. *Phys. Rev. E*, 66:30501, 2002.
- [83] S. Akamatsu, M. Plapp, G. Faivre, and A. Karma. Overstability of lamellar eutectic growth below the minimum-undercooling spacing. *Metall. Mater. Trans. A*, 35:1815–1528, 2004.
- [84] P. Manneville. *Dissipative Structures and Weak Turbulence*. Academic Press, Boston, 1990.
- [85] U Hecht, VT Witusiewicz, A Drevermann, and S Rex. Orientation relationship in univariant Al-Cu-Ag eutectics. *Trans. Indian Inst. Met.*, 58:545–551, 2005.
- [86] Conyers Herring. Some theorems on the free energies of crystal surfaces. *Phys. Rev.*, 82:87–93, 1951.

- [87] N. Cabrera. The equilibrium of crystal surfaces. *Surf. Sci.*, 2:320–345, 1964.
- [88] JM Debierre, A Karma, F Celestini, and R Guerin. Phase-field approach for faceted solidification. *Phys. Rev. E*, 68, 2003.
- [89] V. Kokotin and U. Hecht. Molecular dynamics simulations of Al–Al<sub>2</sub>Cu phase boundaries. *Computational Materials Science*, 86:30–37, 2014.
- [90] S. Akamatsu, S. Bottin-Rousseau, and G. Faivre. Experimental evidence for a zigzag bifurcation in bulk lamellar eutectic growth. *Phys. Rev. Lett.*, 93:175701, 2004.
- [91] A. Parisi and M. Plapp. Stability of lamellar eutectic growth. *Acta Materialia*, 56:1348, 2008.
- [92] A. Parisi and M. Plapp. Defects and multistability in eutectic solidification patterns. *EPL*, 90:26010, 2010.
- [93] M. Perrut, A. Parisi, S. Akamatsu, S. Bottin-Rousseau, G. Faivre, and M. Plapp. Role of transverse temperature gradients in the generation of lamellar eutectic solidification patterns. *Acta Materialia*, 58:1761–1769, 2010.
- [94] A. Hellawell and P. M. Herbert. The development of preferred orientations during the freezing of metals and alloys. *Proc. R. Soc. A*, 269:560–574, 1962.
- [95] D. Hull and D.J. Bacon. *Introduction to Dislocations*. Materials science and technology. Elsevier Science, 2011.
- [96] K. Kassner and C. Misbah. Similarity laws in eutectic growth. *Phys. Rev. Lett.*, 66:445–448, Jan 1991.
- [97] U. Hecht, V. Witisiewicz, and S. Rex. Solidification of bulk lamellar eutectics. *Materials Science Forum*, 790-791:343–348, 2014.
- [98] S. Y. Yeh, C. C. Chen, and C. W. Lan. Phase field modeling of morphological instability near grain boundary during directional solidification of a binary alloy: The hump formation. *Journal of Crystal Growth*, 324:296–303, 2011.

- [99] S. R. Coriell and R. F. Sekerka. Morphological stability near a grain boundary groove in a solid-liquid interface during solidification of a binary alloy. *Journal of Crystal Growth*, 19:285–293, 1973.
- [100] L. H. Ungar and R. A. Brown. Cellular interface morphologies in directional solidification. ii. the effect of grain boundaries. *Physical Review B*, 30:3993, 1984.
- [101] L. H. Ungar and R. A. Brown. Cellular interface morphologies in directional solidification. iv. the formation of deep cells. *Physical Review B*, 31:5931, 1985.
- [102] W. T. Read and W. Shockley. Dislocation models of crystal grain boundaries. *Phys. Rev.*, 78:275–289, 1950.
- [103] G. Faivre, S. Bottin-Rousseau, and S. Akamatsu. The trajectory of subboundary grooves during directional solidification of dilute alloys. *Comptes Rendus Physique*, 14:149–155, 2013.
- [104] P. Lejcek. *Grain Boundary Segregation in Metals*. Springer Series in Materials Science. Springer Berlin Heidelberg, 2010.
- [105] A. Karma and W.-J. Rappel. Quantitative phase-field modeling of dendritic growth in two and three dimensions. *Phys. Rev. E*, 57(4):4323–4349, 1998.
- [106] D. G. Zill and M. R. Cullen. *Advanced Engineering Mathematics*. Number v. 2. CBS, 2003.
- [107] E. Kreyszig. *Advanced Engineering Mathematics*. John Wiley & Sons, 2010.